

Nebular phase spectral line formation in Type IIb supernovae, with application to SN 1993J, SN 2008ax, and SN 2011dh

Anders Jerkstrand¹, Mattias Ergon², Stephen Smartt¹, Claes Fransson², Jesper Sollerman², Stefan Taubenberger³, and Jason Spyromilio⁴

¹ Astrophysics Research Centre, School of Mathematics and Physics, Queen's University Belfast, Belfast BT7 1NN, UK

² The Oskar Klein Centre, Department of Astronomy, Stockholm University, Albanova, 10691 Stockholm, Sweden

³ Max-Planck-Institut für Astrophysik, Karl-Schwarzschild-Str. 1, D-85741 Garching, Germany

⁴ ESO, Karl-Schwarzschild-Strasse 2, 85748 Garching, Germany

Received.....; accepted.....

ABSTRACT

We investigate line formation processes in Type IIb supernovae from 100 to 500 days post-explosion using NLTE radiative transfer simulations. The modeling identifies the nuclear burning layers and physical mechanisms that produce the major emission lines, and the diagnostic potential of these. We compare the model calculations with data on the three best observed Type IIb SNe to-date - SN 1993J, SN 2008ax, and SN 2011dh. Since oxygen nucleosynthesis depends sensitively on the main-sequence mass of the star, the modeling constrains the progenitors of these three SNe to the 12 – 16 M_{\odot} range (**ejected oxygen masses** 0.3 – 0.9 M_{\odot}), with SN 2011dh towards the lower end and SN 1993J towards the upper end of the range. The high ejecta masses from $M_{ZAMS} \geq 17 M_{\odot}$ progenitors give too bright nebular phase emission lines to match the observed line luminosities. Nucleosynthesis analysis thus supports a scenario of low/moderate mass progenitors for Type IIb SNe, and by implication an origin in binary systems. Oxygen and magnesium recombination lines provide further constraints on the hydrodynamic structure of the ejecta, and imply a clumpy ejecta distribution, with the line forming regions occupying a small ($\sim 1\%$) fraction of the core volume of the supernova. From the line luminosities in SN 2011dh we derive a mass of synthesized magnesium of 0.03 – 0.3 M_{\odot} , which together with constraints from the oxygen lines gives a Mg/O production ratio of $-0.3 < [\text{Mg}/\text{O}] < +1$. Among other results, we find the nitrogen left in the He envelope from CNO-burning to give strong [N II] $\lambda\lambda 6548, 6583$ emission that dominates over the $H\alpha$ emission in our models. We find the H envelopes in Type IIb SNe to be too small and dilute to produce any noticeable $H\alpha$ emission or absorption after ~ 150 days. Finally, the influence of radiative transport on the emergent line profiles is investigated. Even as steady-state conditions set in after ~ 100 days, the large velocity gradients lead to significant line blocking for several hundred days, which affects the emergent spectrum. We show here how these radiative transfer effects lead to blue-shifted emission line profiles which gradually move towards symmetry as the densities decrease with time. The modelled evolution of this effect matches the observed evolution in SN 2011dh, but in SN 1993J and SN 2008ax the predicted time evolution is not seen.

Key words. supernovae: general – supernovae: individual: SN 2011dh

1. Introduction

Massive stars that have retained their helium envelopes but lost all or most of their hydrogen envelopes explode as Type Ib and IIb supernovae (SNe), respectively. The Type Ib class was recognized with SN 1983N and SN 1984L (Elias et al. 1985; Uomoto & Kirshner 1985; Wheeler & Levreault 1985). Initially unclear whether these were thermonuclear or core-collapse events, identification of strong helium lines (Harkness et al. 1987), association with galactic spiral arms and HII regions (Porter & Filippenko 1987), strong radio emission (Sramek et al. 1984; Panagia et al. 1986), and oxygen lines in the nebular spectra (Porter & Filippenko 1987; Schlegel & Kirshner 1989) soon established them as originating from massive stars.

The Type IIb class was established with SN 1987K (Filippenko 1988) and the well-studied SN 1993J (Filippenko et al. 1993; Nomoto et al. 1993), after theoretical conception by Woosley et al. (1988). SNe of this type are characterized by hydrogen lines at early times which subsequently fade away. In both Type IIb and Ib SNe, the metal and helium emission lines are significantly broader than in Type IIP SNe, as there is almost no hydrogen in the ejecta to take up the explosion energy

(Filippenko et al. 1994). The light curves and spectral evolution (except for the H lines) are very similar to those of Type Ib SNe (Woosley et al. 1994; Filippenko et al. 1994), and Type Ib and IIb explosions are therefore understood as coming from similar stars. Some authors have even argued that there are signs of hydrogen in most Type Ib SNe, and that these classes could therefore be one and the same (Branch et al. 2002; Elmhamdi et al. 2006).

A promising mechanism for removing the hydrogen envelopes from the Type IIb progenitors is Roche lobe overflow to a binary companion (e.g. Podsiadlowski et al. 1992). This mechanism has the attractive property of naturally leaving hydrogen envelopes of mass 0.1 – 1 M_{\odot} for many binary configurations (Woosley et al. 1994), and the detection of a companion star to SN 1993J (Maund et al. 2004) gave important credibility to this scenario. However, population synthesis modeling by Claeys et al. (2011) finds the region of binary parameter space to be too restricted to reproduce the observed Type IIb rate ($\sim 10\%$ of the **core-collapse rate**, Li et al. (2011); Smith et al. (2011); Eldridge et al. (2013)).

Wind-driven mass loss in single stars is another candidate for producing Type IIb progenitors, but also in this scenario it is

difficult to reproduce the observed rate, as this mechanism has no natural turn-off point as the envelope reaches the $0.1 - 1 M_{\odot}$ range (Claeys et al. 2011). Whereas revisions of binary population parameters could significantly change the predicted rates for SNe from interaction (e.g. Sana et al. 2012), the prospects of obtaining much higher Type IIb rates from single stars is probably smaller. Recent downward revisions of theoretical Wolf-Rayet mass loss rates have also led to a questioning about the general ability of wind-driven mass loss for producing stripped-envelope CCSNe (Yoon et al. 2010).

To advance our understanding of the nature of these SNe, modeling of their light curves and spectra must be undertaken. One important analysis technique is nebular phase spectral modeling. In this phase, emission lines from the entire ejecta provide information about mass and composition, which in turn constrains the nature of the progenitor. The radioactive decay of ^{56}Co and other isotopes powers the SN nebula for many years and decades after the initial explosion, and modeling of the gas allows inference over abundances and mixing. Recent years have seen the development of codes that solve for the non-thermal heating, excitation, and ionization rates in the ejecta, the NLTE equations in each nuclear burning layer, and the radiative transfer equations (e.g. Dessart & Hillier 2011; Jerkstrand et al. 2011; Maurer et al. 2011). These codes are capable of reproducing observed SN spectra to relatively high accuracy, and can be used to derive abundances and constrain other properties of the ejecta.

Here, we perform spectral modeling of Type IIb SN ejecta in the 100 – 500 day phase, and use these models to interpret observations of the three best observed events in the IIb class to-date : SN 1993J, SN 2008ax, and SN 2011dh. We put particular emphasis on the well-observed SN 2011dh, which exploded in the nearby (7.8 Mpc) Whirlpool Galaxy (M51) on May 31, 2011. The detection (and confirmed disappearance) of the progenitor star (Maund et al. 2011; Ergon et al. 2013; Van Dyk et al. 2013), as well as hydrodynamical modeling of the early light curve (Bersten et al. 2012; Ergon et al. 2013; Ergon & Jerkstrand 2014) point towards a $M_{\text{ZAMS}} \sim 13 M_{\odot}$ progenitor. Such a progenitor would, with little doubt, imply a binary mechanism being responsible for the loss of the H envelope. An important confirmation of this result on the progenitor is to analyse the nucleosynthesis from the nebular phase spectra, which is one of the aims of this paper. We also aim to derive information about specific nucleosynthesis yields, explosive mixing, and to provide Type IIb model spectra for generic future use. This paper is accompanied by a companion paper (Ergon & Jerkstrand 2014), where further analysis and the observations and data reduction for SN 2011dh is presented.

2. Observational data

For our analysis we use the spectra of SN 1993J, SN 2008ax, and SN 2011dh listed in Table 1.

2.1. SN 2011dh

The observations and data reduction are described in Ergon & Jerkstrand (2014).

2.2. SN 2008ax

Spectra from Calar Alto, Asiago, TNG (Taubenberger et al. 2011), and from MDM and MMT (Milisavljevic et al. 2010).

Both sets of spectra up to 360 days were flux calibrated to the photometry in Taubenberger et al. (2011).

We use $D = 9.6_{-1.3}^{+1.3}$ Mpc (Pastorello et al. 2008) and $E_{B-V} = 0.40_{-0.10}^{+0.10}$ (Taubenberger et al. 2011), and $V = 565$ km s $^{-1}$ (Milisavljevic et al. 2010). Where we plot line luminosities relative to the ^{56}Co decay, we use a ^{56}Ni mass of $0.10 M_{\odot}$ (Taubenberger et al. 2011). **Phases are relative to the estimated explosion epoch of March 3 2008 (Taubenberger et al. 2011).**

2.3. SN 1993J

Spectra from the 1.8 m Asiago telescope (Barbon et al. 1995), downloaded from SUSPECT, and ING (Lewis et al. 1994), obtained from P. Meikle¹. **The ING dataset includes spectra from the 2.5 Isaac Newton Telescope (INT), with the FOS1 and IDS spectrographs, and from the 4.0 m William Herschel Telescope (WHT) with the ISIS spectrograph.**

All spectra were calibrated to the linearly interpolated ING *BVR* photometry, or *VR* when *B* was not covered. An exception was the 284 day spectrum, where only the *I* band was covered, which was calibrated to this band. We use a distance $D = 3.63$ Mpc (Freedman et al. 1994; Ferrarese et al. 2000) an extinction $E_{B-V} = 0.17$ (Ergon et al. 2013), and a Doppler correction $V = 130$ km s $^{-1}$ (Maund et al. 2004). Where we plot line luminosities relative to the ^{56}Co decay, we use a ^{56}Ni mass of $0.09 M_{\odot}$ (Woosley et al. 1994, corrected for the different distance assumed here).

3. Modeling

We use the SN spectral synthesis code described in Jerkstrand et al. (2011) and Jerkstrand et al. (2012) to compute synthetic spectra and photometry for a variety of ejecta structures as described below. The operations of the code are the same as described in the papers mentioned above, with some updates specified in Appendix B.

3.1. Nucleosynthesis

We take nucleosynthesis calculations from the evolution and explosion ($E = 1.2 \times 10^{51}$ erg) of solar metallicity, non-rotating stars with KEPLER (Woosley & Heger 2007). These stars end their lives with most of their hydrogen envelopes intact (at least for the mass range of interest here), but as the nuclear burning after H exhaustion is largely uncoupled from the dynamic state of the H envelope (e.g. Chiosi & Maeder 1986; Ensmann & Woosley 1988), the nucleosynthesis is unaffected by the late-time mass loss that has occurred in the progenitor (**Roche lobe overflow transfer begins only in the helium burning stage or later (e.g. Woosley et al. 1994).**)

Table 2 lists the masses of the major elements in the KEPLER ejecta as function of progenitor mass. It is clear that oxygen lines are promising diagnostics of the progenitor mass, as the oxygen production shows a strong and monotonic dependence on M_{ZAMS} . Silicon, calcium, and magnesium also have strong dependencies, but the production functions are not strictly monotonic.

¹ The spectra taken after 125 days have not been published.

Table 1. List of observed spectra used in this work. The phases are relative to the estimated explosion epochs.

SN	Date	Phase (days)	WI (Å)	Res (Å)	Telescope (spectrograph)	Source
SN 1993J	1993-07-12	106	3380-10660	11	INT (FOS1)	Lewis 1994
	1993-07-23	118	3300-9400	11	Asiago 1.8m (B&C/300)	Barbon 1995
	1993-09-15	172	4000-9150	22	Asiago 1.8m (B&C/1200)	Barbon 1995
	1993-09-20	176	3400-9340	2.8	WHT (ISIS)	unpublished
	1993-11-07	224	4000-8800	2.8	WHT (ISIS)	unpublished
	1993-12-17	264	3500-9500	2.8	WHT (ISIS)	unpublished
	1994-01-05	283	3500-9200	2.9	WHT (ISIS)	unpublished
	1994-02-17	326	3700-9400	3.1	INT (IDS)	unpublished
	1994-04-20	388	5600-9400	3.1	INT (IDS)	unpublished
	1994-05-17	415	3400-9200	3.1	INT (IDS)	unpublished
SN 2008ax	2008-06-11	101	3350-9300	11	TNG (DOLORES)	T11
	2008-06-27	116	3300-6400	13	CA-2.2m (CAFOS,B200)	T11
	2008-07-03	122	4400-7900	11	MDM/CCDS	M10
	2008-07-11	130	8800-24500	22,26	TNG (NICS)	T11
	2008-07-24	143	3600-9400	24,38	Mt Ekar (AFOSC)	T11
	2008-08-01	151	4500-7700	6	MDM/Modspec	M10
	2008-12-08	280	4200-7700	24	Mt Ekar (AFOSC)	T11
	2008-01-25	328	4150-8000	7	MMT/Blue channel	M10
	2009-02-25	359	5200-9200	16	TNG (DOLORES)	T11
	2009-04-22	415	4200-7800	11	MDM/CCDS	M10
2009-05-16	439	4000-6500	11	MDM/CCDS	M10	
SN 2011dh	2011-09-07	99	3300-10500	12	CA-2.2m (CAFOS)	E13
	2011-10-30	151	3700-8200	?	AS-1.22m (AFOSC)	E14
	2011-12-19	201	3200-10000	8.2/15	WHT (ISIS)	E14
	2012-03-19	293	3200-9100	16	NOT (ALFOOSC)	E14
	2012-05-24	360	3400-10000	21	GTC (OSIRIS)	E14
	2012-07-20	415	3600-7000	17	GTC (OSIRIS)	E14

Table 2. Ejected elemental masses in the KEPLER models (assuming $M_{\text{Henv}} = 0.1 M_{\odot}$ and $M(^{56}\text{Ni}) = 0.075 M_{\odot}$), for different M_{ZAMS} . Ejecta that we model in this paper are marked with an asterisk.

M_{ZAMS} (M_{\odot})	M_{total}	M_{He}	M_{C}	M_{O}	M_{Na}	M_{Mg}	M_{Si}	M_{Ca}	$M_{^{56}\text{Ni}}$	M_{others}
12*	1.7	1.0	0.081	0.30	8.3×10^{-4}	0.020	0.042	0.0027	0.075	0.17
13*	2.1	1.1	0.10	0.51	5.6×10^{-4}	0.043	0.063	0.0037	0.075	0.21
14	2.3	1.2	0.12	0.66	7.8×10^{-4}	0.050	0.063	0.0036	0.075	0.26
15	2.5	1.2	0.15	0.78	2.1×10^{-3}	0.045	0.065	0.0038	0.075	0.22
16	2.8	1.2	0.17	0.88	3.8×10^{-3}	0.045	0.030	0.0025	0.075	0.32
17*	3.6	1.2	0.19	1.3	6.4×10^{-3}	0.074	0.16	0.011	0.075	0.55
18	3.7	1.3	0.17	1.6	1.6×10^{-3}	0.14	0.10	0.0036	0.075	0.39

3.2. Ejecta structure

A major challenge to SN spectral modeling is the complex mixing of the ejecta that occurs as hydrodynamical instabilities grow from asymmetries in the explosion itself and from the reverse shocks being reflected from the interfaces between the nuclear burning layers. In contrast to Type IIP SNe, the small ($\sim 0.1 M_{\odot}$) H envelopes in Type IIb explosions renders Rayleigh-Taylor mixing at the He/H interface inefficient (Shigeyama et al. 1994). The consequence is that the hydrogen becomes confined to a high velocity interval ($v \gtrsim 10^4 \text{ km s}^{-1}$), as evidenced by the spectra of SN 1993J, SN 2008ax, and SN 2011dh (Ergon et al. 2013). Spectral modeling of SN 1993J by Houck & Fransson (1996) confirmed that any H mass mixed below 5000 km s^{-1} must be very small.

However, asymmetries in the explosion itself and reverse shocks from the Si/O and O/He interfaces may still cause significant mixing of the inner layers. Linear stability analysis and 2D hydrodynamical simulations show that such mixing can be extensive, especially for low-mass helium cores (Shigeyama et al.

1990; Hachisu et al. 1991, 1994; Nomoto et al. 1995; Iwamoto et al. 1997). Such strong mixing is supported by models of many Type Ib/IIb light curves (Shigeyama et al. 1990, 1994; Woosley et al. 1994; Bersten et al. 2012; Ergon & Jerkstrand 2014).

The consequence of this large-scale mixing is that the final hydrodynamic structure of the ejecta is likely to be significantly different from the one obtained in 1D explosion simulations. **We adopt a model scenario where significant mixing is taken to occur in these explosions. This is further supported from the fact that all observed major metal emission lines have similar profiles.** Lacking any published grids of multidimensional Type IIb explosions to use as input, we attempt to create realistic structures by dividing the ejecta into three major components, a well-mixed core, a He envelope, and a H envelope.

3.2.1. The core

The core is the region between 0 and 3500 km s^{-1} (which is the velocity roughly corresponding to the estimated **Half-Width at Zero Intensity** (HWZI) values in the three objects studied here,

see Ergon & Jerkstrand (2014)), where complete macroscopic (but not microscopic) mixing is applied. The core contains the metal zones (Fe/Ni/Co, Si/S, O/Si/S, O/Ne/Mg, O/C), and, based on the mixing between the O/He layers seen in the multidimensional simulations, 20% of the He/C layer.

Each zone in the core is distributed over $N_{\text{cl}} = 10^4$ identical clumps (see Jerkstrand et al. (2011) for how this is implemented). This number is constrained to be large ($\gtrsim 10^3$) by the fine-structure seen in the nebular emission lines (e.g. Ergon & Jerkstrand 2014), and from the significant fragmentation seen in the multi-D simulations.

This mixing treatment is referred to as the “medium mixing” scenario. We also run some models where we apply an even stronger mixing by putting 50% of the Fe/Co clumps out in the helium envelope, referred to as the “strong mixing” scenario (we do this by adding three equal-mass shells of ^{56}Ni into the He envelope between 3500 km s^{-1} and 6000 km s^{-1}). The motivation for this type of mixing treatment comes from constraints from the early-time light-curve (Bersten et al. 2012; Ergon & Jerkstrand 2014), which seems to require significant amounts of ^{56}Ni at high velocities. We leave investigation of completely unmixed models for a future analysis.

In most models we assume constant density throughout the core, except for the Fe/Ni/Co and Si/S clumps which expand in the substrate due to the first days of radioactive heating (e.g. Herant & Benz 1991). In Jerkstrand et al. (2012) a density contrast of a factor 30 between the Fe/Ni/Co zone and the other metal zones for the Type IIP SN 2004et was found. Lacking any calculations of the “Ni bubble” expansion in a Type Ib/Ib explosion, we assume here the same contrast, $\rho_{\text{Fe/Ni/Co}} = 1/30 \rho_{\text{O}}$, where ρ_{O} is the density of the oxygen zones in the corresponding model. We also allow some expansion of the Si/S zone (which contains some of the ^{56}Ni), taking $\rho_{\text{Si/S}} = 1/3 \rho_{\text{O}}$.

In some models, we investigate the effect of increasing the density of the oxygen zones. The liberated core volume is then allocated to the other zones in proportion to their mass.

3.2.2. The He envelope

We place alternating shells of He/C and He/N-zone material in a He envelope between $V_{\text{core}} = 3500 \text{ km s}^{-1}$ and $V_{\text{He/H}} = 11,000 \text{ km s}^{-1}$ (see Sect. 3.2.3 for this value for the He/H interface velocity). We take the density profile of the He envelope from the simulations of Bersten et al. (2012), rescaled with a constant to conserve the mass. Each pair of He/C-He/N shells have the same density, and the spacing between each pair is logarithmic with $V_{i+1}/V_i = 1.2$.

3.2.3. The H envelope

Outside the He envelope (between $11,000 \text{ km s}^{-1}$ and $25,000 \text{ km s}^{-1}$) we attach a H envelope of mass $0.1 M_{\odot}$, with mass fractions 0.54 H, 0.44 He, 1.2×10^{-4} C, 1.0×10^{-2} N, 5.6×10^{-3} O, with solar abundances for the other elements. This CNO alternation is based on the model for SN 1993J by Woosley et al. (1994), where there is significant mixing of CNO ashes into the base of the H envelope (see also Shigeyama et al. (1994)), and is in agreement with observational constraints of SN 1993J (Fransson et al. 2005). This envelope mass gives a total H mass in agreement with the constraints derived from the 0 – 100 day phase by Ergon et al. (2013).

The inner velocity of the hydrogen envelope ($11,000 \text{ km s}^{-1}$) is determined by H α absorption line seen during the first 100

days (Ergon et al. 2013). We use a density profile of $\rho(V) \propto V^{-6}$, which is a rough fit to the Type IIB ejecta models by Woosley et al. (1994). The H shells are spaced logarithmically with $V_{i+1}/V_i = 1.1$. We terminate the envelope at $25,000 \text{ km s}^{-1}$, beyond which little gas exists.

3.3. Molecules

The formation of molecules has a potentially large impact on the thermal evolution of the ejecta in the nebular phase. That molecules can form in stripped-envelope SNe was evidenced by the detection of the CO overtone in Type Ic SN 2002ec at 100 days (Gerardy et al. 2002). A second detection was reported for the Type Ic SN 2007gr (Hunter et al. 2009), where high observational cadence showed the onset of CO overtone emission at somewhere between 50–70 days. For Type Ib and IIB SNe, there have been no previous detections of CO, although a feature seen around $2.3 \mu\text{m}$ in SN 1993J at 200 and 250 days (Matthews et al. 2002) could possibly be due to the CO overtone.

Our code does not contain a molecular chemical reaction network, so we are forced to parametrize their formation and impact on ejecta conditions. Here, we compute models in two limits : complete molecular cooling of the O/Si/S and O/C layers, and no molecular cooling. In the models with molecular cooling, we follow our previous treatment of molecular cooling in Type IIP ejecta (J12), assuming that CO dominates the cooling of the O/C zone and SiO of the O/Si/S zone. We fix the temperature evolution of these zones to be the ones derived for SN 1987A (Liu et al. 1992; Liu & Dalgarno 1994). If molecular cooling is strong, the optical/NIR spectrum is not sensitive to the exact value of this temperature.

To compute model NIR and MIR photometry, we need to specify how the molecular cooling is divided between fundamental and overtone bands. For CO we make a division between fundamental band ($4.5 \mu\text{m}$) and first overtone band ($2.3 \mu\text{m}$) as observed in SN 1987A (Bouchet & Danziger 1993). For SiO, no empirical constraints on this division exists. We assume a time-evolution of the division between fundamental band ($8.1 \mu\text{m}$) and first overtone band ($4.1 \mu\text{m}$) in the same way as for CO.

To compute the photometry, we assume box-like emission profiles between $4.4\text{--}4.9 \mu\text{m}$ (CO fundamental band), $2.25\text{--}2.45 \mu\text{m}$ (CO first overtone), and $4.0\text{--}4.5 \mu\text{m}$ (SiO first overtone).

3.4. Dust

As with molecules, formation of dust in the ejecta has a potentially large impact on physical conditions and the emergent SED. No clear dust detection in stripped-envelope SNe has so far been presented in the literature, although in SN 1993J, a strong continuum component, detectable in K and L' bands, arose in the SED after 100 days (Matthews et al. 2002), and was interpreted as possibly coming from dust forming in the ejecta.

The higher expansion velocity in H-poor SNe leads to two opposing effects on the thermal evolution and thereby the dust formation epoch. The gamma-ray trapping is lower, lowering the heating rates, and the density is lower, lowering the cooling rates. The opposing trends make it unclear whether dust formation is expected to occur earlier, at similar time, or later than in hydrogen-rich SNe.

We compute models both with and without dust. We model the dust as a smooth gray opacity in the core region of the SN, simply set to turn on at some given time. We reemit the flux absorbed by the dust in the radiative transfer simulations as a black-

body whose surface area is given by $A_{\text{dust}} = x_{\text{dust}} A_{\text{core}}$, where $x_{\text{dust}} = f^{2/3} N_{\text{cl}}^{1/3}$, which comes from equating $A_{\text{dust}} = 4\pi R_{\text{cl}}^2 N_{\text{cl}}$ and $4\pi/3 R_{\text{cl}}^3 N_{\text{cl}} = V_{\text{dust}}$. For a filling factor $f = 0.1$ and $N_{\text{cl}} = 10^4$, the x_{dust} factor is then 5. The exact value of x_{dust} mainly affects the K band and the mid-infrared bands, and is discussed in more detail in Ergon & Jerkstrand (2014).

3.5. Positrons

About 3% of the ^{56}Co decay energy is emitted in the form of positron (kinetic) energy. Since their absorption cross sections is much higher than that of the gamma-rays, they will come to dominate the power budget when the optical depth to the gamma-rays falls below ~ 0.03 . For typical ejecta masses and energies, this transition will take place around 1-2 years (e.g. Sollerman et al. 2002).

The trajectories of the positrons, and in turn which zones they deposit their energy in, depend on the magnetic field in the SN ejecta, which is unknown. Here we treat the positrons in two limits; $B \rightarrow \infty$ (on-the spot absorption) and $B = 0$ (**transport assuming no magnetic deflection with an opacity $\kappa_{e^+} = 8.5 (\bar{Z}/\bar{A}/0.5) \text{ cm}^2 \text{ g}^{-1}$ (Axelrod 1980; Colgate et al. 1980), where \bar{A} is the mean atomic weight and \bar{Z} is the mean nuclear charge. We refer to these two cases as “local” and “non-local”.**

3.6. Overview of models

Table 3 lists the properties of the various models that we run. All models have a ^{56}Ni mass of $0.075 M_{\odot}$, a metal core between 0 and 3500 km s^{-1} , a He envelope between 3500 and 11000 km s^{-1} , and a H envelope between 11000 and 25000 km s^{-1} . We investigate dependencies on progenitor mass, ^{56}Ni mixing, positron treatment, molecular cooling, dust formation, and oxygen zone density. The lowest progenitor mass in the KEPLER grid is $12 M_{\odot}$ and we can therefore not analyze models below this mass. We will find that metal emission lines from $M_{\text{ZAMS}} = 17 M_{\odot}$ ejecta are already stronger than the observed lines in the IIb objects, and we therefore do not investigate models from higher masses.

Table 4 shows the model combinations that only differ in one parameter. These are useful to see how each single parameter affects the model spectra in the figures to come.

4. Results

We now review the results of the model calculations by comparing model spectra with observed ones, and discuss line formation element by element. All model spectra shown have been convolved with a Gaussian with $R = 250$.

Of the models presented in Table 3, model 12C ($M_{\text{ZAMS}} = 12 M_{\odot}$, strong mixing, local positron absorption, no molecular cooling, dust formation at 200 days, and $\rho(\text{O-zones}) = 2.1 \times 10^{-13} \text{ g cm}^{-3}$) shows promising overall agreement with the spectral evolution of SN 2011dh (Figs. 1, 2). In particular, this model reproduces the $UBVRI$ light curve to ± 0.1 dex in the 100-500 day interval (see Ergon+2014), the evolution of the [O I] $\lambda\lambda 6300, 6364$ lines (Fig. 8), as well as those of other major emission lines.

In the following sections we analyze the spectra by discussing the signatures of the main elements in the ejecta one by one. We aim to illuminate the basic line formation processes for the most common elements in stripped envelope SN ejecta,

and derive abundance constraints where possible. As oxygen and magnesium have particularly strong and distinct lines in stripped-envelope CCSNe, attempts to thoroughly understand their formation and diagnostic potentials are particularly warranted.

In some sections we present line luminosity measurements from both observed and modelled spectra. Such quantities are not strictly well-defined for SN spectra due to strong line blending by both individual strong lines and by the forest of weak lines that make up the quasi-continuum (Li & McCray 1996). Asymmetries and offsets from the rest wavelength cause further complications. These issues make it preferable to perform the line luminosity extractions by automated algorithms, rather than “by-eye” selections of continuum levels and integration limits. The advantage of this process is that it is well defined, removes bias, and is repeatable by others. The disadvantage is that the algorithms may fail in capturing the right feature when strong blending or large offsets are present. We therefore always make manual inspections of the fits to ensure this does not happen.

The algorithm we apply is as follows : for a given SN we select a velocity V_{line} that represents typical emission line widths. For the SNe in this paper we use $V_{\text{line}} = 3500 \text{ km s}^{-1}$ for SN 2011dh, $V_{\text{line}}=4500 \text{ km s}^{-1}$ for SN 2008ax, and $V_{\text{line}} = 4500 \text{ km s}^{-1}$ for SN 1993J (SN 2008ax and SN 1993J have somewhat broader lines than SN 2011dh). For the models (which all have $V_{\text{core}} = 3500 \text{ km s}^{-1}$) we use $V_{\text{line}} = 3500 \text{ km s}^{-1}$. **We identify the minimum flux values within $[\lambda_0^{\text{left}} \times (1 - 1.25V_{\text{line}}/c), \lambda_0^{\text{left}}] = [0.985\lambda_0^{\text{left}}, \lambda_0^{\text{left}}]$ on the left side and $[\lambda_0^{\text{right}}, \lambda_0^{\text{right}} \times (1 + 1.25V_{\text{line}}/c)] = [\lambda_0^{\text{right}}, 1.015\lambda_0^{\text{right}}]$ on the right side², and take the continuum to be the line connecting these points. The line luminosity is then taken as the integral of the flux minus this continuum, with contributions only if the flux at a particular wavelength is higher than the continuum level.**

While the luminosity is automatically extracted, we estimate the error bars on each measurement by manual inspection of how complex the line blending appears to be, and whether some flux could be missed due to asymmetric or offset lines. The quantities that we plot and compare **between observations and models**, line luminosities relative to the ^{56}Co decay power

$$L_{\text{norm}}(t) = \frac{L_{\text{line}}(t)}{9.92 \times 10^{41} \frac{M_{^{56}\text{Ni}}}{0.07M_{\odot}} (e^{-t/111.4 \text{ d}} - e^{-t/8.8 \text{ d}})} \text{ erg s}^{-1}, \quad (1)$$

are independent of distance (and thereby to errors in this) and relatively insensitive to the extinction (and errors in this), **(as the ^{56}Co mass is determined in a phase where the bulk of the radiation emerges in the optical bands). Instead, the systematic error corresponds to the uncertainty in ^{56}Co mass determined for a given distance and extinction, i.e. in the theoretical bolometric corrections..** This uncertainty is of order 10% for all SNe analyzed here, which is always smaller than the estimated statistical errors.

4.1. Individual elements

4.1.1. Hydrogen lines

The hydrogen envelope of $0.1 M_{\odot}$ receives little of the energy input from ^{56}Co , typically around 0.5% at all epochs in the

² For lines with several components (e.g. [Ca II] 7291, 7323) we use the shortest wavelength on the left side (λ_0^{left}) and the longest wavelength on the right side (λ_0^{right}). For single lines $\lambda_0^{\text{left}} = \lambda_0^{\text{right}} = \lambda_0$.

Table 3. Properties of models computed. Further description can be found in the main text of Sect. 3.

Model	M_{ZAMS} (M_{\odot})	Mixing	e ⁺	Mol. cooling	Dust	ρ_{O} 100 d (10^{-14} g cm ⁻³)	other (TEMPORARY)
12A(49)	12	Medium	Free	O/Si & O/C	No	6.5	star, 12-dh1
12B(55)	12	Strong	Free	None	Yes ¹	21	dell, 12-dh17
12C(59)	12	Strong	Local	None	Yes ¹	21	dell, 12-dh18(?)
13A(43)	13	Medium	Free	O/Si & O/C	No	6.5	sn, 13-dh11
13B(46)	13	Medium	Local	O/Si & O/C	No	6.5	dell , 13-dh11
13C(50)	13	Strong	Free	O/Si & O/C	No	4.1	star, 13dh-15
13D(51)	13	Strong	Free	O/Si & O/C	Yes ¹	4.1	sn, 13-dh15
13E(52)	13	Strong	Free	O/Si & O/C	No	21	star, 13-dh16
13F(60)	13	Strong	Local	None	Yes ¹	21	star, 13-dh16
17A(56)	17	Strong	Local	None	Yes ¹	21	star, 17-dh3

1 : $\tau = 0.25$ from 200d, $x_{area} = 0.1$ **Table 4.** Model combinations that only differ in one parameter. The value of the parameter is given in parenthesis.

Parameter	Model combination
Mass (3 values)	12C (12), 13F (13), 17A (17) 12A (12), 13A (13)
Mixing (2 values)	none
e+ (2 values)	12B (local) and 12C (free) 13A (free) and 13B (local)
Mol. cooling (2 values)	none
Dust (2 values)	13C (no dust) and 13D (with dust)
O-zone density (3 values)	13C (4.1×10^{-14}) and 13E (21×10^{-14})

100 – 500 day range. This is too little to produce any detectable emission lines in the steady-state models. The observed line around 6550 Å is instead dominated by [N II] $\lambda\lambda 6548, 6583$ cooling of the He/N layers (Fig. 6, Sect. 3.2).

Some caution is needed in this conclusion though, because the dilute hydrogen envelope is the first region to be affected by time-dependent effects. Its low density leads to both the cooling time-scale and the recombination time-scale becoming comparable to (and then exceeding) the radioactive decay time scale already after ~ 100 -200 days. This will lead to temperature and ionization balance differing from a steady-state calculation (Fransson & Kozma 1993). Whether the H emission may become strong enough to be detectable under the influence of this time-dependence has to be investigated with such modeling. We note, however, that the ionization level in the steady-state model is $x_{\text{HII}} \sim x_e \gtrsim 1/3$ and so even in complete freeze-out ($x_{\text{HII}} \sim x_e \sim 1$), the recombination lines would be at most an order of magnitude brighter (the recombination rate scales with $x_{\text{HII}} \cdot x_e$). As Fig. 6 shows, this would still be too little to match the [N II] $\lambda\lambda 6548, 6583$ luminosity. It therefore appears to be a robust result that (⁵⁶Co-powered) H α is undetectable after ~ 200 days in Type IIB SNe.

All lines in the Balmer series (and higher n) are optically thin after ~ 150 days, also preventing any P-Cygni components to form. Our conclusion is therefore that the H envelope can contribute neither emission nor absorption in H lines after ~ 150 days. This result agrees with the analysis of SN 1993J by Houck & Fransson (1996), who found that the H α emission in their models was inadequate to account for the observed flux around 6550 Å. They did not include N II in their spectral calculations, and here we have likely solved the discrepancy by adding this atom.

In SN 1993J, circumstellar interaction started dominating the output of the SN after about a year, leading to a leveling off in all photometric bands to almost constant flux levels (e.g. Zhang et al. 2004). The 6500-6600 region then became dominated by (true) H α from the circumstellar interaction, showing a boxy line profile with almost constant flux (Filippenko et al. 1994; Houck & Fransson 1996). This interpretation is validated by similar H β and H γ emission lines emerging in the spectrum. Circumstellar interaction is expected both in single star scenarios and in binary progenitor systems (where the Roche lobe overflow mass transfer typically ejects $\sim 50\%$ of the mass (Yoon et al. 2010)). No such flattening has occurred in SN 2011dh, at least up to 500 days, and the spectral region continues to be dominated by the [N II] $\lambda\lambda 6548, 6583$ line.

Before ~ 150 days, H α is optically thick and will affect the spectrum with absorption (Maurer et al. 2011). If the bulk of the photons are emitted from a core region with a velocity scale much smaller than the inner velocity of the H-envelope, this absorption will be in the form of a band centered at $\lambda_c \sim 6563 (1 - V_H/c) \sim 6320$ Å, with a width governed by the velocity distribution of both the hydrogen layer and the emitting region. The width will roughly correspond to the larger of these velocity scales. Since they are both of order a few thousand km s⁻¹, the width of the absorption band will be $\Delta\lambda \sim 2\Delta V/c\lambda_c \sim 150$ Å, where we have used $\Delta V \sim 3500$ km s⁻¹. Ergon et al. (2013) shows how SN 1993J, SN 2008ax, and SN 2011dh all have such distinct absorption bands throughout the 0 - 100 day evolution, all with absorption minima corresponding to $V_H \sim 10^4$ km s⁻¹, and the identification with H α secured by a similar band seen in H β . Whereas the feature continuously fades in SN 2008ax and SN 2011dh, it remains strong in SN 1993J, likely as the hydrogen envelope mass was higher in this SN (Woosley et al. 1994).

The absorption band emerges in the models at 100 days (Fig. 1). It leads to a complex line profile, where [O I] $\lambda 6364$ is cut off by H α absorption **redward of** 6350 Å, ($\approx \lambda_c + 1/2\Delta\lambda_c = 6390$ Å). The absorption reaches its maximum at 6315 Å ($\approx \lambda_c = 6320$ Å) and ceases at 6260 Å ($\approx \lambda_c - 1/2\Delta\lambda = 6250$ Å). The observed profile shows a similar structure, with a minimum at 6325 Å, a cut-off to the left at 6275 Å, but no clear cut-off to the right. The region is complex, with an [Fe II] line coming in on the red side. It is clear that the absorption in the model is stronger than in the observed spectrum, and it is therefore unlikely that the hydrogen density in the model could be underestimated. Finally, we note that H β and the other Balmer lines are optically thin in the model in the time interval studied here, and therefore do not produce

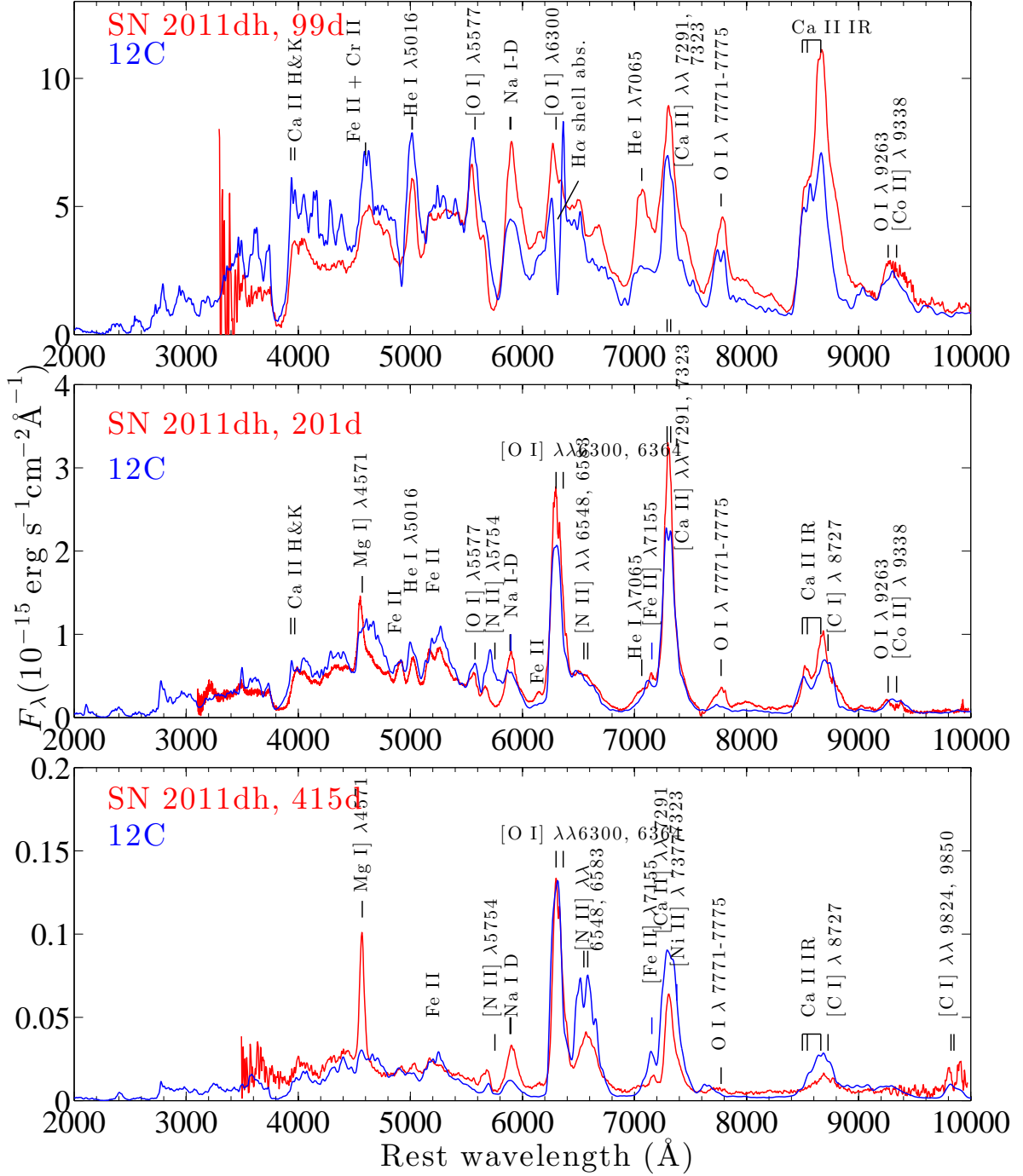


Fig. 1. SN 2011dh (dereddened and redshift corrected) at 99 days (top), 201 days (middle), and 415 days (bottom) (red) and model 12C at 100, 200, and 400 days (blue), scaled with exponential factors $\exp(-2\Delta t/111.4)$, where Δt is the difference between observed and modelled phase (here $\Delta t = -1$ day). The decay rate of double the ^{56}Co rate corresponds to the evolution in most bands (Ergon & Jerkstrand 2014).

any similar absorption bands (which would occur at $\sim 4690 \text{ \AA}$ and 4180 \AA for $\text{H}\beta$ and $\text{H}\gamma$.)

4.1.2. Helium lines

He line formation in the nebular phase is complex, as He resides in several chemically distinct regions in the SN. CNO-burning leaves the progenitor with a He/N layer enriched in nitrogen and depleted in carbon. The inner parts of this zone later become

enriched in carbon and oxygen from convective mixing with the helium-burning shell. The resulting He/C layer is then mixed to an uncertain extent with core material in the explosion, when the shock wave passes the O/C-He/C interface. Freeze-out from nuclear statistical equilibrium also leaves a large mass fraction ($\sim 20 - 50\%$) of He in the ^{56}Ni clumps. Despite the much lower mass of He in these clumps compared to that in the He/N and He/C zones, this He can contribute strongly to the total He line

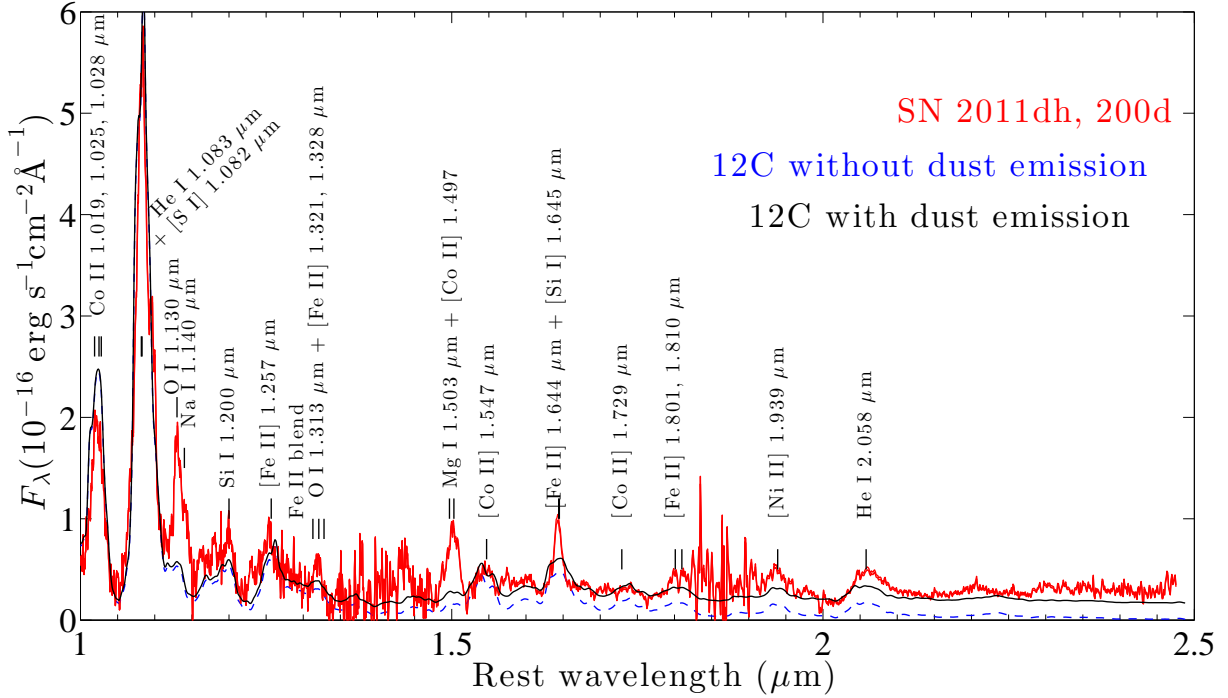


Fig. 2. SN 2011dh (dereddened and redshift corrected) in the NIR at 200 days (red; The observed spectrum is composed of 1-1.5 μm observations at 198 days scaled with $\exp(-2 \times 2/111.4)$ and 1.5 – 2.5 μm observations at 206 days, scaled with $\exp(+2 \times 6/111.4)$) and model 12C without (blue) and with (black) a dust component ($\tau = 0.25$, $V_{\text{dust}} = 3500 \text{ km s}^{-1}$, $x_{\text{dust}} = 0.05$). Line identifications from the model are labelled. A dust component clearly improves the spectral fit above 1.5 μm .

emission due to the high energy deposition in the ^{56}Ni clumps (e.g. Kjær et al. 2010).

He-line analysis must thus consider contributions from three distinct zones (and possibly from the He in the H envelope as well). We find the He/C and He/N zones in the envelope and the He in the ^{56}Ni clumps to all significantly contribute to the He lines, with a smaller contribution by the mixed-in He/C clumps.

At all epochs, He I 1.083 μm is the strongest He emission line in the models. There is however significant blending of this line with [S I] 1.082 μm , and the observed feature can therefore not be interpreted as arising from He I alone. This conclusion was also reached for SN 1987A (Li & McCray 1995; Kozma & Fransson 1998). A corollary of this result is that the presence of He in any SN cannot reliably be established by observation of this emission line only. The only other S I line with significant emission is S I 9213 Å, which is still about an order of magnitude weaker than the [S I] 1.082 μm line, and is therefore difficult to detect.

He I 2.058 μm does not suffer from any significant line blending, and detection of this line therefore *is* sufficient for establishing the presence of He in the SN ejecta. The line is optically thick in the Fe/He clumps, in the in-mixed He clumps, and in the inner He envelope for several hundred days, leading to a P-Cygni component in the line profile (or rather its equivalent form in the nebular phase **where the peak is redward of the rest wavelength**, see Friesen et al. (2012)). Such a P-Cygni component is clearly visible in the observed spectra at 200 days.

In Fig. A.1 we plot the contribution of He lines to the model spectrum at 100, 300 and 500 days. In the optical, the strongest model lines are those at 3614 Å (this is from highest level 29, why so strong?), 3889 Å, 5016 Å, 6678 Å, and 7065 Å. Neither

of these lines are strong compared to the optical spectrum as a whole, and will be difficult to detect in the nebular phase. Note also how He I 1.083 μm typically contributes only $\sim 50\%$ to the feature at that wavelength. He I $\lambda 5876$ does not emerge directly in the model, as most of its flux scatters in the Na I-D lines (Sect. 4.1.6).

4.1.3. Carbon lines

Fig. A.2 shows the contribution by carbon (completely dominated by C I emission) to the spectrum. The emission is mainly from the carbon in the O/C zone, but there is also a contribution from the carbon dredged up into the He/C layer (this component in particular dominates the strong [C I] $\lambda 8727$ emission at late times). **Apart from this line**, also [C I] $\lambda\lambda 9824, 9850$, C I 1.176 μm , C I 1.454 μm and a group of lines between 9060 – 9111 Å are emitting at detectable levels.

4.1.4. Nitrogen lines

As discussed above in the hydrogen lines section, cooling of the $\sim 1 M_{\odot}$ He/N envelope by [N II] $\lambda\lambda 6548, 6583$ is responsible for almost all emission in this wavelength range, exceeding the H α contribution after ~ 150 days. The [N II] lines naturally obtain rather flat-topped profiles as most of the He/N layers expand with high velocities. Our models (which are dominated by [N II]) do a satisfactory reproduction of the feature also in SN 1993J and SN 2008ax (Figs. 4 and 5). However, by 400 days H α has completely taken over in SN 1993J (Fig. 7).

Since the [N II] identification is an important result, it is warranted to understand how robust it is. The first question is how

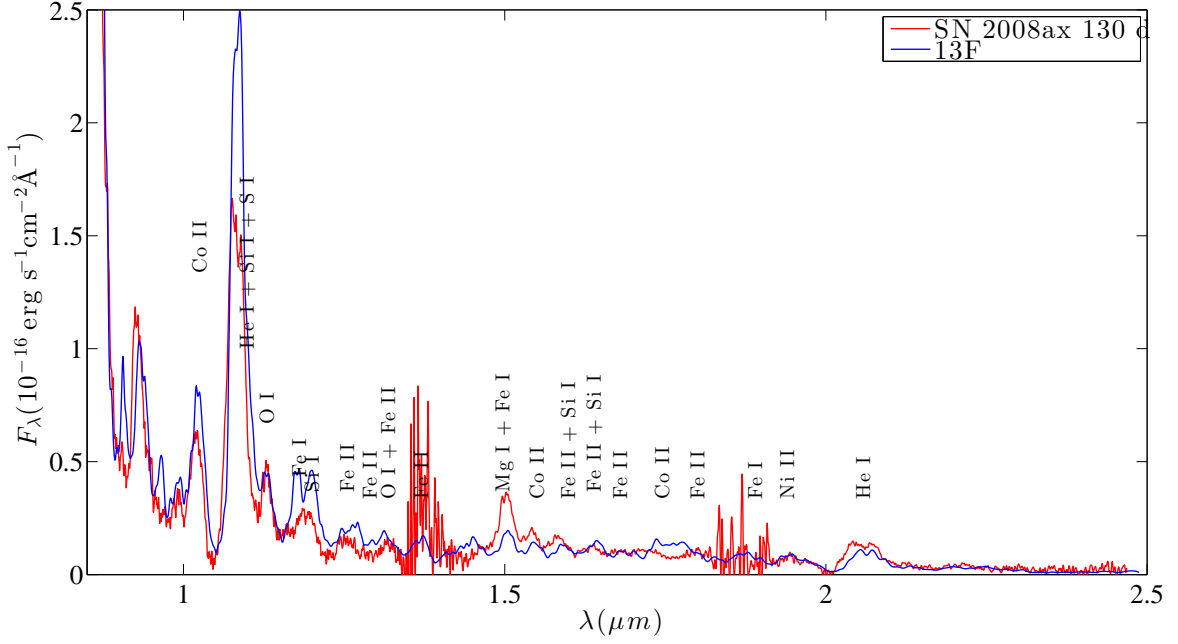


Fig. 3. SN 2008ax (dereddened and redshift corrected) in the NIR at 130 days (red) and model 13F. Line identifications from the model are labelled. The observed spectrum has been rescaled to the same ^{56}Ni mass as used in the model.

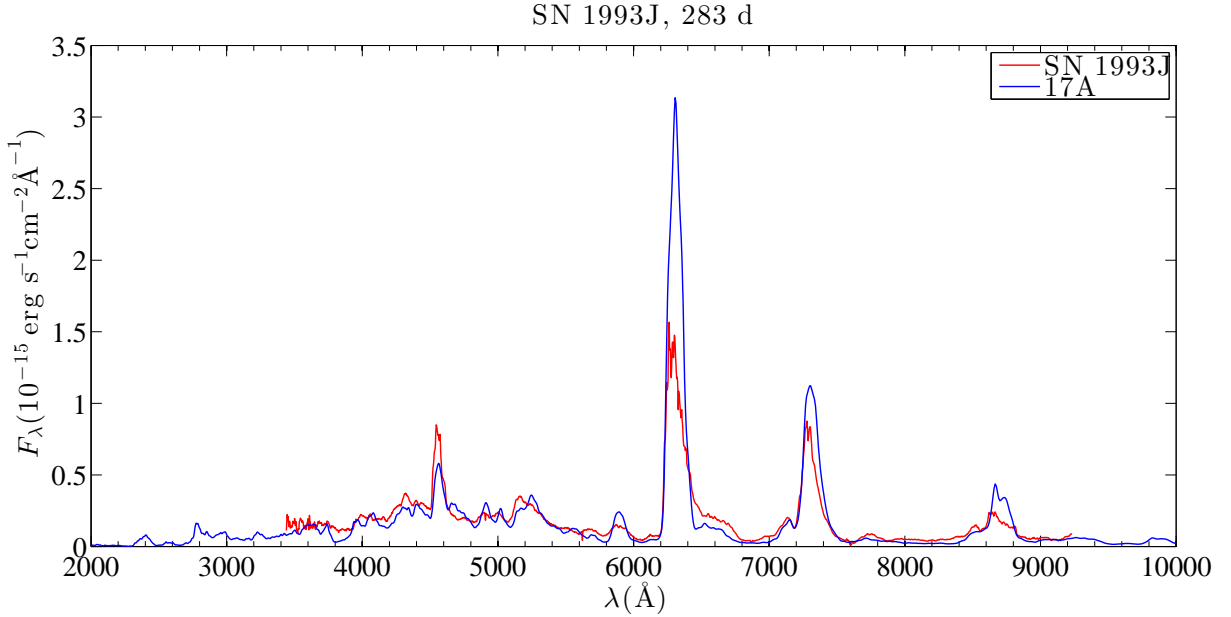


Fig. 4. Same as Fig. 1, for SN 1993J at 283 days (red), and model 17A at 300 days (blue). The observed spectrum has been rescaled to the same ^{56}Ni mass as used in the model.

large the helium layer is in the SN. All KEPLER models in the 12-20 M_{\odot} range have total He zone masses between 1.1 – 1.3 M_{\odot} . The fraction that is still rich in N, i.e. has not been mixed with metals in a second dredge-up, is 80% at the low-mass end and 30% at the high mass end. The mass of the He/N layer thus varies by about a factor two over the 12 – 20 M_{\odot} range, from 0.9 to 0.4 M_{\odot} . The prediction would be that ejecta from lower mass stars have stronger [N II] $\lambda\lambda 6548, 6583$ emission lines.

The [N II] $\lambda\lambda 6548, 6583$ are similar to the [O I] $\lambda\lambda 6300, 6364$ lines : they are transitions from the first excited state to the

ground state, and have similar A-values ($A = 3.9 \times 10^{-3} \text{ s}^{-1}$ for [N II] versus $A = 8 \times 10^{-3} \text{ s}^{-1}$ for [O I]). The [N II] lines have about an order of magnitude higher collision strengths. The nitrogen abundance in the He/N layer is about 1%, but although small there are even smaller amounts of other possible cooling agents (carbon, oxygen, magnesium, silicon and iron all have mass fractions of $\sim 10^{-3}$). Helium makes up $\sim 98\%$ of the zone mass, but being a poor coolant itself, the He/N layers are quite hot **compared to the other zones**. The fraction of the nitrogen that is singly ionized is very close to unity, so there should not

SN 2008ax, 328 d

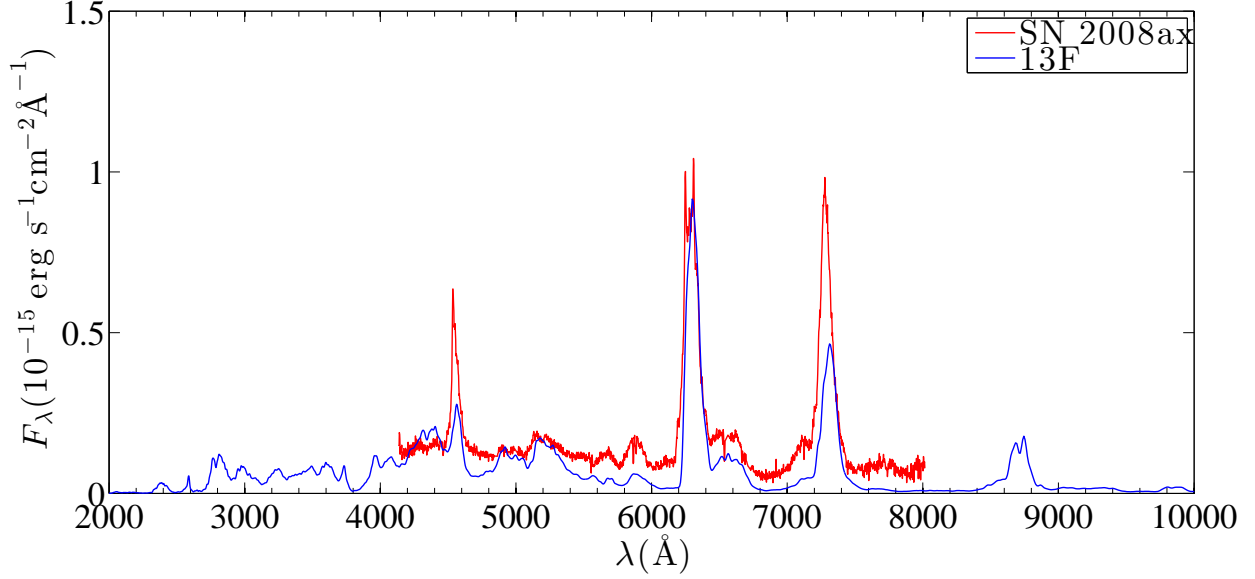


Fig. 5. Same as Fig. 1, for SN 2008ax at 307 days (red), and model 13F at 300 days (blue). The observed spectrum has been rescaled to the same ^{56}Ni mass as used by the model.

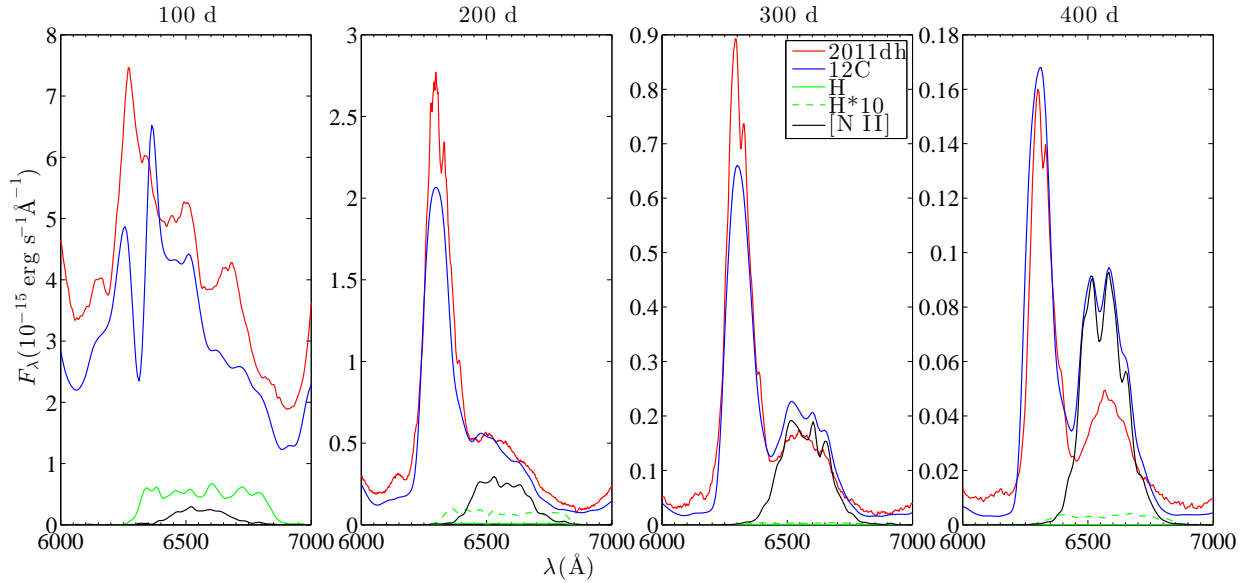


Fig. 6. The contribution by $\text{H}\alpha$ (solid green) and $[\text{N II}] \lambda\lambda 6548, 6583$ (black) to the total emission (blue) in the $6000 - 7000 \text{ \AA}$ range, in model 12C at 100, 200, 300, and 400 days. Also shown at 200, 300, and 400 days is the H contribution multiplied by 10 (dashed green). From 200 days and on, the $[\text{N II}]$ lines are fully responsible for the feature between $6500 - 6600 \text{ \AA}$. Observations of SN 2011dh in red (spectra at 99, 201, 293, and 415 days scaled with $\exp(\Delta t/111 \text{ d})$ factors).

be any strong sensitivity to the ionization balance of nitrogen. Combining these results - moderate variations in the predicted mass of the He/N layer, a robust prediction for a high temperature, and no sensitivity to the nitrogen ionization balance, strong $[\text{N II}] \lambda\lambda 6548, 6583$ emission appears to be a robust property of the models. Of course, the question that then arises is why we do not see this line in the nebular phase of Type Ib SNe. Reviewing published nebular spectra of Type Ib SNe, we find several Type Ib SNe to in fact display a prominent emission line at this wavelength - SN 1996N (Sollerman et al. 1998), SN 2007Y of these

to display an emission line that can be either the $[\text{N II}]$ lines or $\text{H}\alpha$

One possible explanation is that Type Ib SNe have lost the outer He/N zone (but not the inner He/C zone) to stellar winds or binary mass loss. Another explanation could be that dredge-up from the C/O core has engulfed the entire He/N envelope in these stars and altered its chemical composition to a carbon and oxygen rich mixture. Either way, it is clear that the possible association of the 6550 \AA line with $[\text{N II}] \lambda\lambda 6548, 6583$ opens up many important and unresolved questions.

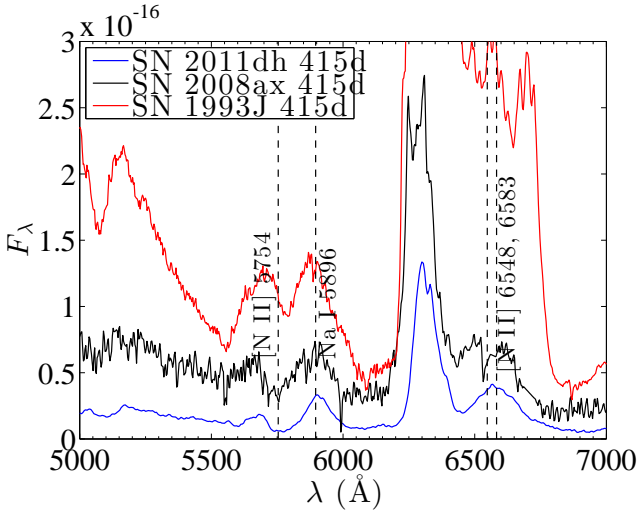


Fig. 7. The 5000 - 7000 Å region at 415 days in SN 2011dh (blue), SN 2008ax (black) and SN 1993J (red), all scaled to the same distance. We identify the feature at ~ 5700 Å with the blue side of [N II] $\lambda 5754$, with the red side being lost in scattering into Na I-D.

In Fig. A.3 we plot the contribution by nitrogen lines to the spectrum. The only other possibly detectable nitrogen line is [N II] $\lambda 5754$. The red side of this line scatters into the Na I-D lines. There is an emission feature in all 2011dh spectra centered at ~ 5670 Å that could be this line - it is also clearly seen in SN 1993J and SN 2008ax (Fig. 7). The blue edge goes to 5600 Å which would correspond to an expansion velocity of ~ 8000 km s $^{-1}$, making an identification with the helium envelope likely. Furthermore, our models confirm that Na I-D is optically thick throughout the He envelope also at 400 days (model 12C reaches a nominal $\tau = 1$ at 9000 km s $^{-1}$ at 400 days). The predicted absorption cut is thus around $5890 \text{ Å} \times (1 - 1 \times 10^4 / 3 \times 10^5) = 5700 \text{ Å}$, in good agreement with the observed line. The [N II] $\lambda 5754$ line **luminosity** in the model matches the observed one quite well, although the line profile it is too narrow. No other emission lines are predicted in the relevant range, further strengthening the identification.

After ~ 400 days, the model starts overproducing the [N II] $\lambda \lambda 6548, 6583$ line compared to observations of SN 2011dh. At this time, the adiabatic cooling has reached 3–26% in the various He/N layers. At 300 days it is 1 – 12%. It is thus plausible that the temperature computed with our steady-state models starts overestimating the true temperature in the outer helium envelope at ~ 400 days. However, the [N II] $\lambda 5754$ line is too weak in the model.

The nitrogen lines will almost certainly be optically thin and suffer no collisional deexcitation in the dilute helium envelope. **The [N II] $\lambda 5754$ /[N II] $\lambda \lambda 6548, 6583$ line ratio** is then expected to be 1.0 at 10000 K, 0.7 at 5000 K, and 0.017 at 2500 K. As the [N II] $\lambda 5754$ line appears to scatter significantly into the Na I-D lines its intrinsic luminosity can be only roughly determined.

4.1.5. Oxygen lines

Fig. 8 (and Fig. 23) show the flux in [O I] $\lambda \lambda 6300, 6364$ (relative to ^{56}Co) for SN 2011dh, SN 2008ax, and SN 1993J, compared to the models. For SN 1993J, we include data up to about one year, after which circumstellar interaction began to dominate the spectrum. All three SNe show oxygen nucleosynthesis matching stars in the $M_{\text{ZAMS}} = 12 - 16 M_{\odot}$ range (corresponding to

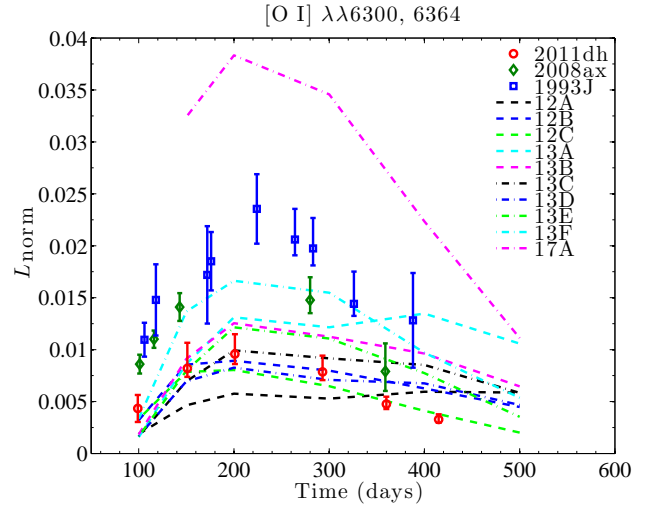


Fig. 8. The luminosity in [O I] $\lambda \lambda 6300, 6364$ normalized to the total ^{56}Co decay power (see Eq. 1) for SN 1993J, SN 2008ax, and SN 2011dh, and in the models.

oxygen masses $M_{\text{O}} = 0.3 - 0.9 M_{\odot}$). In the WH07 models, oxygen production grows sharply for progenitors over $\sim 16 M_{\odot}$, and none of these SNe show [O I] $\lambda \lambda 6300, 6364$ lines expected from such high-mass stars. Fig. 4 shows model 17A against SN 1993J at 300 days - there is good overall agreement with this model, although the oxygen lines are about a factor two too strong. As [O I] $\lambda \lambda 6300, 6364$ is an important and relatively parameter-insensitive diagnostic of the progenitor mass (J12, J13), there is thus support from nucleosynthesis analysis that low/moderate mass stars ($M_{\text{ZAMS}} \lesssim 16 M_{\odot}$) is a dominant progenitor population for Type IIb SNe.

An important property to constrain is the optical depth of the [O I] lines. In SN 1987A, the [O I] $\lambda \lambda 6300, 6364$ lines began to depart the optically thick 1:1 regime already at 100 days, and became fully optically thin ($\tau < 1$) around 400-500 days (Spyromilio & Pinto 1991; Li & McCray 1992). Since the expansion velocities here are about a factor two higher, the densities for a similar mass and filling factor are a factor eight lower. The $\tau = 1$ limit is then expected to be reached by ~ 100 days instead of 400.

Since $V_{\text{exp}} \gtrsim 3047$ km s $^{-1}$ (the 64 Å line separation between [O I] $\lambda 6300$ and [O I] $\lambda 6364$ Å), the two lines are blended and the individual components of the doublet cannot be directly extracted. Fig. 9 shows the best fit to the doublet line profile for an optically thin (black) and an optically thick (blue) model with Gaussian components. The optically thin version gives better fits at all times, although at 100 days neither fit is good, likely due to the line blending and radiative transfer effects discussed above. If we take the lines to have entered the optically thin regime at 150 days, we obtain an upper limit to the density of the oxygen³ of

$$\rho_{\text{O}}(150d) \lesssim 10^{-13} \text{ g cm}^{-3}. \quad (2)$$

This is about an order of magnitude higher than the typical density in the models, which all produce optically thin doublets. For the oxygen masses in 12, 13 and 17 M_{\odot} progenitors, this limit corresponds to filling factor limits $f_{\text{O}} \gtrsim 0.01, 0.03$ and 0.08. This result will later be useful in constraining the magnesium mass in the ejecta.

³ **Formally for the neutral oxygen, but since the ionization level is low, the total oxygen density is close to this value.**

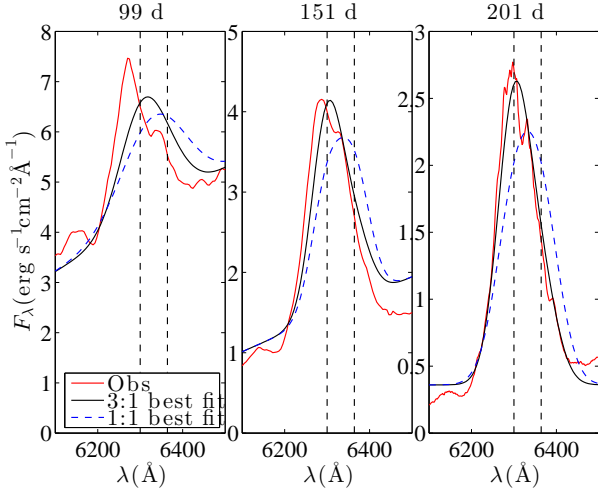


Fig. 9. The [O I] $\lambda\lambda 6300, 6364$ feature in SN 2011dh (red) and the best double Gaussian fits assuming optically thin (3:1) emission (black solid line) and optically thick (1:1) emission (blue dashed line). The optically thin fits are superior at all times.

Other oxygen lines we can identify with the models are [O I] $\lambda 5577$, O I $\lambda 7771$ ⁴, O I $\lambda 9263$ ⁵, O I $\lambda 1.130 \mu\text{m}$ and O I $\lambda 1.316 \mu\text{m}$. Most of the pumping of these lines is by recombination. However, [O I] $\lambda 5577$ arises from $2p^4(^1S)$ which is only 4.2 eV above the ground state and becomes populated by thermal collisions in the early nebular phase. Since the [O I] $\lambda\lambda 6300, 6364$ lines are **driven by thermal collisions** at all times, the [O I] $\lambda 5577$ /[O I] $\lambda\lambda 6300, 6364$ ratio can serve as a thermometer for the oxygen region. As discussed in Jerkstrand et al. (2013), this allows an estimate of the oxygen mass assuming LTE.

Fig. 10 shows the luminosity in [O I] $\lambda 5577$ and the ratio [O I] $\lambda 5577$ /[O I] $\lambda\lambda 6300, 6364$. It is noteworthy how similar the evolution of this line ratio is in the three SNe. Most of the models overproduce this ratio by a factor ~ 2 . Since both lines are driven by thermal collisions, one possibility is that the oxygen-zone temperatures are somewhat too high in the models. This in turn must be caused by either a too efficient gamma-ray deposition in the oxygen clumps, or an underestimate in their cooling ability.

The first situation can be improved on by increasing the separation between the ^{56}Ni clumps and the oxygen clumps. The second situation can possibly be remedied by changing the density of the oxygen clumps. Two opposing effects depend on the density - a higher density leads to more frequent collisions, which increases the efficiency of collisional cooling, but a higher density also leads to higher radiative trapping, which prevents the escape of the cooling radiation. Comparing models 13C and 13E, which only differ in that the O-zone density is higher in model 13E ($f_0 = 0.03$ vs $f_0 = 0.13$ for the thermally emitting O/Ne/Mg layer), model 13E has a higher O/Ne/Mg zone temperature (6060 K vs 5860 K at 150 days). The higher density also brings the [O I] $\lambda 5577$ parent state close to LTE, and the combined effect is a higher [O I] $\lambda 5577$ /[O I] $\lambda\lambda 6300, 6364$ line ratio. From this comparison, a high O-zone density is not favored by the [O I] $\lambda 5577$ /[O I] $\lambda\lambda 6300, 6364$ line ratio. This is however not consistent with the constraints imposed by oxygen and magnesium recombination lines (see below). There may

⁴ Three lines between 7771-7775 Å.

⁵ Nine lines between 9261-9266 Å.

thus be other issues that explain the [O I] $\lambda 5577$ /[O I] $\lambda\lambda 6300, 6364$ ratio discrepancy, such as line blending, line blocking, or molecular cooling. As Fig. 12 shows, there are strong [Fe II] lines contaminating both [O I] $\lambda 5577$ and [O I] $\lambda\lambda 6300, 6364$ at 100 days, and the discrepancy is possibly related to this line blending.

Radiative transfer effects further complicate interpretation of the line luminosities. Fig. 11 shows that the observed line profiles of both [O I] $\lambda 5577$ and [O I] $\lambda\lambda 6300, 6364$ evolve quite significantly between 100 and 200 days in SN 2011dh. At 100 days the peak of the lines are both blue-shifted by $\sim 1500 \text{ km s}^{-1}$. This likely arises as a result of line blocking by emission from the receding side of the ejecta. Note that the Na I-D line is not noticeably affected, as it is formed by scattering in the envelope and suffers little radiative transfer through the core. The blue-shifts of the oxygen lines gradually disappear by 200 days. Our interpretation is that both lines are affected by radiative transfer effects early on, but less so at later times.

This idea is supported by the model calculations which give significant line blocking throughout the optical region at 100 days. In Fig. 12 we show the model spectra at 100 and 200 days zoomed in on the oxygen lines. We obtain significant blue-shifts of [O I] $\lambda 5577$ and [O I] $\lambda\lambda 6300, 6364$ at 100 days, due to a combination of line blending and line blocking of the flux from the receding side (notice the lack of emergent [O I] $\lambda 6300$ emission redward of 6300 Å). At later times the line opacity decreases and the model gives more symmetric lines profiles, as observed in SN 2011dh as well as in most other stripped envelope SNe with respect to the [O I] $\lambda\lambda 6300, 6364$ lines (Taubenberger et al. 2009). In SN 2008ax and SN 1993J, the [O I] $\lambda 5577$ line also showed a $\sim 2000 \text{ km s}^{-1}$ blue-shifted peak at early times. In SN 2008ax the blue-shift slowly diminished with time (Milisavljevic et al. 2010) but in SN 1993J there was no discernible shift until the line disappeared (Spyromilio 1994).

In cases where no such changes occur for several hundred days, ejecta asymmetries are often invoked. The consistency of blueshifts in [O I] $\lambda 5577$ (no redshifted cases were observed in a sample of stripped-envelope SNe (Milisavljevic et al. 2010)) seem to make both asymmetries and line blending unlikely explanations. On a broader scale, all observed lines of Mg I $\lambda 4571$, [O I] $\lambda 5577$, [O I] $\lambda\lambda 6300, 6364$ **in this sample** are either symmetric or asymmetric towards the blue (Milisavljevic et al. 2010). **CHECK 2002ap (not that paper), redshifted** The only scenario that can explain such systematic line shifts towards the blue is selective absorption of emission from the receding side of the SN, which as discussed above is seen when the **detailed** radiative transfer problem is solved (Fig. 12). The temporal decrease of the line blocking depends on the density of the homogeneously expanding ejecta. One possible scenario is that the SNe which show slow line profile changes have high-density ejecta that maintain high line-blocking opacity for a longer time. The finding here that the nebular lines indicate an increasing progenitor mass along the sequence SN 2011dh - SN 2008ax - SN 1993J is consistent with this explanation. **Other factors, such as different velocities and temperature evolution, may also be responsible.**

We now turn our attention to the O I recombination lines to see what constraints are provided by these. There are four recombination lines predicted to be detectable by the model (Fig. A.4) and which are also clearly seen in the spectra : I $\lambda 7771$, O I $\lambda 9263$, O I $\lambda 1.130 \mu\text{m}$ and O I $\lambda 1.316 \mu\text{m}$. These are allowed transitions from high-lying states (excitation energies $> 10 \text{ eV}$) which cannot be populated by thermal collisions. The solutions to the energy deposition channels of the non-thermal electrons

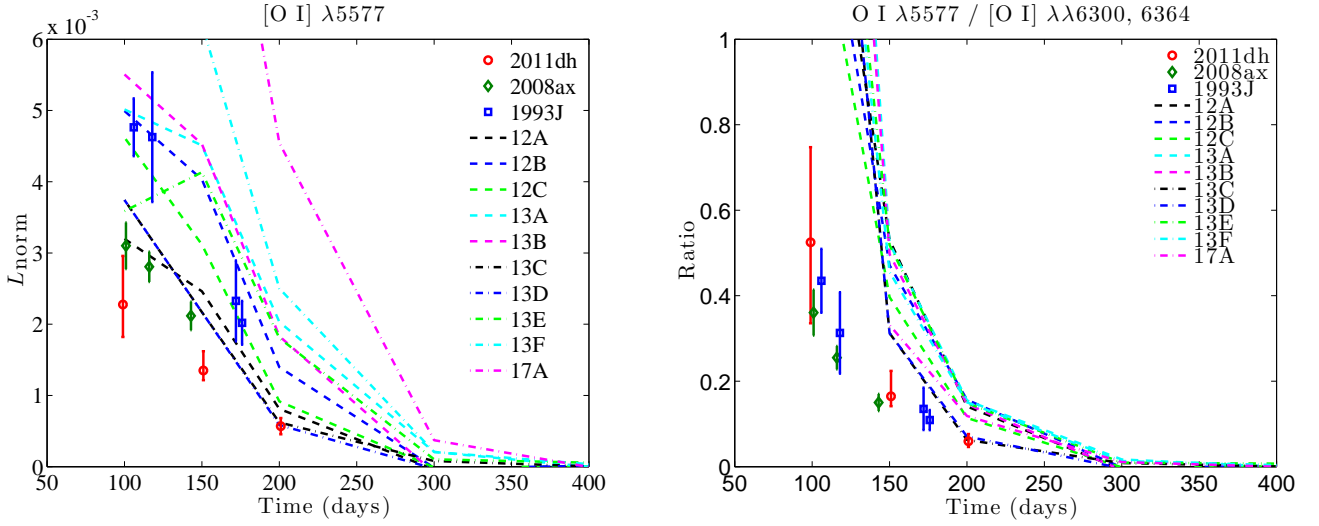


Fig. 10. Left : The luminosity in [O I] $\lambda 5577$ relative to the ^{56}Co decay power in the models and in SN 1993J, SN 2008ax, and SN 2011dh. Right: The [O I] $\lambda 5577$ / [O I] $\lambda\lambda 6300, 6364$ line ratio.

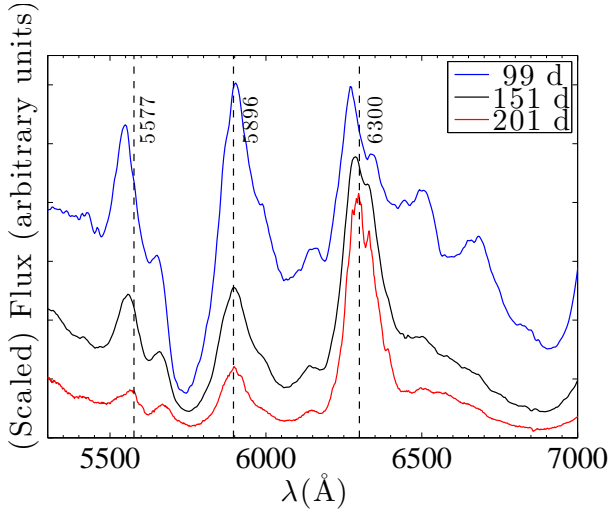


Fig. 11. Zoom-in on the [O I] $\lambda 5577$, Na I $\lambda\lambda 5890, 5896$ and [O I] $\lambda\lambda 6300, 6364$ lines in SN2011dh at 99, 151, and 201 days. Both oxygen lines show blue-shifted line profiles at 99 days, **but the peaks then gradually move towards zero velocity. The Na I D lines show no blueshift as they arise from the envelope rather than the obscured core.**

show that **at all epochs at least ten times more energy goes into ionizing oxygen than exciting it.** Emission lines from high-lying states are thus to a larger extent driven by recombination than by non-thermal excitations. **Note that O I 8446 has a recombination emissivity similar to these four lines, but this flux scatters and/or blends into the Ca II 8498, 8552, 8662 Å lines and is not directly observable.**

At early times $n_{\text{OII}} \approx n_e$ and the recombination line luminosity is

$$L_{\text{rec}}^{\text{ul}} = V_{\text{O}} n_e^2 \alpha_{\text{eff}}^{\text{ul}} h\nu_{\text{ul}} \quad (3)$$

where V_{O} is the total volume of the oxygen clumps, and u and l refer to the upper and lower levels. The effective recombination rates $\alpha_{\text{eff}}^{\text{ul}}$ (for the purpose of the analytical formulae here) are computed in the purely radiative limit (no collisional deexcitation), using Case B for the optical depths (escape probabilities

of zero for allowed transitions to the ground state, and of unity otherwise).

To get an idea how useful the measurements of the recombination line luminosities are, we use the model to analyze the amount of line blending and scattering that is present. The presence of blending and scattering still allows a determination of an upper limit to the recombination luminosity in the line of interest, which from Eq. 3 translates to an upper limit for $V_{\text{O}} n_e^2$.

In our models O I $\lambda 7771$ is relatively uncontaminated between 100-500 days. It is optically thick up to ~ 400 days. Pure recombination emission is thus present only after this time. O I $\lambda 9263$ is at all times strongly blended with [Co II] $\lambda 9338$ in particular, but also with S I $\lambda\lambda 9218, 9228, 9237$ and Mg II $\lambda\lambda 9218, 9244$. It becomes optically thin at ~ 200 days. Pure recombination emission is never present. The O I $1.130 \mu\text{m}$ line has little contamination in the model throughout the evolution. Na I $\lambda\lambda 1.138, 1.140 \mu\text{m}$ typically contributes $\sim 10\%$. The line becomes optically thin at ~ 200 days. Pure recombination emission is present between ~ 150 -500 days. The O I $1.316 \mu\text{m}$ line has little contamination in the model early on (Fig. A.4), but for $t \geq 200$ days becomes overtaken by [Fe II] $\lambda 1.321 \mu\text{m}$ + [Fe II] $1.328 \mu\text{m}$ (Fig. A.9). It becomes optically thin at ~ 200 days. Pure recombination emission is present between ~ 150 -200 days.

We use these considerations to derive either direct estimates (when pure recombination is indicated) or upper limits (when blending and/or scattering is indicated) of the quantity $n_e f_{\text{O}}^{1/2}$ (where f_{O} is the filling factor of the oxygen clumps, $4\pi/3 (V_{\text{core}} t)^3 f_{\text{O}} = V_{\text{O}}$), presented in Table 5. All four O I recombination lines indicate a value for $n_e f_{\text{O}}^{1/2} \sim 3 \times 10^8 \text{ cm}^{-3}$ at 100 days, and $n_e f_{\text{O}}^{1/2} = (3 - 7) \times 10^7 \text{ cm}^{-3}$ at 200 days.

From Figs. 1 and 2, it is clear that the 12C model underproduces the oxygen recombination lines. Closer inspection of the ionization balance at 200 days shows that the O II ions in the O/Si/S zone are completely neutralized by charge transfer with Si I and S I, and in the O/C zone by C I. The ion pools in these zones instead consist of Mg II, Si II, and S II (O/Si/S zone) and C II and Mg II (O/C zone). If these charge transfer reactions are overestimated, the recombination lines from O I become underestimated.

If charge transfer rates were zero, the quantity $n_e f_{\text{O}}^{1/2}$ would not have any strong dependence on density - **doubling the vol-**

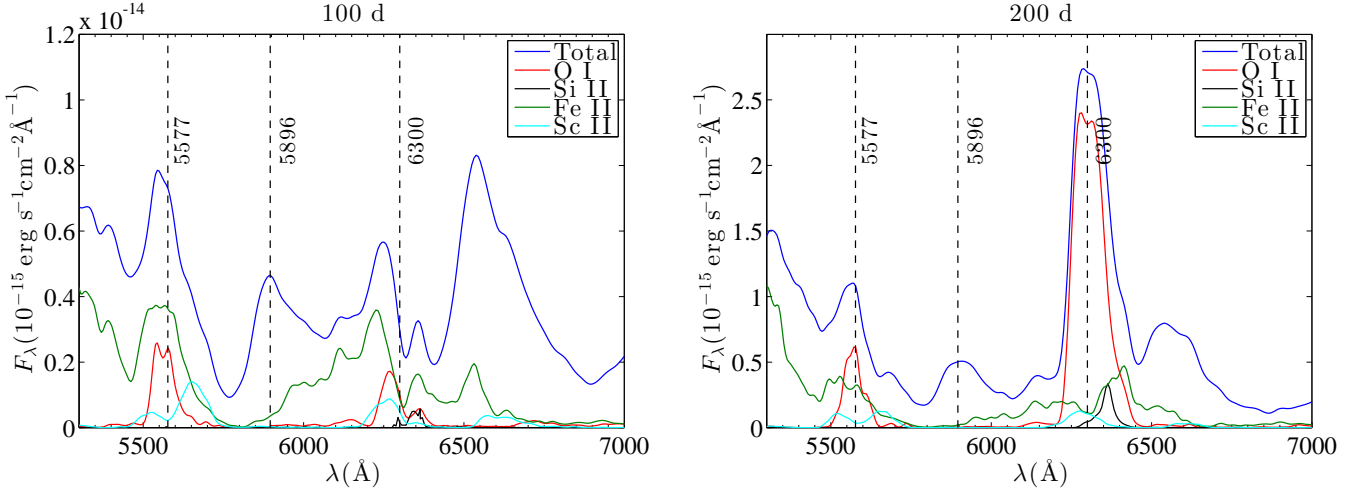


Fig. 12. Model spectra (model 13A) at 100 days (left) and 200 days (right), showing total flux (blue) and the contributions by O I (red), Si II (black), Fe II (green) and Sc II (cyan). Distinct blueshifts of [O I] λ 5577 and [O I] λ 6300, 6364 occur in the model at 100 days, due to a combination of radiative transfer effects (line blocking) and line blending. At 200 days these effects are less severe and the model gives more symmetric line profiles. The spectra have been Gaussian smoothed ($R=250$).

ume leads to a halving of ionization rates per unit volume, which under the steady-state constraint must lead to a halving of the recombination rates per unit volume as well. If $n_e n_+ \approx n_e^2$, this means a factor $\sqrt{2}$ reduction in n_e , and $n_e f_O^{1/2}$ stays constant. This is confirmed by comparing models 13C and 13E with respect to the oxygen recombination lines - their luminosities are almost identical despite a factor 5 different densities (Fig. 13). The low density model has (for the O/Ne/Mg zone) $f = 0.13$ and $n_e = 6 \times 10^7 \text{ cm}^{-3}$ so $n_e f_O^{1/2} = 2.2 \times 10^7$. The high density model has $f = 0.026$, $n_e = 1.5 \times 10^8$, so $n_e f_O^{1/2} = 2.4 \times 10^7$.

However, as the O II fraction becomes low, there are enough neutral elements in the O/Si/S and O/C zones to neutralize O II by charge transfer. O I recombination lines are then quenched. Looking again at models 13C and 13E (in the O/Ne/Mg zone), the O II densities go from $n_{OII} = 4.7 \times 10^7 \text{ cm}^{-3}$ in the low-density model to $n_{OII} = 7.3 \times 10^7 \text{ cm}^{-3}$ in the high density model. Whereas n_e went up by a factor 2.5 ($\approx \sqrt{5}$), n_{OII} went up only by a factor 1.6, as the charge transfer neutralization of O II is more efficient in the high-density case. The result is that the O I recombination lines are weaker at high density, below some critical threshold.

The critical charge transfer reactions in the early phase are O II + Si I, O II + S I, O II + C I, and O II + Mg I, as all other species in the oxygen zones are too rare to affect the pool of oxygen ions. No published calculations for these rates exist. We use fast reactions rates of $10^{-9} \text{ cm}^3 \text{ s}^{-1}$ for the first three, and a small reaction rate for the last - these are based only on the presence or absence of transitions with typical resonance values (Rutherford et al. 1971; Pequignot & Aldrovandi 1986). **The uncertain rates above affect the oxygen ionization balance mainly in the O/Si/S and O/C zones, which are rich in Si, S and C, respectively. Little Mg I exists in the O/Ne/Mg zone since it is heavily photoionized.** Since the O/Si/S and O/C zones contain about 2/3 of the oxygen mass in low M_{ZAMS} models, there is thus a factor ~ 3 uncertainty in the O I recombination line luminosities introduced by the uncertainty in these rates. This is roughly the underproduction of the O I recombination lines in $12 M_\odot$ models, and we therefore do not consider this discrepancy to be critical. In the ejecta from a $13 M_\odot$ pro-

genitor the oxygen mass is almost twice as high, and the oxygen recombination lines are not off by more than a factor 2 (Fig. 13).

Fig. A.4 shows the full contribution by O I to the spectrum. The emission by O II is negligible at all epochs, including any contribution by [O II] λ 7320 to the [Ca II] doublet.

In summary, the thermal oxygen lines ([O I] λ 5577 and [O I] λ 6300, 6364) can be reproduced only with small/moderate amounts of oxygen in the ejecta, for the three SNe analyzed here $0.1 < M_O < 1 M_\odot$. The oxygen recombination lines (O I λ 7771, O I λ 9263, O I λ 11300 and O I λ 13100) are, within the uncertainties introduced by unknown charge transfer rates, consistent with both these oxygen masses but also with a factor ~ 3 larger values.

4.1.6. Sodium lines

Sodium has only one detectable line throughout the optical/NIR region; the Na I D doublet (Fig. A.5). As discussed in J12, even small amounts of Na I can produce optically thick D-lines throughout a SN nebula for a long time, giving a strong P-Cygni component. Any He I λ 5876 emission would scatter in these optically thick D-lines.

On top of the P-Cygni component is a recombination component from the O/Ne/Mg zone, where most of the synthesized sodium resides. This emission component is always weaker than the P-Cygni emission component by a factor of a few in the models. This makes difficult any direct determination of the sodium nucleosynthesis to an accuracy better than a few $\times 10^{-3} M_\odot$. A signature from high-mass progenitors should be a distinct emission component on top of the P-Cygni component.

4.1.7. Magnesium lines

The solar Mg abundance is $\log N = 7.60 \pm 0.04$ (Asplund et al. 2009), making the solar Mg/O ratio (by number) $n(\text{Mg})/n(\text{O}) = 0.081 \pm 0.012$, or equivalently $\text{Mg}/\text{O} = 0.12 \pm 0.018$ by mass. The KEPLER models produce a factor two lower ratio ($\text{Mg}/\text{O} = 0.05 - 0.07$, see Table 2). As galactic nucleosynthesis of oxygen and magnesium should be dominated by massive stars (Timmes

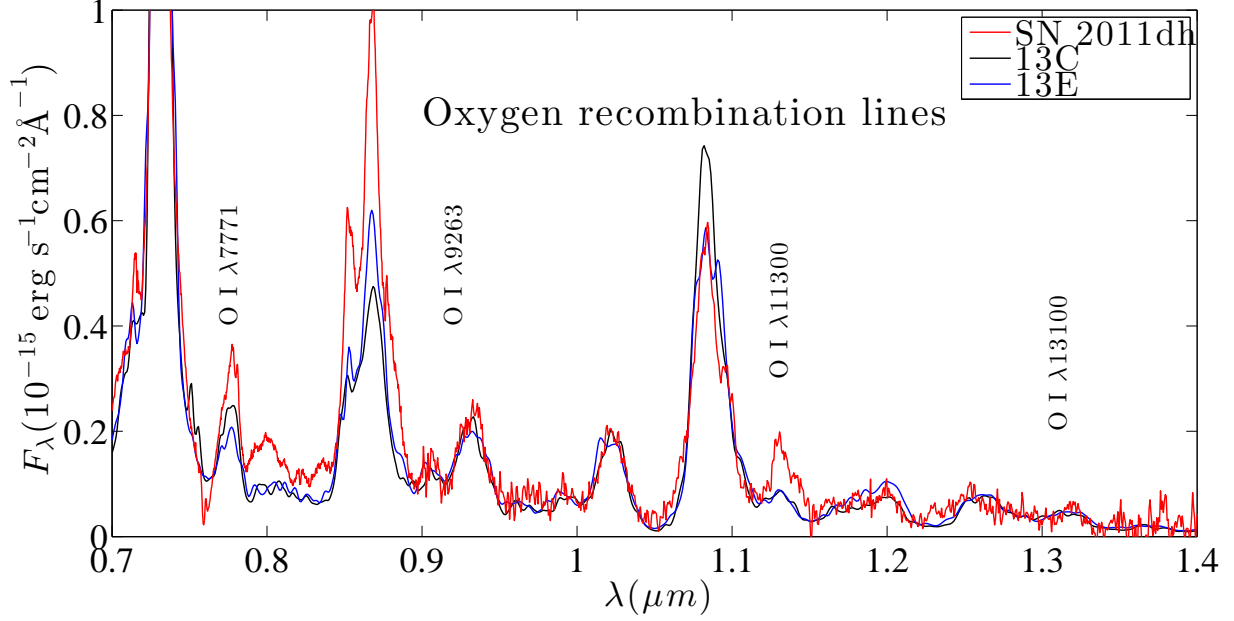


Fig. 13. Models with low (13C, black) and high (13E, blue) density in the oxygen region show similar O I recombination line luminosities, here at 200 days. Observed spectrum of SN 2011dh (optical part : 201 days, NIR part 198 days) in red.

Table 5. Measured luminosities of the O I recombination lines of SN 2011dh at 99 and 201 days, and the corresponding $n_e f_O^{1/2}$ factors derived from Eq. 3. We have used effective recombination coefficients $\alpha_{eff}^{7771} = 1 \times 10^{-13} \text{ cm}^3 \text{ s}^{-1}$, $\alpha_{eff}^{9263} = 4 \times 10^{-14} \text{ cm}^3 \text{ s}^{-1}$, $\alpha_{eff}^{1.130} = 3 \times 10^{-14} \text{ cm}^3 \text{ s}^{-1}$, $\alpha_{eff}^{1.316} = 4 \times 10^{-15} \text{ cm}^3 \text{ s}^{-1}$. Where the model calculations suggest line blending or scattering contributions, we add a \lesssim symbol.

Time (days)	$L_{7771}(n_e^{7771} f_O^{1/2})$ ($\text{erg s}^{-1}(\text{cm}^{-3})$)	$L_{9263}(n_e^{9263} f_O^{1/2})$ ($\text{erg s}^{-1}(\text{cm}^{-3})$)	$L_{1.130}(n_e^{1.130} f_O^{1/2})$ ($\text{erg s}^{-1}(\text{cm}^{-3})$)	$L_{1.316}(n_e^{1.316} f_O^{1/2})$ ($\text{erg s}^{-1}(\text{cm}^{-3})$)
99	$2.0 \times 10^{39} (\lesssim 2.6 \times 10^8)$	$1.1 \times 10^{39} (\lesssim 3.4 \times 10^8)$
198	$1.0 \times 10^{38} (4.6 \times 10^7)$	$3.0 \times 10^{37} (7.4 \times 10^7)$
201	$2.0 \times 10^{38} (\lesssim 2.9 \times 10^7)$	$1.1 \times 10^{38} (\lesssim 3.7 \times 10^7)$

et al. 1995), this difference will persist in galactic chemical evolution models.

From this perspective it is interesting to see what constraints SNe with distinct oxygen and magnesium emission lines, **as the ones studied here**, can provide on the relative Mg/O production. We begin by considering the line formation of Mg I] $\lambda 4571$. The relative contributions of collisional excitation and recombination for populating $3p^3P$ (the parent state of Mg I] $\lambda 4571$) is (**letting u and l denote the upper and lower states ($3s^2(^1S)$ and $3p(^3P)$ respectively), and approximating $n_{3s^2(^1S)} = n_{MgI}$**

$$\frac{R_{\text{coll}}}{R_{\text{rec}}} = \frac{n_{MgI} n_e 8.629 \times 10^{-6} T^{-1/2} \Upsilon_{ul}(T) g_l^{-1} e^{-(E_u - E_l)/kT}}{\alpha_{\text{eff}}^{3p(^3P)}(T) n_{MgII} n_e} \quad (4)$$

$$= 1.4 \left(\frac{x_{MgI}}{10^{-3}} \right) \exp \left[\frac{-(E_u - E_l)}{k} \left(\frac{1}{T} - \frac{1}{5000} \right) \right] \quad (5)$$

where $E_u - E_l = 2.71 \text{ eV}$, $x_{MgI} = n_{MgI}/n_{MgII}$, and we have used a collision strength of $\Upsilon_{ul}(T) = 1.95 (T/5000 \text{ K})^{-1/2}$, and an effective recombination rate $\alpha_{\text{eff}}^{3p(^3P)} = 3 \times 10^{-13} (T/5000 \text{ K})^{-1/2} \text{ cm}^3 \text{ s}^{-1}$. In the models, photoionization (which typically has an ionization rate $\sim 10^3$ times the non-thermal ionization rate) leaves almost all magnesium in the Mg II state throughout the nebular phase, so $x_{MgI} \ll 1$ at all times, with $x_{MgI} \approx 10^{-3}$ being a typical value. The ratio above then has values $R_{\text{coll}}/R_{\text{rec}} = 1.4, 0.3,$

and 0.02 for temperatures of $T = 5000, 4000,$ and 3000 K . As the neutral fraction tends to increase with time, the actual ratio will have a slower time-dependence than this, but the exponential term in Eq. 5 always ensures that recombination eventually dominates.

The proximity to unity for this ratio nevertheless means that the Mg I] $\lambda 4571$ emission is sensitive to the exact ionization balance of magnesium. Fig. 14 shows the regimes in $[x_{MgI}, T]$ space where collisional excitation and recombination dominate, respectively. The evolution of models 13C and 13E are also plotted, showing that physical conditions are close to the transition between the regimes, and in general both processes could be important.

All other Mg I lines come from high lying states that are more difficult to populate by collisional excitation, and will form mainly through recombinations. Some empirical verification for this can be found by considering the relative line luminosities of Mg I $1.183 \mu\text{m}$ and Mg I $1.504 \mu\text{m}$. The $1.183 \mu\text{m}$ line arises from a lower level than the Mg I $1.504 \mu\text{m}$ line, and has a larger collision strength relative to the ground state; consequently collisional excitation should lead to higher luminosity than in $1.504 \mu\text{m}$ (both lines are allowed transitions to excited states and are thus radiatively deexcited). But the observed feature at $1.183 \mu\text{m}$ in SN 2011dh is significantly weaker than the $1.504 \mu\text{m}$ feature at both 99 and 201 days, which cannot be achieved in the colli-

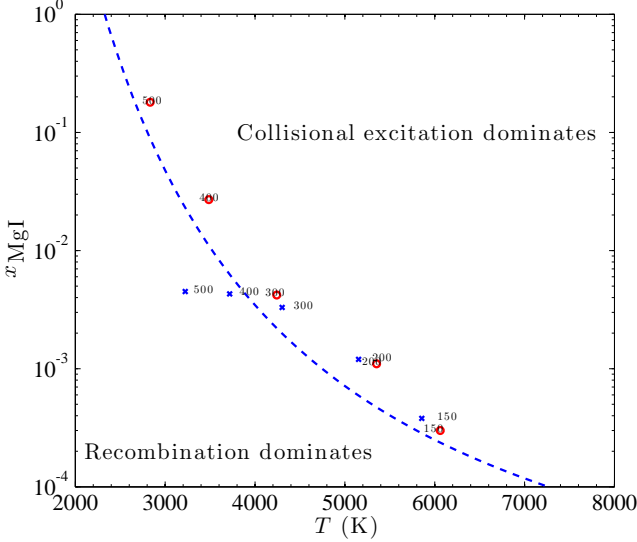


Fig. 14. The regimes of Mg I] $\lambda 4571$ line formation in the $[T, x_{MgI}]$ plane. The values as function of time for models 13C (blue crosses) and 13E (red circles) are also shown. It is clear that both recombination and collisional excitation may contribute to the Mg I] $\lambda 4571$ luminosity.

s

sional excitation scenario. The dominance of Mg I] $\lambda 4571$ and Mg I $\lambda 1.504 \mu\text{m}$ in the spectrum of Mg I is instead naturally explained in a recombination scenario, since these lines arise from triplet states which generally take most of the recombinations, whereas Mg I $\lambda 1.183 \mu\text{m}$ (as well as Mg I $\lambda 5200$ and Mg I $\lambda 8806$) arise from singlet states. The situation is analogous to the triplet to singlet recombination line ratios in He I, **where $\sim 3/4$ of all recombinations go to the triplet ladder and $\sim 1/4$ to the singlet ladder (e.g. Benjamin et al. 1999).**

Having established that the nebular Mg I lines likely arise by recombination, with collisional excitation making some (uncertain) contribution to Mg I] $\lambda 4571$, we can attempt an understanding of their luminosities. The critical density (**over which collisional deexcitations have importance**) for Mg I] $\lambda 4571$ (at 5000 K) is $n_{e,\text{crit}}^{4571} = 8 \times 10^9 \beta_{4571} \text{ cm}^{-3}$, **where β_{4571} is the escape probability.** We find in our models that the optical depth of the line is of order unity in the nebular phase, so $\beta_{4571} \gtrsim 0.1$ and $n_{e,\text{crit}}^{4571} \gtrsim 10^9 \text{ cm}^{-3}$. This is at least an order of magnitude higher than the electron density in the oxygen zones in our models, so collisional deexcitation is unimportant and most populations of $3p(^3P)$ will lead to emission of a 4571 \AA photon. We can therefore write (using the result that $n_{MgII} \approx n_{Mg}$ in all models)

$$L_{4571} = 6.5 \times 10^{39} \left(\frac{M_{Mg}}{1 M_{\odot}} \right) \left(\frac{n_e}{10^8 \text{ cm}^{-3}} \right) \times \left(\frac{\alpha_{eff}^{3p(^3P)}}{3 \times 10^{-13} \text{ cm}^3 \text{ s}^{-1}} \right) e^{-\tau_{lb}^{4571}(t)} \text{ erg s}^{-1} \quad (6)$$

where $\tau_{lb}^{4571}(t)$ is the optical depth due to line blocking (by other lines). For a given magnesium mass M_{Mg} , higher electron density thus gives higher Mg I] $\lambda 4571$ emissivity (up to the limit when the critical density is reached or when $x_{MgII} \gg x_{MgI}$ is no longer fulfilled). However, the model calculations show that the line blocking optical depth τ_{lb}^{4571} at 4571 \AA can be significant far into the nebular phase (see below), and increases for higher density. This effect may thus limit the growth of L_{4571} with density.

Table 6. Measured luminosities in Mg I] $\lambda 4571$ and Mg I $\lambda 1.504 \mu\text{m}$ in SN 2011dh, and the corresponding electron density factors from Eq. 6. We use effective recombination coefficients $\alpha_{4571} = 3 \times 10^{-13} \text{ cm}^3 \text{ s}^{-1}$ and $\alpha_{1.5 \mu\text{m}} = 5 \times 10^{-14} \text{ cm}^3 \text{ s}^{-1}$. **Since collisional excitation may contribute to the Mg I] $\lambda 4571$ luminosity, we add a \lesssim symbol to the derived electron density.**

Time (days)	$L_{4571} (n_e \left(\frac{M_{Mg}}{M_{\odot}} \right) e^{-\tau_{lb}^{4571}})$ ($\text{erg s}^{-1} (\text{cm}^{-3})$)	$L_{1.504 \mu\text{m}} (n_e \left(\frac{M_{Mg}}{M_{\odot}} \right))$ ($\text{erg s}^{-1} (\text{cm}^{-3})$)
201	$2.8 \times 10^{38} (\lesssim 4.3 \times 10^6)$...
206	...	$9.7 \times 10^{37} (2.9 \times 10^7)$

The other distinct Mg I line observed in the optical/NIR is Mg I $\lambda 1.504 \mu\text{m}$. Having a much higher critical density than Mg I] $\lambda 4571$ and suffering no significant line blocking, its luminosity should be well approximated by

$$L_{1.504 \mu\text{m}} = 3.2 \times 10^{38} \left(\frac{M_{Mg}}{1 M_{\odot}} \right) \left(\frac{n_e}{10^8 \text{ cm}^{-3}} \right) \times \left(\frac{\alpha_{eff}^{4p(^3P)}}{5 \times 10^{-14} \text{ cm}^3 \text{ s}^{-1}} \right) \text{ erg s}^{-1}. \quad (7)$$

Table 6 shows the measured luminosities in Mg I] $\lambda 4571$ and Mg I $\lambda 1.504 \mu\text{m}$ in SN 2011dh, and the corresponding quantity $n_e M_{Mg}$. With the recombination rate data that we use (see Sect. B.2) the effective recombination rates for $3p(^3P)$ and $4p(^3P)$ are $\alpha_{eff}^{3p(^3P)} \sim 0.5 \alpha_{tot}$ and $\alpha_{eff}^{4p(^3P)} \sim 0.08 \alpha_{tot}$, respectively, which at 5000 K translate to 3×10^{-13} and $5 \times 10^{-14} \text{ cm}^3 \text{ s}^{-1}$.

In table 6 we see that at 200 days the Mg I $1.504 \mu\text{m}$ line gives an order of magnitude higher $n_e M_{Mg}$ value than the Mg I] $\lambda 4571$ line does, if the line blocking opacity would be zero ($e^{-\tau_{lb}^{4571}} = 1$). One contributing factor is likely that $\tau_{lb}^{4571} > 0$ at this epoch, as the blueshift of the Mg I] $\lambda 4571$ line suggests (1300 km s^{-1} , see Fig. 15). **The Mg I $1.504 \mu\text{m}$ line shows no blueshift, as there is little line opacity in the NIR.** If $\tau_{lb}^{4571} = 2$, the derived $n_e M_{Mg}$ values agree. The expected blueshift for a uniform sphere with a smooth radial opacity τ is $\Delta V/V = -1 + \ln(1 + \tau)/\tau$ (Lucy et al. 1991), which has a value $\Delta V/V = -0.45$ for $\tau = 2$ (**note that the use of formulae for continuous opacities is only strictly applicable if the line opacity is made up by a large number of equally spaced and equally strong lines, so its use here is only for qualitative purposes**). This matches the observed blueshift of Mg I] $\lambda 4571$ ($\Delta V \sim 1300 \text{ km s}^{-1}$) if $V_{exp} \sim 3000 \text{ km s}^{-1}$, in good agreement with the observed line widths.

The blueshift of Mg I] $\lambda 4571$ gradually disappears with time (Fig. 15, Table 7), reaching $\Delta V < 400 \text{ km s}^{-1}$ at 400 days, as expected in the line blocking scenario. The shift at 400 days requires $\tau_{lb}^{4571} \lesssim 0.3$, and so the $n_e M_{Mg}$ values derived from the Mg I] $\lambda 4571$ line listed in Table 6 at these epochs should be close to the true ones. Fig. 16 shows how the Mg I] $\lambda 4571$ line profile evolves in model 13A between 200 days (where there is significant line blocking) and 300 days (where most line blocking is gone). The total line profile is, as for the O I lines, affected in a complex way by both line blocking from the receding side and from blending with other emission lines.

The optical to NIR spectral coverage at 200 days allows us to combine the constraints from the oxygen and magnesium recombination lines. From the oxygen lines (Sect. 4.1.5) we have $n_e f_O^{1/2} = (3 - 7) \times 10^7 \text{ cm}^{-3}$, and from the magnesium lines we have $n_e (M_{Mg}/M_{\odot}) \approx 2 \times 10^7 \text{ cm}^{-3}$. Combining these we obtain a constraint $M_{Mg} = (0.3 - 0.6) f_O^{1/2} M_{\odot}$. This range is plotted

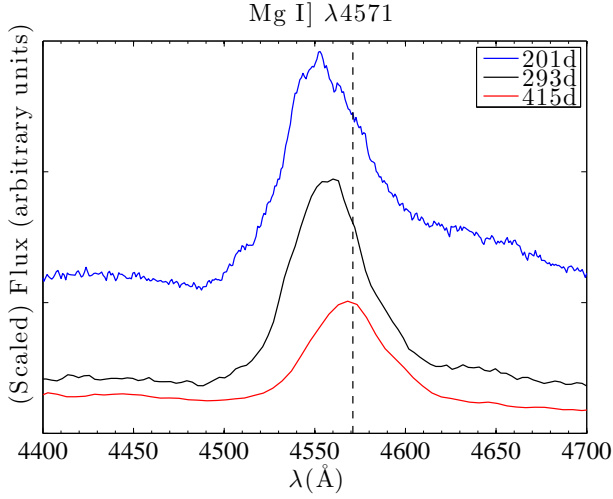


Fig. 15. The observed Mg I $\lambda 4571$ feature in SN 2011dh. The line peak shows a blueshift of 1300 km s^{-1} at 200 days, which gradually disappears and is smaller than 400 km s^{-1} at 415 days.

in Fig. 18. For a filling factor $f_o = 10^{-2}$, a magnesium mass of $0.03 - 0.06 M_\odot$ is thus needed to reproduce the observed Mg I recombination lines, whereas for $f_o = 0.1$ a mass $0.1 - 0.2 M_\odot$ is needed. A formal limit can be stated if we take the $f_o \gtrsim 10^{-2}$ constraint from the [O I] $\lambda\lambda 6300, 6364$ lines and $f_o < 0.5$, giving $0.03 M_\odot < M_{Mg} < 0.3 M_\odot$. If we take the oxygen mass to have been constrained to $0.2 - 0.5 M_\odot$ (from the acceptable fits of the [O I] $\lambda\lambda 6300, 6364$ lines, Fig. 23), the Mg/O ratio falls in the $0.06 - 1.5$ range, or $\text{Mg/O} = (0.5 - 12) [\text{Mg/O}]$. Thus, the Mg and O production in SN 2011dh is consistent with the solar value, but with relatively large error bars. Bringing the ratio within a factor two of the solar value requires the oxygen/magnesium zones to be clumpy, with $f_o \sim 10^{-2}$. The $\sim 1/2$ [Mg/O] production in the KEPLER models is difficult to reconcile with SN 2011dh, lying at the very edge of the tolerance interval.

Fig. 17 shows the observed and model luminosities in Mg I $\lambda 4571$ and Mg I $1.504 \mu\text{m}$. With the caveat that a clear extraction of the line is difficult due to blending (more significant in some models than others, see e.g. Fig. 1), the general trend is a factor $\sim 2-4$ underproduction of Mg I $\lambda 4571$. From the analysis above, there are likely two contributing factors to this - the factor ~ 2 underproduction of magnesium in the KEPLER models relative to the solar value, and a too low density assumed for the O/Ne/Mg zone in the models. The strong impact of the density is illustrated by comparing the 13C (low density) and 13E (high density) tracks. The Mg I $1.504 \mu\text{m}$ line depends mostly on these parameters, whereas the Mg I 4571 line has additional sensitivity to the exact radiation field (through its influence in the neutral fraction) and on line blocking.

4.1.8. Silicon lines

Fig. A.7 shows the contribution by Si I to the model spectrum (higher ions produce negligible emission). The detectable lines are [Si I] $1.099 \mu\text{m}$, [Si I] $1.20 \mu\text{m}$, and [Si I] $1.607, 1.646 \mu\text{m}$. No detectable optical lines are predicted. The emission comes from the explosively synthesized silicon in the Si/S and the O/Si/S zones. **Comparison to data?**

4.1.9. Sulphur lines

Fig. A.8 shows the contribution by S I and S II to the model spectrum (higher ions produce negligible emission). The sulphur lines arise from explosively made sulphur in the Si/S zone. The only line predicted to be strong is [S I] $1.082 \mu\text{m}$, which is about as strong as He I $1.083 \mu\text{m}$. **Comparison to data?**

4.1.10. Calcium lines

Most of the calcium nucleosynthesis in SNe occurs in explosive oxygen burning, producing a Si/S zone that contains a few percent calcium by mass. The nucleosynthesis depends both on the progenitor structure and the properties of the explosion itself.

In hydrogen-rich SNe this calcium is not visible as it is overwhelmed by emission from primordial calcium in the massive hydrogen envelopes (Li & McCray 1993). Here, we find that in SN ejecta without such an envelope, the [Ca II] $\lambda\lambda 7291, 7323$ emission comes indeed from the newly synthesized calcium up to ~ 500 days. Calcium is not as prominent a cooler of the He envelope as the H envelope, as the radiation field here is harder, ionizing most of the calcium to Ca III in the nebular phase. After ~ 500 days, however, photoionization rates have dropped enough that Ca II starts forming in the He envelope, and eventually takes over from the calcium in the Si/S clumps in producing the [Ca II] $\lambda\lambda 7291, 7323$ emission.

Fig. 20 shows the observed and modelled [Ca II] $\lambda\lambda 7291, 7323$ lines. In model 12C, the fraction of the cooling of the Si/S/Ca zone done by Ca II is 100, 83, 67, and 42% at 100, 200, 300 and 400 days, respectively. As we are thus in a regime where the cooling is dominated by Ca II, the Ca II luminosity is not sensitive to the Ca II mass, but rather depends on the mass of the Si/S zone. The satisfactory agreement between observed and modelled Ca II lines thus supports the mass of the explosive oxygen burning ashes in the models used; $0.06 - 0.1 M_\odot$. These ashes contain about 40% each of silicon and sulphur.

We find that the Ca II $\lambda\lambda 8498, 8542, 8662$ lines in general do not originate from the calcium in the Si/S zone. They instead arise by fluorescence following absorption in the H&K lines by the Ca II that exists in the Fe/He clumps and the primordial Ca in the rest of the nebula. The radiative deexcitation rate is $A_{HK}^{eff} = 1.5 \times 10^8 \beta_{HK} \text{ s}^{-1}$ for the return transition in H&K, and $A_{IR}^{eff} = 1.1 \times 10^7 \beta_{IR} \text{ s}^{-1}$ for the IR channel. Whereas the H&K channel is optically thick ($\beta_{HK} < 1$) as long as absorption occurs, the IR channel is optically thin ($\beta_{IR} = 1$) in model 12C from ~ 100 days. The result is that $A_{IR}^{eff} \gtrsim A_{HK}^{eff}$, and a significant fraction of the H&K absorptions are followed by fluorescence in the IR lines. Reaching the 3D(2d) state, further radiative deexcitation in the [Ca II] $\lambda\lambda 7291, 7323$ lines competes with collisional deexcitation. Since $A_{7291,7323} = 1.3 \text{ s}^{-1}$ (the lines are optically thin in the nebular phase for this component), collisional deexcitation dominates if $C_{ul} > A_{ul} \rightarrow 8.629 \times 10^{-6} T^{-1/2} \gamma_{ul} g_u^{-1} n_e > A_{ul}$, which translates to $n_e > 10^7 \text{ cm}^{-3}$ (for $T = 3000 \text{ K}$ and $\Upsilon = 6$). This is close to the typical electron density in the phase investigated here (in model 12C, n_e equals $2 \times 10^8, 6 \times 10^6$ and $8 \times 10^5 \text{ cm}^{-3}$ in the Si/S zone at 100, 300, and 500 days) - we can thus expect some further fluorescence but also some thermalization (particularly early in the nebular phase).

In this scenario, the width of the Ca II IR emission lines should equal the width of the Ca II H&K absorption lines, and can serve as a proxy for measuring to which velocity Ca II absorbs in H&K.

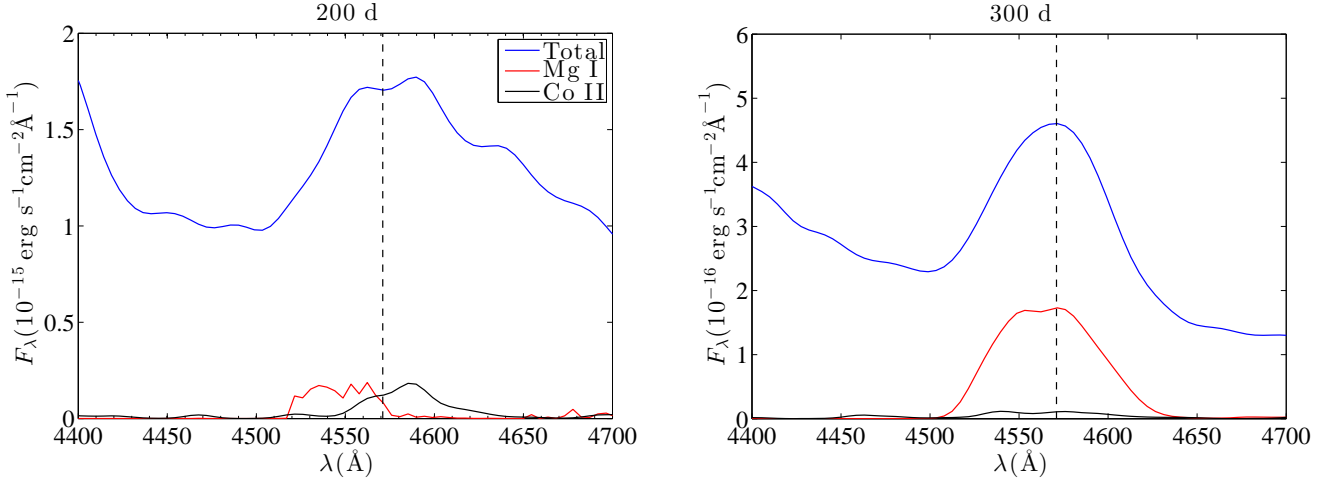


Fig. 16. Zoom-in on Mg I] $\lambda 4571$ in model 13A (blue) at 200 (left) and 300 (right) days. The total flux is in blue, the contribution by Mg I in red and by Co II in black. At 200 days there is significant line blocking of the red side of the Mg I emission, as well as a blend with some iron-group line emission. At 300 days both the line blocking and blending have abated. Gaussian $R = 250$ smoothing has been applied.

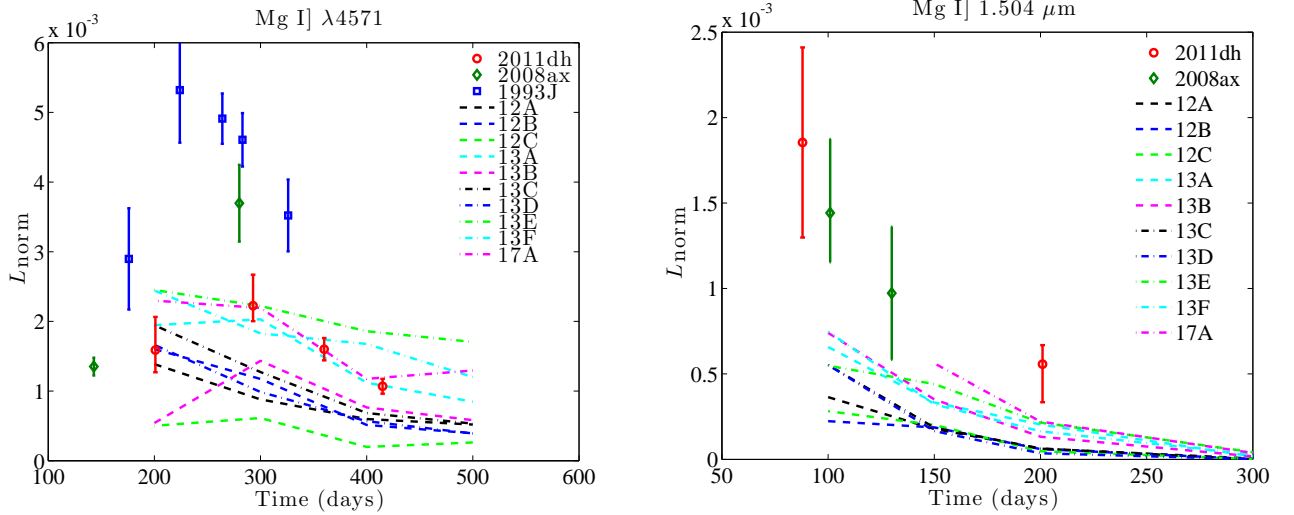


Fig. 17. The luminosity in Mg I] $\lambda 4571$ (left) and Mg I] $1.504 \mu\text{m}$ (right) relative to the ^{56}Co decay power in SN 1993J, SN 2008ax, and SN 2011dh, and in the models.

4.1.11. Iron lines

Fig. A.9 shows the contribution by Fe I and Fe II to the model spectrum (higher ions produce negligible emission). It is clear iron emission and scattering dominates the nebular spectrum of stripped-envelope SNe. The iron lines arise from both cooling and recombination of the iron from decayed ^{56}Co , but also from scattering in this component as well as from primordial iron in the rest of the nebula.

Distinct iron lines with potential use for simple diagnostics are [Fe II] $\lambda 7155$, [Fe II] $1.26 \mu\text{m}$, and [Fe II] $1.64 \mu\text{m}$. The [Fe II] $\lambda 7155$ line has an excitation temperature of 22800 K whereas the $1.26 \mu\text{m}$ line has an excitation temperature of 11500 K, their ratio is thus temperature-sensitive. Both lines are optically thin from 100 days in model 12C. The $i=10$ level (giving the $1.26 \mu\text{m}$ line) is in LTE for a few hundred days, but $i=17$ (giving the 7155 line) starts falling out already at 100 days. In the LTE and optically thin limit

$$\frac{L_{7155}}{L_{1.26}} \approx 60 \exp\left(-\frac{11300 \text{ K}}{T}\right). \quad (8)$$

The [Fe II] $\lambda 7155$ line is quite heavily blended with [Ca II] $\lambda 7291$, 7323 to the right and He I $\lambda 7065$ to the left, and its flux is therefore hard to determine. At 100 days it is not visible. At 200 days the [Fe II] $\lambda 7155$ luminosity is $L_{7155} = 3.9 \times 10^{37} \text{ erg s}^{-1}$. The [Fe II] $\lambda 1.26 \mu\text{m}$ line is noisy but we estimate $L_{1.26} = 6 \times 10^{37} \text{ erg s}^{-1}$, giving a ratio of 0.7, which gives an LTE temperature of 2500 K. This is much cooler than the computed temperatures in the Fe zone which is $\sim 4000 \text{ K}$ at 200 days. The deviation from LTE for level 17 is only a factor ~ 2 , which would still require $T < 3000 \text{ K}$. The [Fe II] $\lambda 7155$ / [Fe II] $\lambda 1.26 \mu\text{m}$ line ratio thus suggests that model 12C has too hot Fe clumps and/or too high densities in them. **However, temperature determination from the cobalt lines (Sect. 4.1.12), which are expected to form in the same clumps, are higher and in better agreement with the model. The reason for this discrepancy is unclear.**

The luminosity of [Fe II] $\lambda 1.64 \mu\text{m}$ at 200 days is $L_{1.64} = 7.6 \times 10^{37} \text{ erg s}^{-1} = 1.3 L_{1.26}$. As [Fe II] $1.64 \mu\text{m}$ and [Fe II] $\lambda 1.26 \mu\text{m}$ arise from the same upper level and have almost the same A-values, their ratio should be close to $L_{1.64}/L_{1.26} = 1.26/1.64 =$

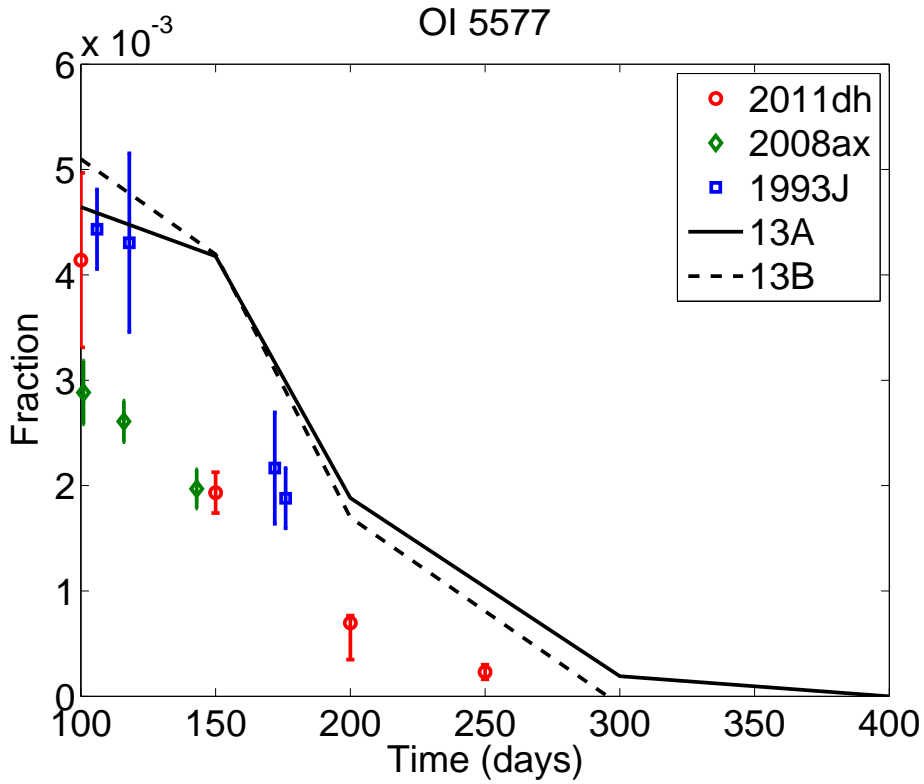


Fig. 18. The relationship between magnesium mass and oxygen/magnesium zone filling factor derived from the oxygen and magnesium recombination lines in SN 2011dh (solid line is best estimate and dashed lines show error bars). The Mg recombination lines can be reproduced by either high-mass progenitors ($M_{ZAMS} \sim 20$) and large filling factors, or low-mass progenitors ($M_{ZAMS} \sim 12$) and small filling factors. The Mg mass- f combinations of some models are shown as red crosses. The models we use have about half the solar Mg/O ratio.

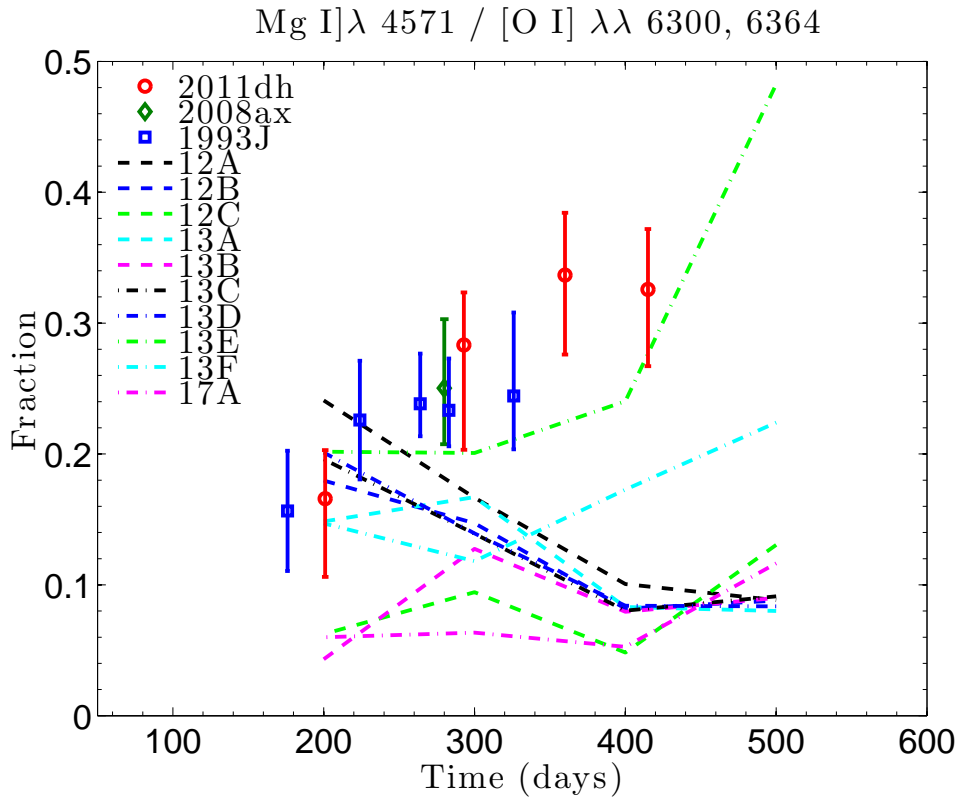


Fig. 19. The luminosity in Mg I] $\lambda 4571$ relative to [O I] $\lambda\lambda 6300, 6364$ in SN 2011dh, SN 2008ax, and SN 1993J.

Table 7. First wavelength moments (integration over $\pm 4500 \text{ km s}^{-1}$ with a linear continuum estimates as described in Sect. 4) of Mg I $\lambda 4571$, [O I] $\lambda 5577$ and [O I] $\lambda\lambda 6300, 6364$ as function of time in SN 2011dh, SN 2008ax and SN 1993J. For Mg I $\lambda 4571$ we measure only at $t > 200$ days, before which the line is weak and/or heavily blended. The velocity shift for [O I] $\lambda\lambda 6300, 6364$ is computed by assuming a 3:1 ratio which gives a rest wavelength first moment of 6316 Å. Notice how the blueshifts gradually disappear with time for all three lines in SN 2011dh, but persist in SN 2008ax and SN 1993J.

Time (days)	Mg I $\lambda 4571$ (Å (km s ⁻¹))	[O I] $\lambda 5577$ (Å (km s ⁻¹))	[O I] $\lambda\lambda 6300, 6364$ (Å (km s ⁻¹))
SN 2011dh			
151	...	5557 (-1070)	6306 (-480)
201	4560 (-730)	5558 (-1000)	6309 (-320)
293	4560 (-740)	...	6307 (-410)
415	4569 (-120)	...	6317 (+70)
SN 2008ax			
143	...	5548 (-1600)	6308 (-400)
151	...	5546 (-1680)	6301 (-710)
266	6306 (-500)
280	4563 (-500)	...	6307 (-400)
328	4557 (-950)	...	6297 (-420)
359	6308 (-400)
415	4560 (-740)	...	6294 (-1000)
439	4561 (-670)	...	6300 (-770)
SN 1993J			
176	...	5556 (-1150)	6298 (-840)
224	4559 (-780)	5559 (-980)	6309 (-310)
236	...	5539 (-2050)	6310 (-280)
256	4564 (-440)	...	6312 (-200)
264	4560 (-690)	...	6309 (-320)
283	4562 (-610)	...	6308 (-400)
299	4559 (-780)	...	6305 (-540)
326	4561 (-630)	...	6310 (-290)
368	4558 (-880)
415	4561 (-670)
437	4561 (-580)
463	4562 (-600)
524	4562 (-580)

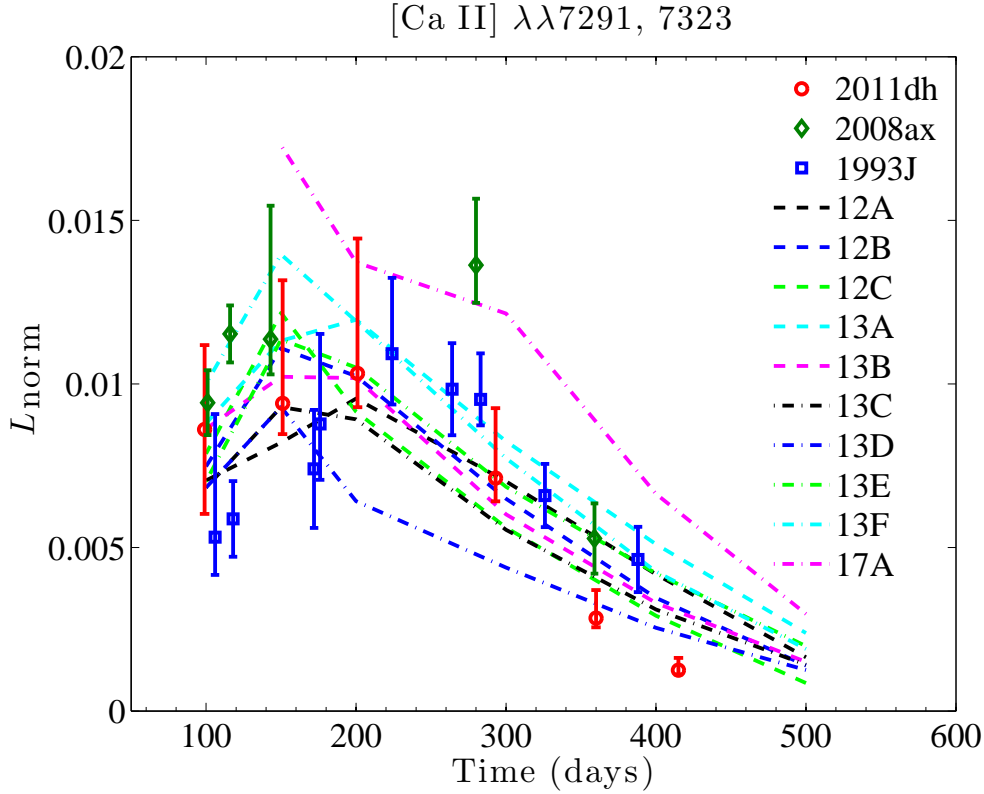


Fig. 20. The luminosity in [Ca II] $\lambda\lambda 7291, 7323$ relative to the ^{56}Co decay power in SN 1993J, SN 2008ax, SN 2011dh, and in the models.

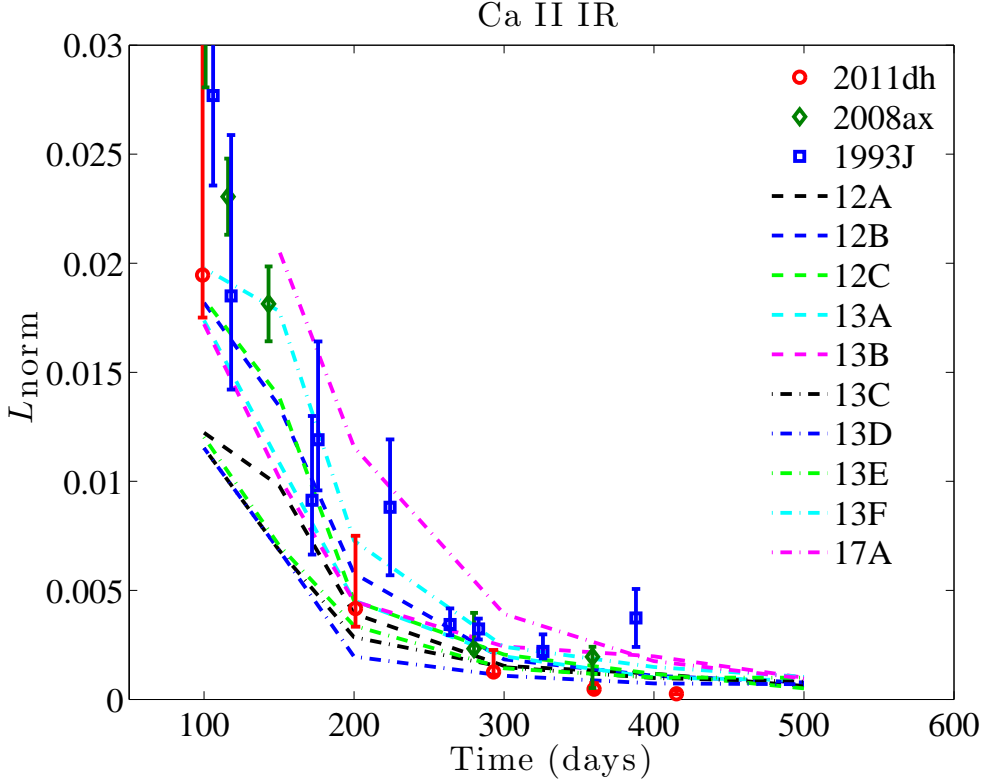


Fig. 21. The luminosity in Ca II IR lines in the models, compared to SN 2011dh, SN 2008ax and SN 1993J.

0.8. Given the uncertainties in the line flux measurements, this is consistent with the measured value. The 12C model does not give any strong contribution by [Si I] 1.64 μm to the [Fe II] 1.64 μm line at 200 days, **but at later times it starts to dominate the blend.**

4.1.12. Cobalt lines

Fig. A.10 shows the contribution by Co II to the spectrum (other ions are negligible). The models predict strong [Co II] $\lambda\lambda 9338, 9344$, [Co II] $\lambda 9946$, [Co II] $\lambda\lambda 1.019, 1.025, 1.028 \mu\text{m}$, and [Co II] $\lambda 1.547 \mu\text{m}$ at early times, arising from the radioactive ^{56}Co . At later times most of the ^{56}Co has decayed and the lines become weak.

All lines mentioned above are clearly detected in the early spectra of SN 2011dh. The [Co II] $\lambda\lambda 1.019, 1.025, 1.028 \mu\text{m}$ line profile extends to 3700 km s^{-1} blue-ward of 1.019 μm , and 3000 km s^{-1} redward of 1.028 μm , although the red side is possibly cut off by the He I 1.083 μm absorption trough. These velocities indicate the velocity scale to which the ^{56}Ni is mixed. However, [Co II] 1.547 μm extends to only $\pm 2200 \text{ km s}^{-1}$. The [Co II] $\lambda\lambda 9338, 9344$ doublet is blended with [O I] $\lambda 9263$ on the blue side. The red side extends to 4700 km s^{-1} redward of 9344 \AA . The model does not predict any line blending on the red side, and this could then possibly signal ^{56}Co at these high velocities.

No simple way to determine the ^{56}Co mass from the optical/NIR cobalt lines exists. A more useful approach is probably the reverse, to take the ^{56}Co mass as given and derive the zone temperature. The observed [Co II] $\lambda\lambda 1.019, 1.025, 1.028 \mu\text{m}$ luminosity at 100 days is $L_{1.02} = 7 \times 10^{38} \text{ erg s}^{-1}$. Using the LTE and optically thin formula

$$L_i = \frac{M_{\text{CoII}}}{56m_p} Z(T) g_u e^{-\Delta E_u/kT} A_i h\nu_i, \quad (9)$$

where $Z(T)$ is the partition function, the corresponding temperature is $T_{\text{LTE}} = 4400 \text{ K}$. This is somewhat cooler than in our model 12C ($T = 5500 \text{ K}$). The same exercise for the [Co II] $\lambda\lambda 9338, 9344$ lines gives an observed luminosity $L_{9338,9344} = 2.4 \times 10^{39} \text{ erg s}^{-1}$ and $T_{\text{LTE}} = 5500 \text{ K}$, in close agreement with the model temperature. Thus, given an **initial** ^{56}Co mass of 0.075 M_{\odot} these lines constrain the cobalt temperature to $T \sim 5000 \text{ K}$ at 100 days.

4.1.13. Nickel lines

Fig. A.11 shows the contribution by Ni II to the spectrum (emission from other nickel ions is negligible). The radioactive nickel quickly decays and is not present in enough quantities to be visible in the nebular phase. However, some stable ^{58}Ni is created alongside the ^{56}Ni , which gives rise to [Ni II] $\lambda\lambda 7377, 7411$ emission. These lines will in general blend with the red wing of the forbidden Ca II lines. Diagnosis of the ^{58}Ni yield (which in turn constrains the explosion dynamics) may be possible in narrow-lined SNe.

Fig. A.11 shows that identification of ^{58}Ni may also be done by [Ni II] 1.939 μm , which arises from the same upper level as [Ni II] $\lambda\lambda 7377, 7411$. The day 201 spectrum of SN 2011dh shows an emission line at this wavelength, but at low S/N.

4.1.14. Other lines

Fig. A.12 shows the contribution to the spectrum by all other lines (blue), and the Ti II component of these in green. Titanium is an effective line blocking agent, and provides much of the quasi-continuum **through scattering and fluorescence**. Subtracting this component, it is clear that we have accounted for most of the the optical/NIR flux.

4.2. Influence of model parameters

4.2.1. Progenitor mass

The model combinations that differ only in the progenitor mass are 12C, 13F, and 17A⁶. Fig. 22 shows the optical/NIR spectra of these models at 300 days. As illustrated here and in Fig. 23, one of the key differences between these models is the [O I] $\lambda\lambda 6300, 6364$ lines - they are about a factor four stronger in the ejecta from a 17 M_{\odot} progenitor compared to a 12 M_{\odot} progenitor. For the values of the other parameters used here (strong mixing, local positron absorption, no molecular cooling, dust formation from 200 days, and high oxygen zone density) SN 1993J, SN 2008ax and SN 2011dh are matched by models of ejecta from $M_{ZAMS} \approx 15 M_{\odot}$ (**judged by the bracketing of the 13 and 17 M_{\odot} models**), 13 M_{\odot} , and 12 M_{\odot} progenitors, respectively.

The [O I] $\lambda 5577$ line has a similar dependency with the progenitor mass (Fig. 10), and the [O I] $\lambda 5577$ /[O I] $\lambda\lambda 6300, 6364$ ratio is little affected. This can be understood from the fact that we are in the regime $\tau_{\gamma} < 1$, and the energy deposition per unit mass (which governs the temperature) is roughly independent of the ejecta mass. Indeed, we find in the 12, 13 and 17 M_{\odot} models an O/Ne/Mg zone temperature at 300 days all around 4000 K, with a variation less than 100 K.

The magnesium recombination lines also become stronger for higher progenitor masses (Fig. 22). Fig. 17 is here somewhat misleading as the actual Mg I] $\lambda 4571$ line luminosity differs by almost a factor two between models 13F and 17A, but the algorithm used to extract the line luminosity gives a similar value as there is a strong blend on the red side of the line in the 17A model that affects the continuum determination. As the oxygen zone density is held at constant value in the three models, the neutral fraction of magnesium is about the same in all models, and the relative contributions by collisional excitation and recombination are therefore similar (see Sect. 4.1.7). The Mg I 1.504 μm line is weak at 300 days and difficult to discern, but also gets stronger for higher mass progenitors.

The [Ca II] $\lambda 7291, 7323$ lines also increase with progenitor mass, although quite weakly (Fig. 20). As the [Ca II] lines dominate the cooling of the oxygen burning ashes (the Si/S zone), their luminosities are mainly dependent on the mass of the Si/S zone. This zone mass varies only from 0.06 to 0.10 M_{\odot} in mass over the 12 – 17 M_{\odot} range. The relatively weak dependency with progenitor mass predicted by the models is in rough agreement with the quite small differences seen in the observed sample.

The Ca II triplet does not arise from the synthesized calcium (Sect. 4.1.10), and in these models [C I] $\lambda 8727$ cooling of the O/C zone overwhelms the Ca II triplet at 300 days. This situation depends, however, sensitively on the amount of CO cooling of the O/C clumps (see Sect. 4.2.4).

As discussed in Sect. 4.1.6, the Na I D lines have contributions from both a scattering component and a recombination component from the synthesized sodium. Fig. 22 shows that a distinct recombination component is produced in the 17 M_{\odot} ejecta, clearly distinguishable from the scattering-dominated component seen at lower masses.

⁶ Some caution about language is needed here; it is strictly not possible to hold all parameters (as we have defined them) constant for different ejecta. For instance, we cannot have the same core velocity and density for different ejecta masses. What actually is constant here is the core velocity, the *method* to apply mixing and allocate filling factors, and the positron and dust treatment. What is not constant is then the density and filling factors of the core zones (apart from the oxygen clumps whose density is forced to be constant).

In the NIR, the largest differences are seen in [S I] 1.083 μm , and Si I 1.60, 1.64 μm (Fig. 22).

4.2.2. Mixing

The mixing affects the emergent spectra in several different ways. First of all the mixing of the ⁵⁶Ni with the rest of the ejecta determines the energy deposition into the various zones. More outmixed ⁵⁶Ni gives lower total energy deposition and thus dimmer nebular spectra. Very temperature-sensitive lines, such as [O I] $\lambda 5577$ show the strongest drops when the deposition decreases (Fig. 24). Second, since different zones have quite different opacities due to their differing metal content, the mixing affects the radiative transport and the line blocking effect discussed earlier.

To be completed, two models differing only in mixing currently lacking to use as foundation for discussion...

4.2.3. Positron trapping

For the first 200-300 days gamma-rays dominate the energy deposition throughout the nebula, and the treatment of the positrons has little impact. However, after that time the fraction of gamma-rays that are trapped becomes small enough that the treatment of the positrons makes a difference for the spectra.

To study the influence of the positron treatment, we compare models 13A (non-local) and 13B (local). As a first observation, note how the non-local model (13A) gives an [O I] $\lambda\lambda 6300, 6364$ doublet that does not fall off in time as observed (Fig. 8). The on-the-spot model (13B) gives a better reproduction of the thermal evolution of the oxygen layers. A caveat here, however, is that if molecular cooling is strongly time-dependent, it will change these curves.

The magnesium recombination lines also become brighter in the non-local model (Fig. 17), not because magnesium becomes more highly ionized (is almost 100% ionized throughout most models), but **instead because** the electron fraction increases when the non-thermal ionization rate increases.

Fig. 25 compares models 13A and 13B at 400 days. As the Fe clumps receive less energy input in the non-local models, they are cooler and emit weaker iron-group lines. The [Co II] $\lambda 10200$ line is about 1/3 weaker in model 13A than in 13B. Unfortunately, at the time of the last NIR spectrum (200 days), the difference in this line as well as in the iron lines is only 10%.

In the optical, the line that is most strongly affected is [Fe II] $\lambda 7155$. With on-the-spot absorption, this line is significantly stronger than in the non-local model. The observed line **at late times** in SN 2011dh appears to fit the non-local scenario better (**Fig. 1, 25**), although the vicinity to the strong [Ca II] doublet complicates the analysis. At 400 days, the non-local model produces no detectable line at all, and the on-the-spot model produces one that is several times too strong.

We thus find no satisfying solution to this situation. It appears that wherever we put the positrons, they produce too strong emission lines - too strong [O I] $\lambda\lambda 6300, 6364$ and [Ca II] $\lambda\lambda 7291, 7323$ if allowed to stream into the oxygen and silicon zones, and too strong [Fe II] $\lambda 7155$ if trapped locally in the iron clumps. The situation is reminiscent of attempts to understand the spectrum of SN 1987A at an age of eight years, where similar results were obtained (but for [Fe II] 26 μm instead of [Fe II] $\lambda 7155$) (Jerkstrand et al. 2011). The situation is puzzling, and we encourage further research into the question. Many possible solutions are conceivable, such as significant reemission by dust or molecules in whatever zones the positrons deposit their en-

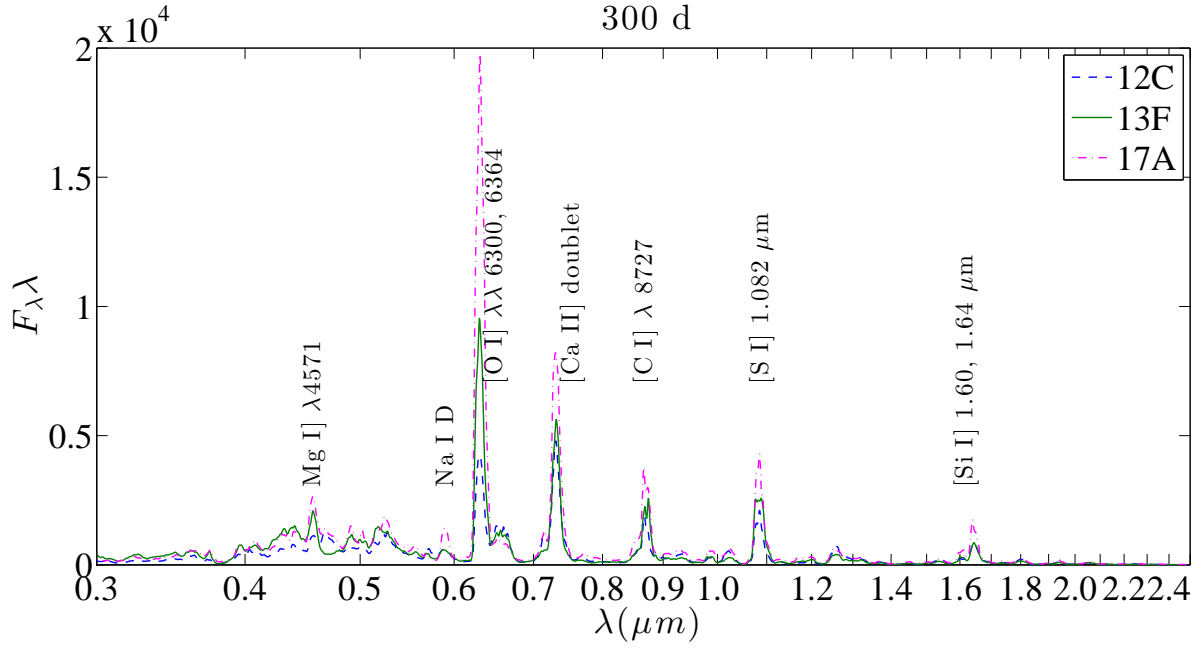


Fig. 22. The optical/NIR spectrum at 300 days for different progenitor masses (models 12C, 13F, and 17A).

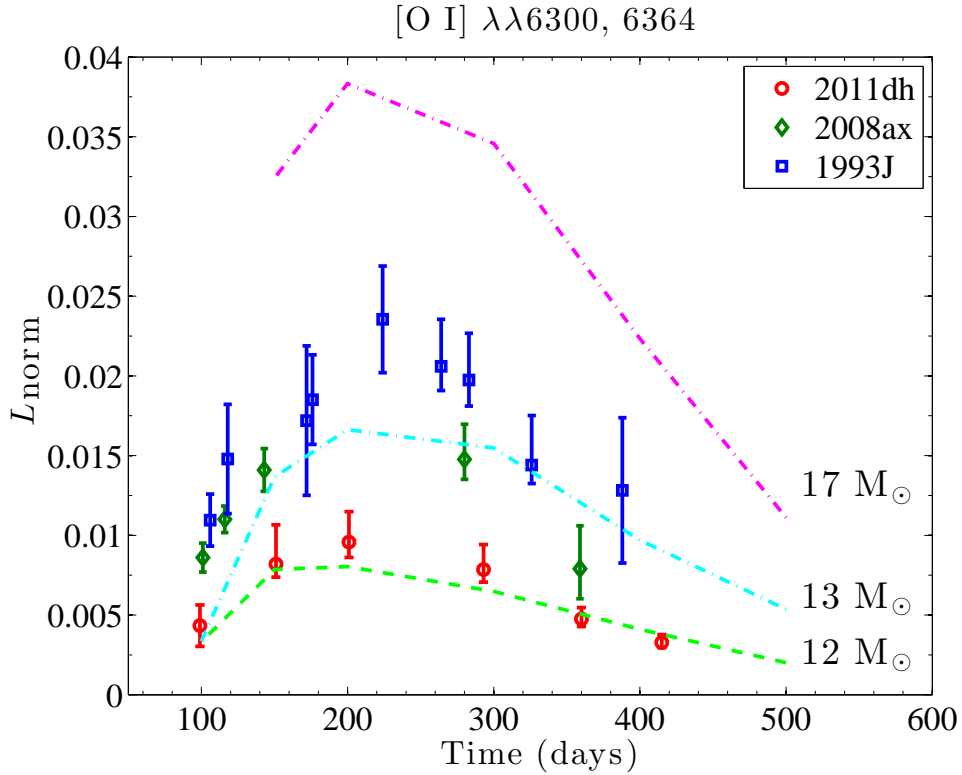


Fig. 23. The ratio of the luminosity in [O I] $\lambda\lambda 6300, 6364$ to the total ^{56}Co decay power for SN 2011dh, SN 2008ax, and SN 1993J, compared to model values for various progenitor masses (models 12C, 13F, and 17A). **This is the same figure as Fig. 8 but with only these three models plotted.**

ergy in. This is an attractive scenario given the strong emission by SN 2011dh in the MIR at late times (Ergon+2014).

4.2.4. Molecular cooling

Models with molecular cooling have their thermal emission from the O/Si/S and O/C zones damped out. The lines that are mainly

affected are [Ca II] $\lambda\lambda 7291, 7323$ (from the O/Si/S zone), [S I] $1.082 \mu\text{m}$ (O/Si/S zone), [O I] $\lambda\lambda 6300, 6364$ (O/Si/S and O/C zones), C I 4620 (O/C zone) and [C I] $\lambda 8727$ (O/C zone). As Fig. 26 shows, the impact is large on [O I] $\lambda 5577$, which is temperature sensitive, and [C I] $\lambda 8727$, which is the dominant cooler of the O/C zone in the absence of CO cooling. The observed blend of the Ca II triplet and the [C I] $\lambda 8727$ line at 200 days is sig-

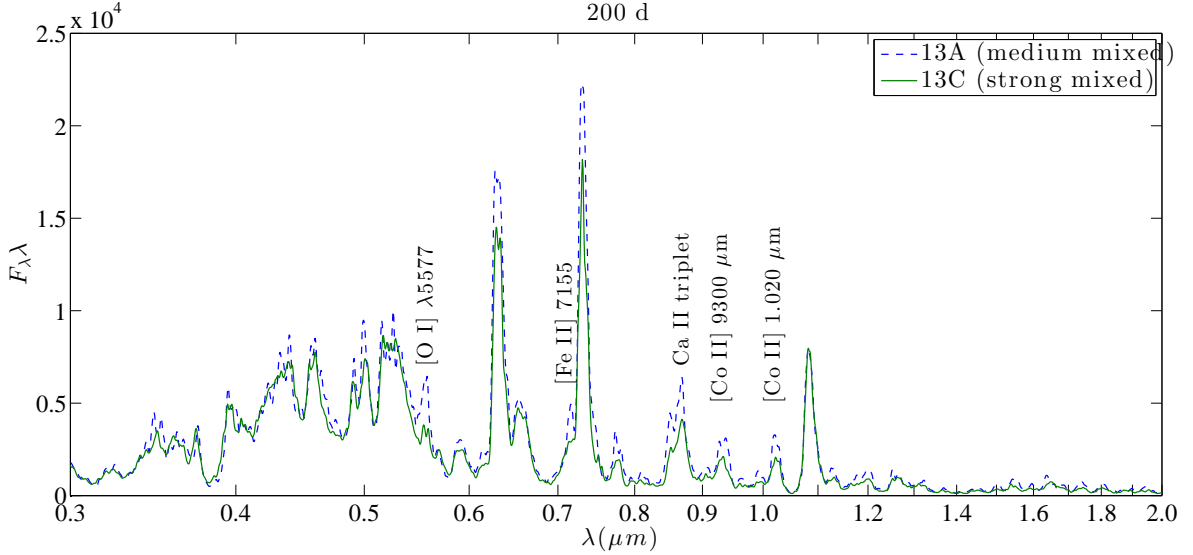


Fig. 24. A comparison of models with medium mixing (13A, blue dashed) and strong mixing (13C, black solid) at 200 days. The lines showing the strongest sensitivity to the mixing are marked.

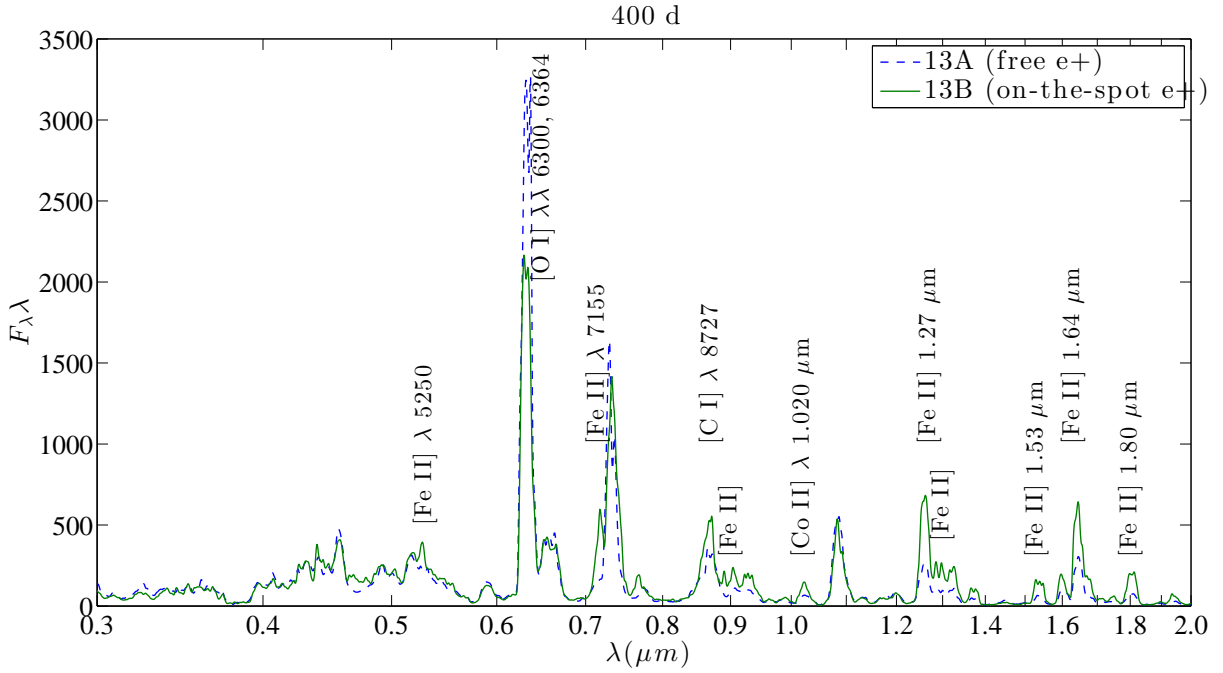


Fig. 25. A comparison of models with non-local positrons (13A, blue dashed) and on-the-spot absorbed positrons (13B, green solid) at 400 days. The lines showing the strongest sensitivity to the positron treatment are marked.

nificantly better reproduced in models with no CO cooling than those with (as seen by combining Figs. 1 (middle) and 26).

The impact of the molecular cooling depends on the progenitor mass, as the relative masses of the O/Si/S, O/Ne/Mg, and O/C zones vary with progenitor mass. For instance, at $M_{ZAMS} = 12 M_{\odot}$, these zone masses are 0.12, 0.13 and 0.15 M_{\odot} , whereas at $M_{ZAMS} = 18 M_{\odot}$ they are 0.24, 1.4 and 0.55. Since the O/Ne/Mg zone is much more massive than the others in high-mass progenitors, the impact of molecular cooling on the oxygen lines is much smaller, since molecules form mainly in the O/Si/S and O/C layers (SiO and CO, respectively). For low-mass progenitors, on the other hand, $\sim 2/3$ of the oxygen mass resides in

the O/Si/S and O/C layers, and the oxygen emission is much more sensitive to the molecular chemistry.

The consequence is that the conclusions regarding upper limits to the progenitor masses based on the [O I] $\lambda\lambda 6300, 6364$ lines are robust with respect to uncertainties in molecular cooling. A 17 M_{\odot} model with molecular cooling has only $\sim 1/3$ weaker [O I] $\lambda 6300, 6364$ emission than a model without molecular cooling, and still overproduces the observed [O I] $\lambda\lambda 6300, 6364$ emission in the observed sample Fig. 23).

Further discussion about molecular cooling, including the influence of the molecules in the MIR, is given in Ergon & Jerkstrand (2014).

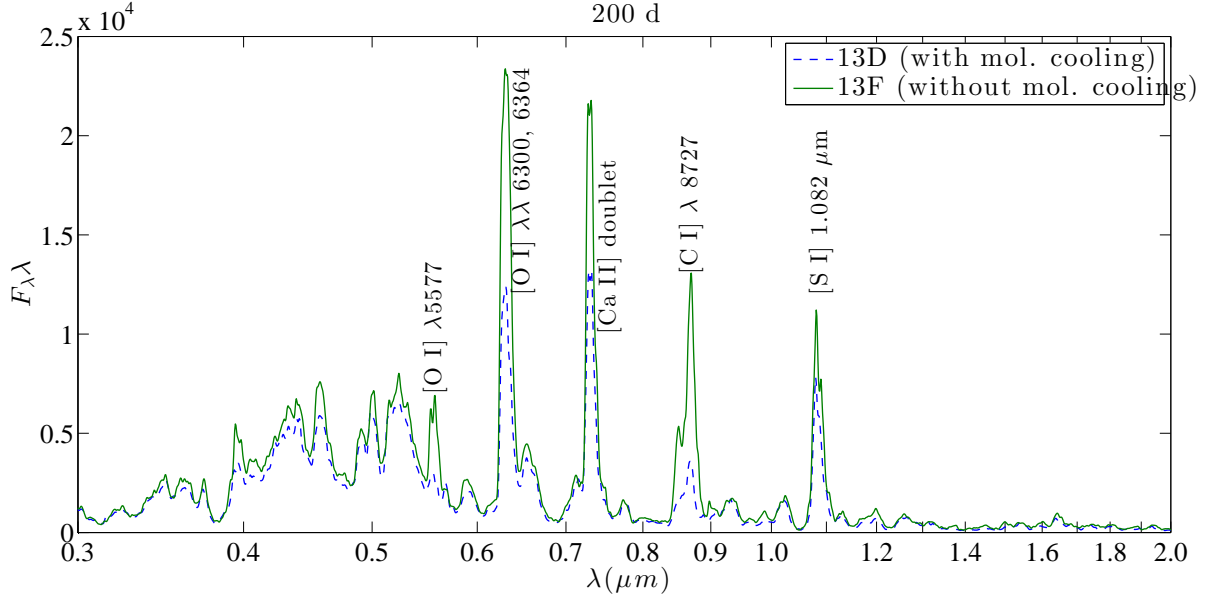


Fig. 26. A comparison of models with (13D, blue dashed) and without (13F, green solid) molecular cooling of the O/Si/S and O/C zones, at 200 days. The lines showing the strongest sensitivity to molecular cooling are marked.

4.2.5. Dust

The effects of dust on the emergent SED of the supernova is discussed in detail in Ergon & Jerkstrand (2014). The main influence of the dust on the optical/NIR is twofold; it suppresses the flux levels approximately by $1 - \exp(-\tau_{dust})$ and it leads to line profile distortions. The emission line profiles become distorted and blueshifted due to the preferential blocking of emission from the receding side of the ejecta. Fig. 27 shows an example by comparing the model Mg I] $\lambda 4571$ line at 400 days in a model with and without dust. In models with a **uniform dust distribution**, the peaks are blueshifted by an amount given by (Lucy et al. 1991) $\Delta V = V_{emit} [(\ln(1 + \tau)) / \tau - 1]$ which is $\sim 400 \text{ km s}^{-1}$ for $V_{emit} = 3500 \text{ km s}^{-1}$ and $\tau = 0.25$. This distortion further complicates the interpretation of the observed line profiles, as the mechanism is similar to the one of line opacity discussed in Sect. 4.1.5. **Whereas the line blocking must always decrease with time, dust blocking can both increase and decrease with time. If the dust is optically thin, an increase of its blocking will occur if dust growth occurs faster than the t^{-2} decline of the column densities. If the dust is optically thick, the blocking will be proportional to the amount at any given time.**

In SN 2011dh the blueshifts appear to decrease with time, and to disappear by 400 days (Sect. 4.1.5). This is difficult to reconcile with the signs of strong dust emission in the MIR throughout the 100-700 day range (Ergon & Jerkstrand 2014); if this dust resides in the ejecta it should lead to obscuration effects on the lines, shifting the peaks by several 100 km s^{-1} . In SN 1993J and SN 2008ax, on the other hand, the blueshifts do not appear to disappear with time (Table 7). One possibility is that we have a complex situation where early on the metal core has optical opacity due to line blocking, and later on due to dust, with perhaps an intermediate regime with both effects. Nevertheless this does still not explain how SN 2011dh can have dust emission without any noticeable effects on the line profiles at 400 days. **A possible geometry which could allow for such a combination is to have the dust region outside the line emitting region, such as in a shell. But also the other extreme, a dust region**

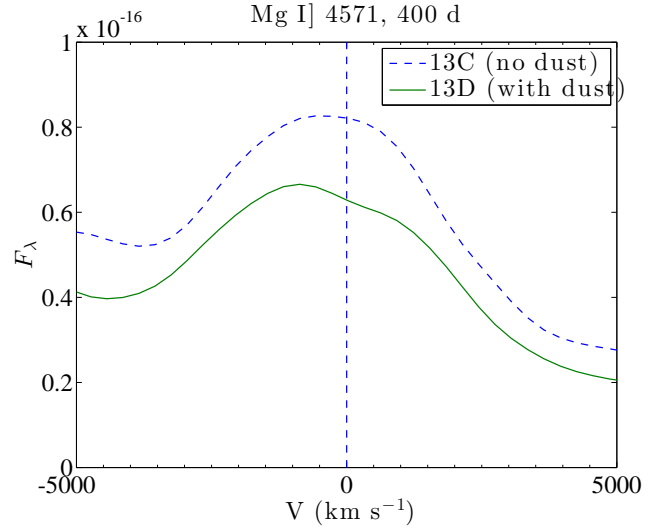


Fig. 27. The Mg I] $\lambda 4571$ line profile at 400 days in a model without (13C, blue dashed) and with (13D, green solid) dust. The peak of the line is blueshifted in the model with dust.

occupying only a small inner part of the line emitting region, might explain the situation.

4.2.6. Oxygen zone density

The influence of the oxygen zone is discussed in detail in Section 4.1.5 and 4.1.7. To recap, the density has (to first order) a weak influence on recombination lines from dominant species, as their ionized fractions adapt such that $Vn_e n_+$ stays constant (the amount of non-thermal ionization energy available for reemission changes only weakly with density (Kozma & Fransson 1992)). On the other hand, the influence on recombination lines of minor species like magnesium and sodium can be much larger, as these are often radiatively ionized and tend to stay fully ionized over a broad range of densities. Without any adaptation in the ionization balance, their emissivity depends on

n_e/V , a quantity that approximately grows with $f^{-1/2}$. Thus, doubling the zone density gives roughly a factor $\sqrt{2}$ increase in such recombination lines.

Fig. 28 compares models with low and high O-zone densities. It is clear that apart from the Mg recombination lines, the differences are small, as expected from the arguments above.

5. Discussion

Observations and modeling of SNe in the nebular phase allow critical tests to be made for our fundamental theories of the evolution and nucleosynthesis of massive stars. Undoubtedly, the rather close match between observed and modelled spectra demonstrate that current models for what supernova ejecta consist of are reasonably correct. This provides important support for the general validity of many uncertain assumptions that underpin modern calculations (which are still in 1D), for instance regarding convective mixing in the late stages of stellar evolution (Arnett & Meakin 2011).

Yet, the road to high-precision determination of yields is still long and winding. Both the chemical composition of heavy element nucleosynthesis ashes, and physical conditions are unique in SN ejecta, and this sometimes means that important atomic data has not been calculated. The other major stumbling block is to obtain realistic hydrodynamic structures; our reasoning is almost always.

The only detailed previous modelling done for nebular Type IIb SNe is that by Houck & Fransson (1996) for SN 1993J. Here a satisfactory reproduction of the spectrum, and in particular of the [O I] $\lambda\lambda 6300, 6364$ lines, were achieved with the SN ejecta from a $4.0 M_{\odot}$ helium core progenitor, with an oxygen mass of $0.5 M_{\odot}$. The modelling here gives a similar result; ejecta from the $M_{ZAMS} = 15 M_{\odot}$ progenitor of WH07 (which ends with a helium core of $3.8 M_{\odot}$, and a oxygen mass of $0.8 M_{\odot}$) gives the best fit to the thermal oxygen lines, with lower and higher helium core masses over and underproducing (Figs. 8,4). These results are in agreement with the progenitor luminosity of $\log L/L_{\odot} \sim 5.0$ (Aldering et al. 1994), which correspond to the model luminosity in helium cores of mass $4-5 M_{\odot}$ (Woosley et al. 1994).

For the Type IIb class, observations and modeling of progenitors, the diffusion phase light curve, and nebular phase spectra are at this point in quite satisfactory agreement with each other regarding the nature of Type IIb explosions. Of the three best observed events, two (SN 1993J and SN 2011dh) had yellow supergiant progenitors (Aldering et al. 1994; Maund et al. 2011) that ejected $\sim 2-3 M_{\odot}$ of material (Woosley et al. 1994; Bersten et al. 2012; Ergon & Jerkstrand 2014), and created nucleosynthesis products in agreement with $12 - 16 M_{\odot}$ progenitors (Houck & Fransson 1996; Shivvers et al. 2013, this paper). Binary stellar evolution codes can explain the progenitor structures by Roche lobe overflow, although attempts to reproduce the observed rates have so far not been successful (Claeys et al. 2011), possibly due to the many uncertainties in the binary population properties. The search for the expected binary companion to SN 2011dh will provide a crucial test for the binary hypothesis, as it did for SN 1993J (Maund et al. 2004).

More information on SN 2011dh should be possible to extract from observations past the epoch investigated here. As the supernova evolves, the steadily decreasing densities eventually leads to breakdown of the steady-state assumption for the energy equation as well as for the ionization balance. Up to 500

days most of the ejecta are still at high enough density to allow a steady-state treatment, but after this time time-dependent analysis is needed. As there are data on SN 2011dh up to 700 days, such an analysis would be highly interesting.

6. Summary and conclusions

We have investigated optical/NIR line formation processes in Type IIb SNe from 100 to 500 days, by computing emergent spectra with NLTE radiative transfer simulations. We find the principal components of the nebular spectra to be cooling and recombination emission from hydrostatic burning ashes ([O I] $\lambda\lambda 6300, 6364$, [O I] $\lambda 5777$, O I $\lambda 7771$, O I $\lambda 9263$, O I $1.130 \mu\text{m}$, O I $1.31 \mu\text{m}$, Mg I] $\lambda 4571$, Mg I $1.504 \mu\text{m}$, Na I-D) and from explosive burning ashes ([Ca II] $\lambda\lambda 7291, 7323$, [Si I] $\lambda\lambda 1.60, 1.64 \mu\text{m}$, [S I] $1.082 \mu\text{m}$, [Fe II] $\lambda 7155$). In addition **primordial** H, He, and N contribute emission lines to the spectrum. CNO-burning in the **progenitor star** leaves a large amount of nitrogen in the helium envelope, **which leads to [N II] $\lambda\lambda 6548, 6583$ emission dominating $H\alpha$ emission** in our models, and successfully reproduces the observations. This result is made further robust by the emergence of [N II] $\lambda 5754$ in all three SNe. We find the H envelopes in Type IIb SNe to be too small to produce any significant $H\alpha$ emission in the 100-500 day range. .

We compare our model calculations with data on the three **closest and best observed** Type IIb SNe to-date - SN 1993J, SN 2008ax, and SN 2011dh. Since oxygen nucleosynthesis depends sensitively on the progenitor mass of the star, the modeling constrains the progenitors of these three SNe to the $12 - 16 M_{\odot}$ range (**ejected oxygen masses between $0.3-0.9 M_{\odot}$**), with SN 2011dh towards the lower end of the range and SN 1993J towards the upper. With the velocity limits obtained from the observed spectra, the high ejecta mass from $M_{ZAMS} > 17 M_{\odot}$ progenitors give too bright cooling lines to match the observed line luminosities. Nucleosynthesis analysis thus supports a low/moderate mass origin for Type IIb SNe, and by implication binary progenitor systems. There may still be a high-mass star channel producing Type IIb events, but with the three best observed events all falling in the low-mass range, the binary channel appears to be dominant.

Oxygen and magnesium recombination lines are bright in SN 2011dh, and suggest a clumpy ejecta distribution, with the line forming clumps occupying only a small fraction ($\sim 1\%$) of the core volume. This finding should put constraints on multidimensional explosion simulations of this type of SNe.

Even as steady-state conditions set in after $\sim 50-100$ days in Type IIb and Ib ejecta, the large velocity gradients lead to significant line blocking effects for several hundred days. We have shown here how these radiative transfer effects lead to blue-shifted emission line profiles in lines such as Mg I] $\lambda 4571$ and [O I] $\lambda\lambda 6300, 6364$, an effect which gradually disappears with time as the densities decrease. The model evolution of this effect reproduces the observed line profile evolution in SN 2011dh well, but in SN 1993J and SN 2008ax the time evolution is not seen, possibly due to higher ejecta masses or intrinsic asymmetries in these SNe.

Appendix A: Element contributions

As an overview of the contributions by all major elements to the spectral formation in Type IIb SNe, and for future guidance in line identification, Figs. A.1 to A.12 show the contribution by all major elements to the emergent spectra in the 100 - 500 day interval. See the main text for more information.

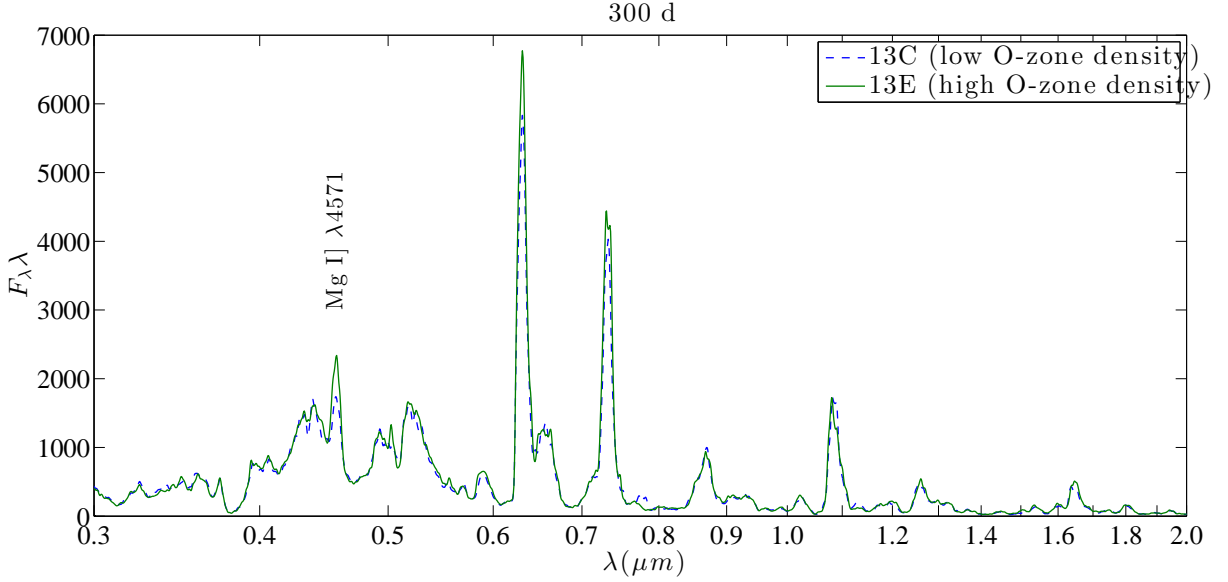


Fig. 28. A comparison of models with low (13C) and high (13E) oxygen zone densities, at 300 days. The lines showing the strongest sensitivity to the oxygen zone density are marked.

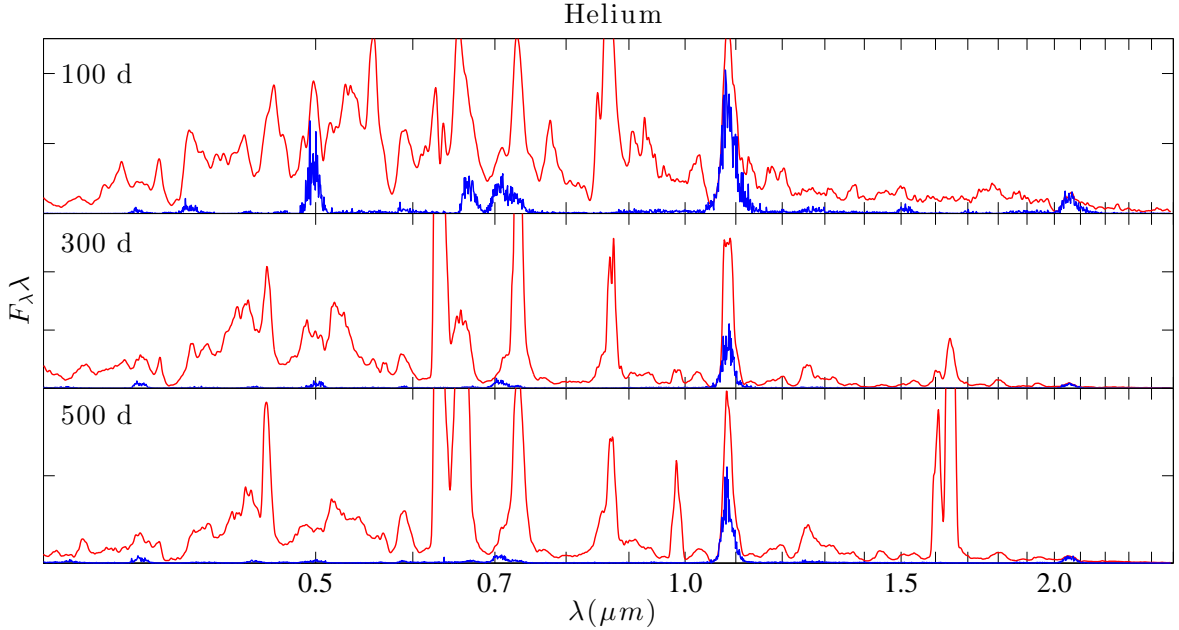


Fig. A.1. The contribution by helium lines (blue) to the spectrum in model 13F (red), at 100, 300 and 500 days.

Appendix B: Code updates

B.1. Lorentz factors

The velocities in stripped envelope core-collapse SNe are high enough (up to $0.1c$) that relativistic effects have some significance. We find that including the Lorentz factor in the Doppler formula

$$\frac{\Delta\lambda}{\lambda} = \gamma \frac{\Delta V}{c} \quad (\text{B.1})$$

where

$$\gamma = \frac{1}{\sqrt{1 - (\Delta V/c)^2}} \quad (\text{B.2})$$

produces noticeable wavelength shifts (of order $\gamma \sim 1\%$) in the emergent spectrum, and is therefore applied.

The relativistic effects on the intensity of the radiation is of less importance, and we postpone a treatment of this for future code upgrades.

B.2. Atomic data

- Mg I. Total recombination rate updated, now from Gould (1978). Also added dielectronic recombination from Nussbaumer & Storey (1986) to the total recombination rate. We compute specific recombination rates by applying the Milne relations to the TOPBASE photoionization cross sec-

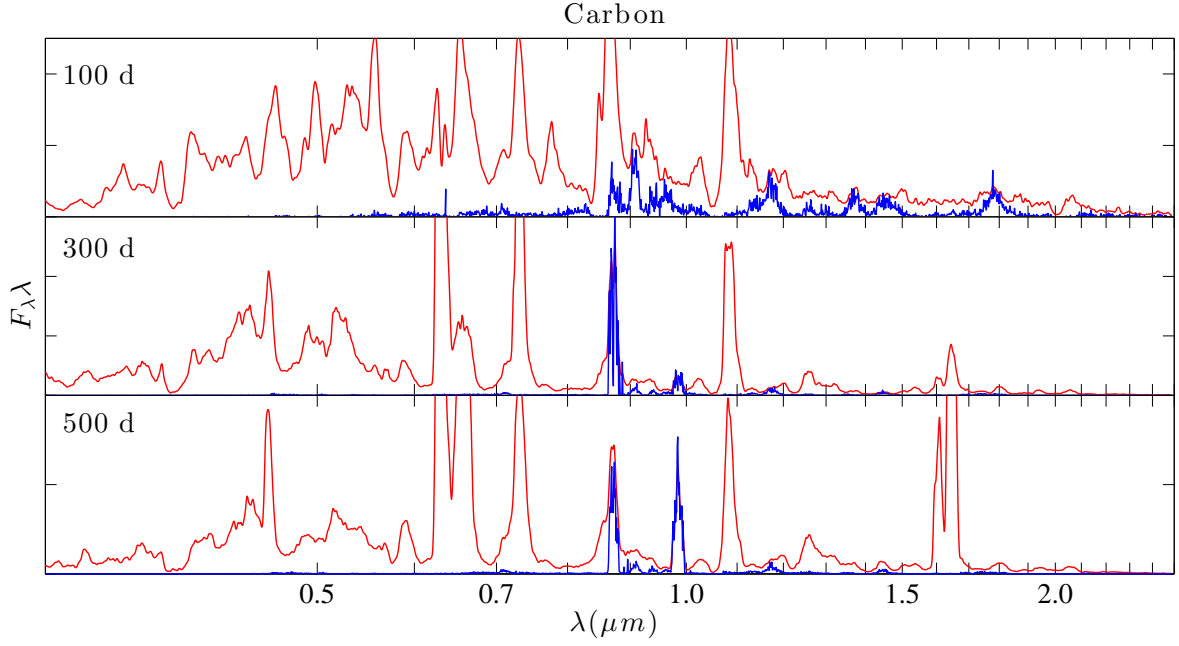


Fig. A.2. The contribution by carbon lines (blue) to the spectrum in model 13F (red), at 100, 300 and 500 days.

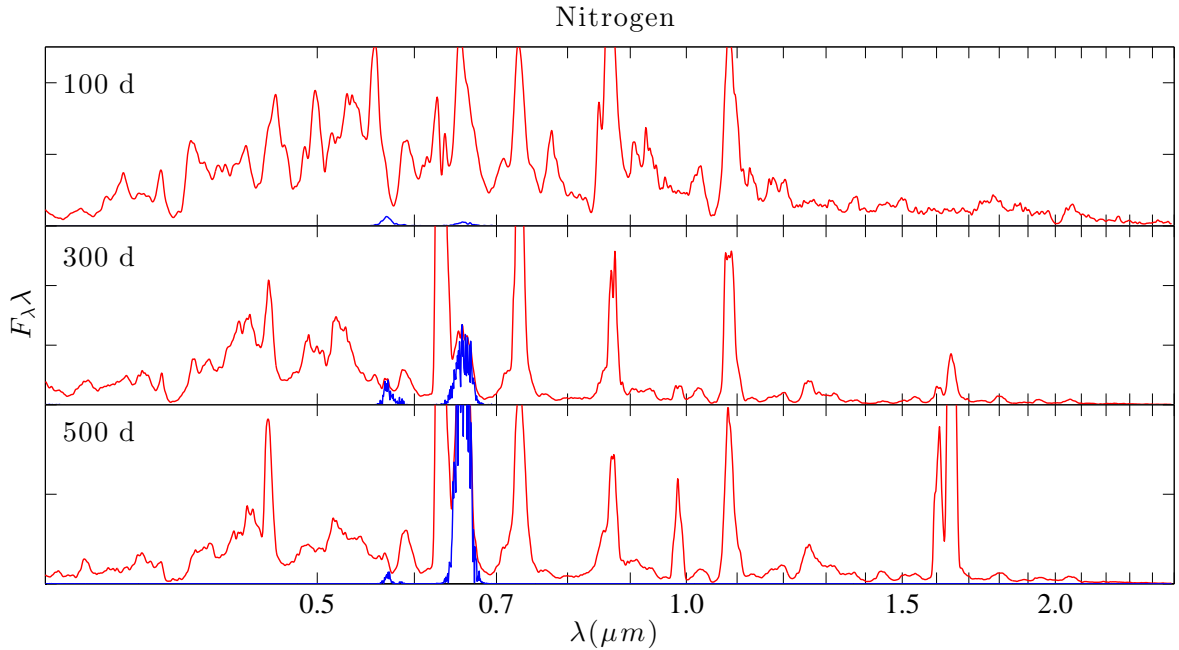


Fig. A.3. The contribution by nitrogen lines (blue) to the spectrum in model 13F (red), at 100, 300 and 500 days.

tions for the first 30 (up to $s6d^1D$) multiplets. The sum of these are in quite good agreement with the Gould rates; any missing recombinations (including dielectronic) are allocated to the higher states as discussed in J11/J12.

There are some issues with applying the Milne relations to the TOPBASE cross sections; these include ionization to excited states, whereas the bound-free cross section needed to compute recombination from the ground state in the ion refers to the ground state of the ion only. However, the first

excited state in Mg II has an excitation energy of 4.42 eV, so for the moderate temperatures ($T \lesssim 10^4$ K) of interest here, the contribution by excited states is negligible. A second complication is how to treat the autoionization resonances in the cross sections; they should not be included for computing the *radiative* free-bound cross section, but are associated with the dielectronic recombination. We currently leave them in, noting that they typically occur at several eV, and thus have a small influence. A final complication is that

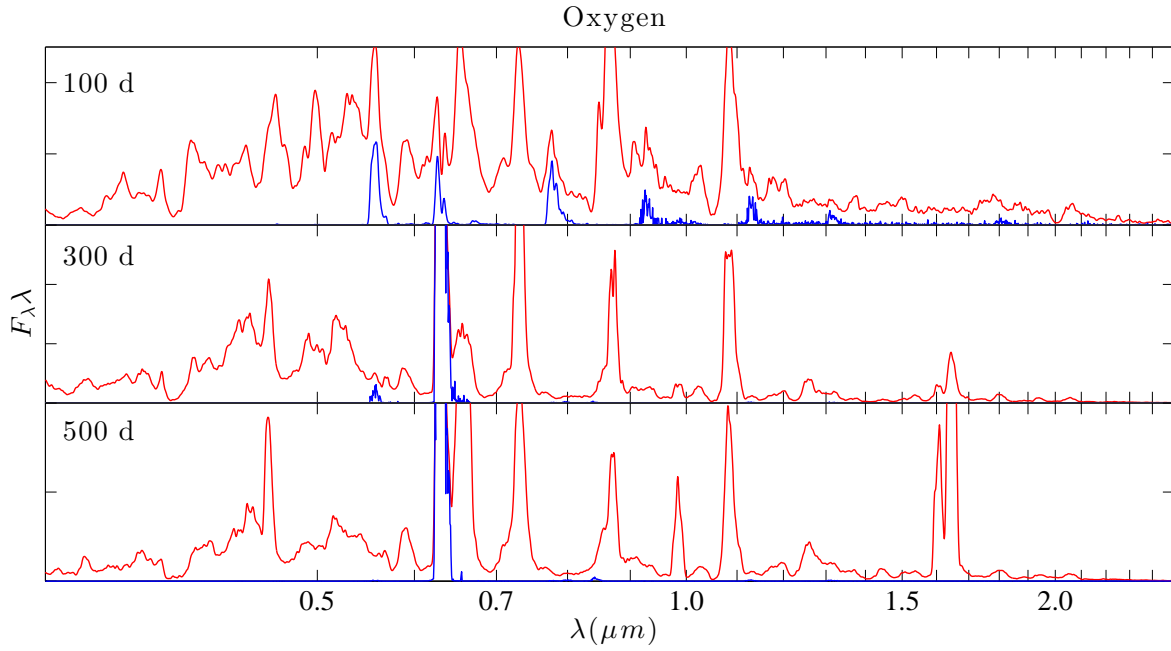


Fig. A.4. The contribution by oxygen lines (blue) to the spectrum in model 13F (red), at 100, 300 and 500 days.

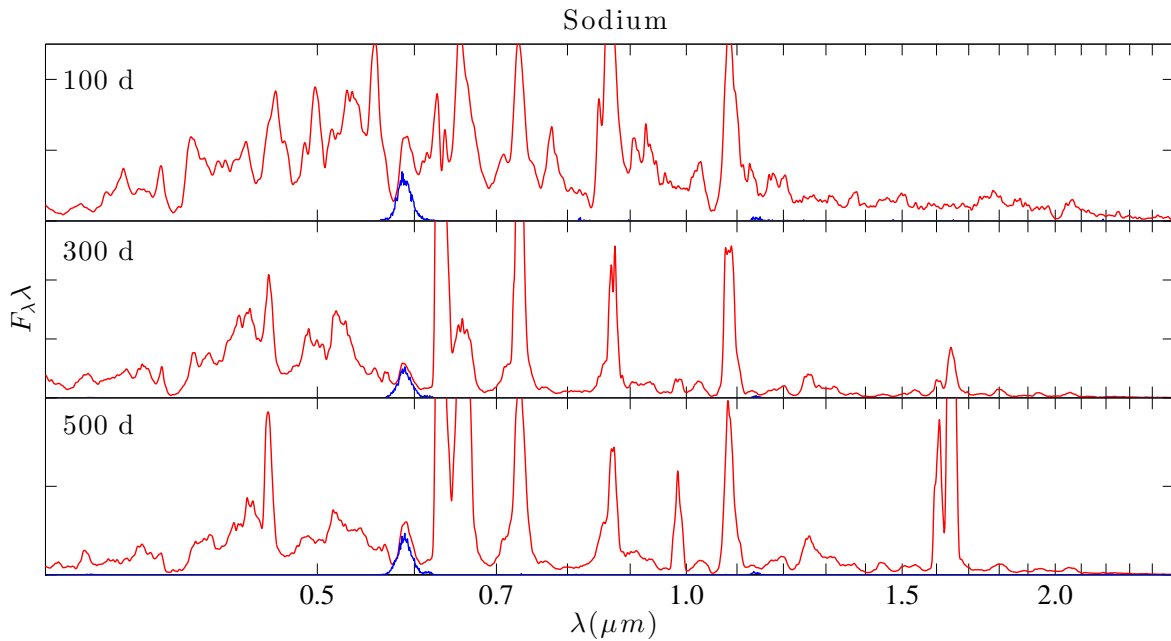


Fig. A.5. The contribution by sodium lines (blue) to the spectrum in model 13F (red), at 100, 300 and 500 days.

the ionization thresholds presented in TOPBASE are often somewhat offset from their correct values. One may choose to renormalize all energies to the correct threshold, here we have not done so (so we simply ignore any listed cross sections at energies below the true edge).

- Na I. Total recombination rate from Verner & Ferland (1996). Specific recombination rates for first 15 terms (up to $6d^2D$) computed from TOPBASE photoionization cross sections (same as in J11/J12). These cross sections are rel-

atively free from contributions by autoionization resonances and excited states in Na II. The collision strengths come from Trail et al. (1994) for the D line, and from Park (1971) for the other transitions. The Trail value is in good agreement with the more recent calculation by Gao et al. (2010).

- O I. Specific recombination rates from Nahar (1999) implemented for the first 26 terms (up to $5f^3F$).
- Others. Added Ni III, with energy levels from Sugar & Corliss (1985) (up to $3d^8 1G$), A-values from Garstang

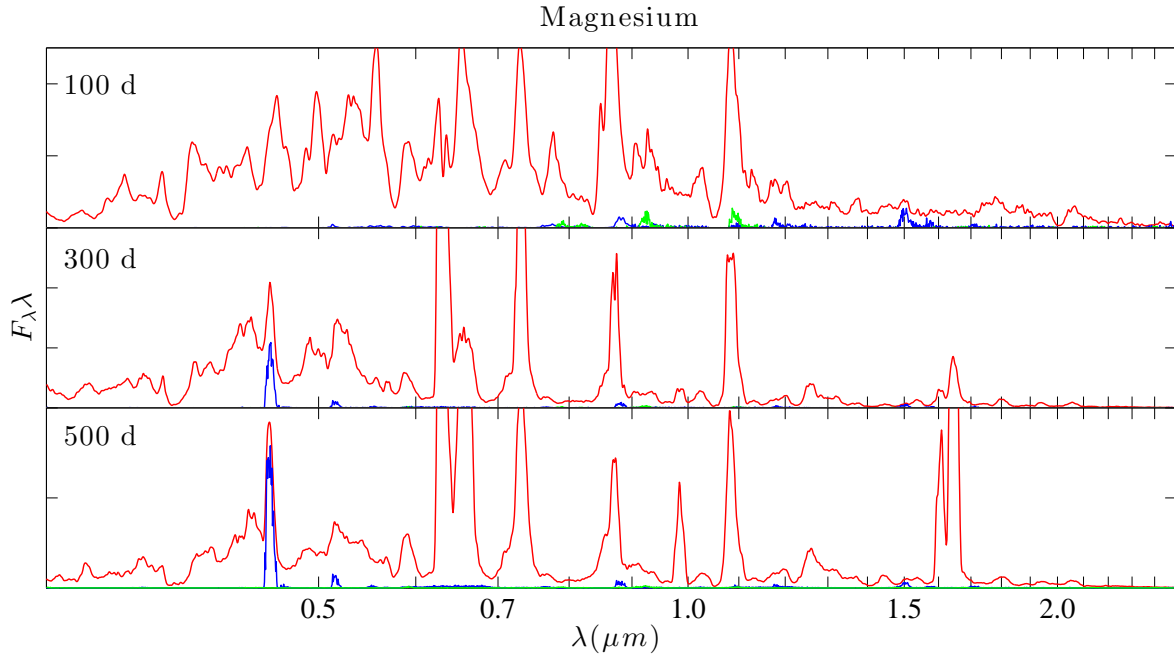


Fig. A.6. The contribution by Mg I lines (blue), Mg II lines (green) to the spectrum in model 13F (red), at 100, 300 and 500 days.

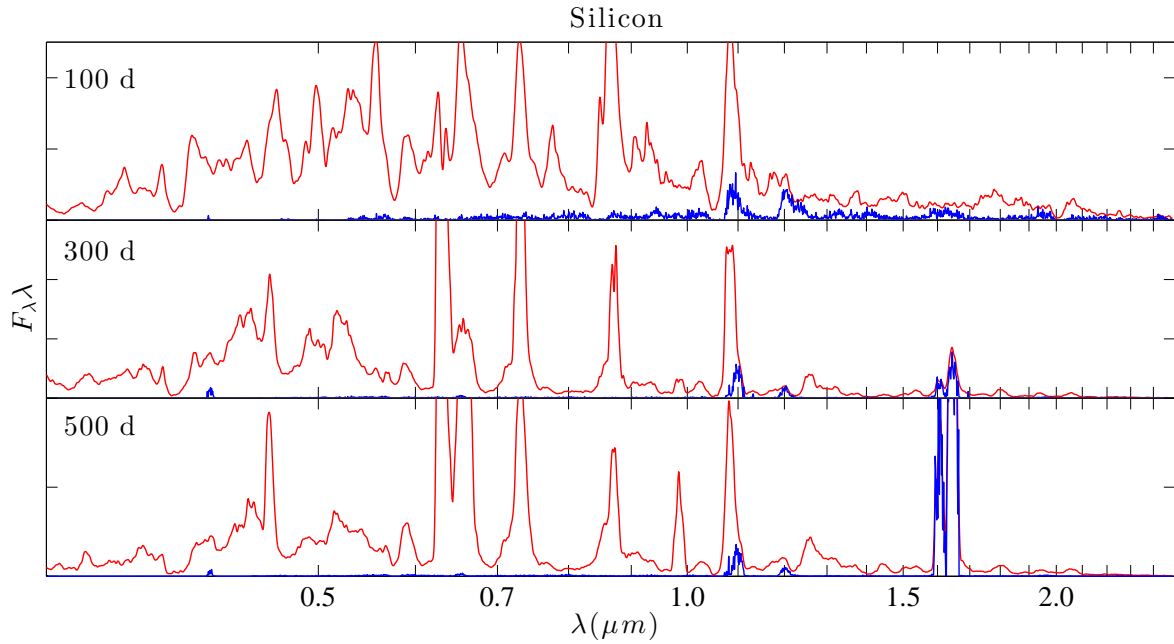


Fig. A.7. The contribution by Si I lines (blue) to the spectrum in model 13F (red), at 100, 300 and 500 days.

(1958), collision strengths (from ground multiplet only) from Bautista (2001). Added dielectronic recombination rates for Si I, Si II, S I, Ca I, Fe I, and Ni I (Shull & van Steenberg 1982). Added forbidden lines for Fe III, Co III, Al I, Al II, Ti I, Ti II, Ti III, Cr I, Cr II, Mn II, V I, V II, Sc I, Sc II (Kurucz). Added Fe III collision strengths from Zhang & Pradhan (1995b). Fe II collision strengths for the first 16 levels in Fe II now from Ramsbottom et al. (2007)

(higher levels from Zhang & Pradhan (1995a) and Bautista & Pradhan (1996)).

Appendix C: Ejecta models

References

- Aldering, G., Humphreys, R. M., & Richmond, M. 1994, AJ, 107, 662
 Arnett, W. D. & Meakin, C. 2011, ApJ, 733, 78
 Asplund, M., Grevesse, N., Sauval, A. J., & Scott, P. 2009, ARA&A, 47, 481

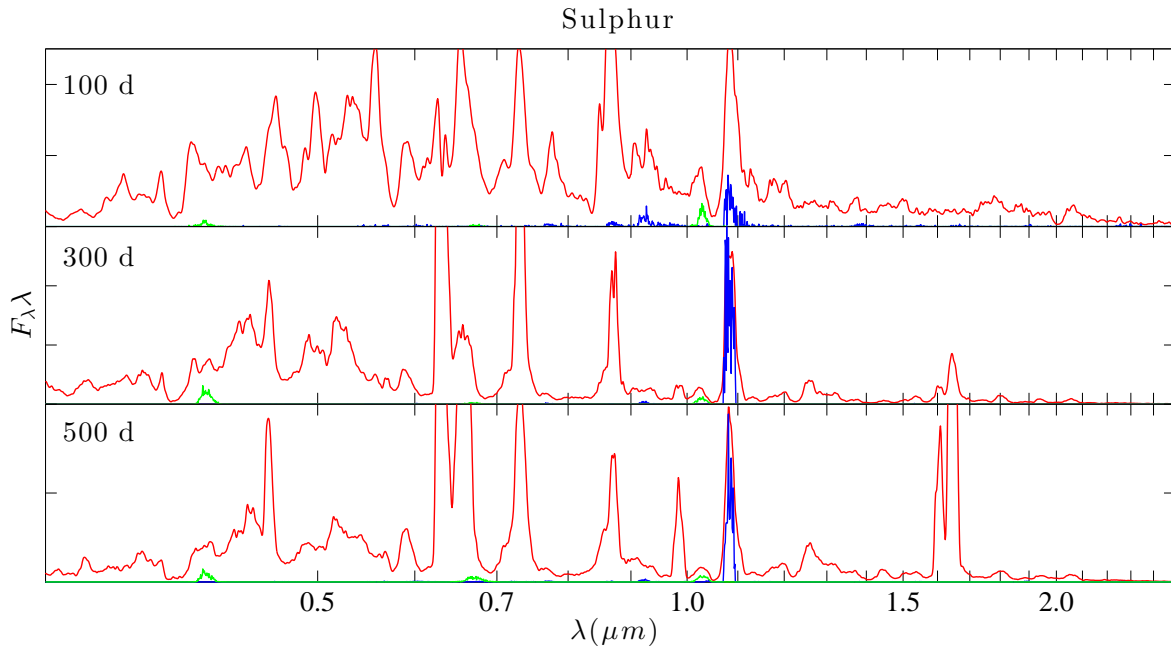


Fig. A.8. The contribution by S I lines (blue) and S II lines (green) to the spectrum in model 13F (red), at 100, 300 and 500 days.

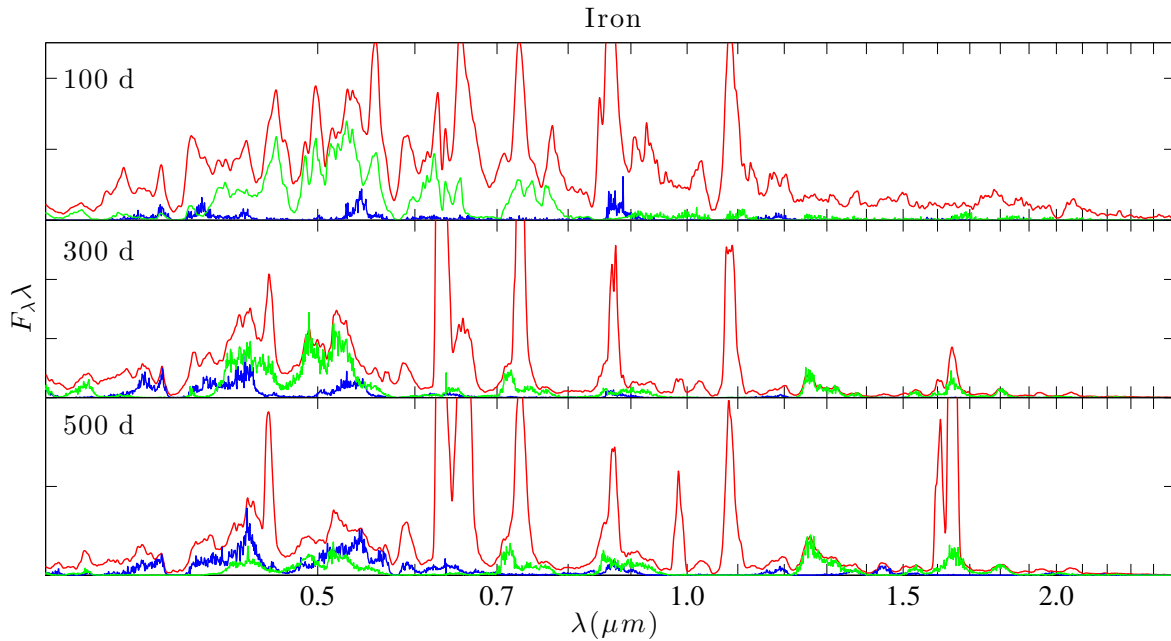


Fig. A.9. The contribution by Fe I lines (blue) and Fe II lines (green) to the spectrum in model 13F (red), at 100, 300 and 500 days.

Axelrod, T. S. 1980, PhD thesis, California Univ., Santa Cruz.
 Barbon, R., Benetti, S., Cappellaro, E., et al. 1995, *A&AS*, 110, 513
 Bautista, M. A. 2001, *A&A*, 365, 268
 Bautista, M. A. & Pradhan, A. K. 1996, *A&AS*, 115, 551
 Benjamin, R. A., Skillman, E. D., & Smits, D. P. 1999, *ApJ*, 514, 307
 Bersten, M. C., Benvenuto, O. G., Nomoto, K., et al. 2012, *ApJ*, 757, 31
 Bouchet, P. & Danziger, I. J. 1993, *A&A*, 273, 451
 Branch, D., Benetti, S., Kasen, D., et al. 2002, *ApJ*, 566, 1005
 Chiosi, C. & Maeder, A. 1986, *ARA&A*, 24, 329
 Claeys, J. S. W., de Mink, S. E., Pols, O. R., Eldridge, J. J., & Baes, M. 2011, *A&A*, 528, A131

Colgate, S. A., Petschek, A. G., & Kriese, J. T. 1980, *ApJ*, 237, L81
 Dessart, L. & Hillier, D. J. 2011, *MNRAS*, 410, 1739
 Eldridge, J. J., Fraser, M., Smartt, S. J., Maund, J. R., & Crockett, R. M. 2013, *MNRAS*, 436, 774
 Elias, J. H., Matthews, K., Neugebauer, G., & Persson, S. E. 1985, *ApJ*, 296, 379
 Elmhamdi, A., Danziger, I. J., Branch, D., et al. 2006, *A&A*, 450, 305
 Ensmann, L. M. & Woosley, S. E. 1988, *ApJ*, 333, 754
 Ergon, M. & Jerkstrand, A. 2014
 Ergon, M., Sollerman, J., Fraser, M., et al. 2013, ArXiv e-prints
 Ferrarese, L., Ford, H. C., Huchra, J., et al. 2000, *ApJS*, 128, 431
 Filippenko, A. V. 1988, *AJ*, 96, 1941

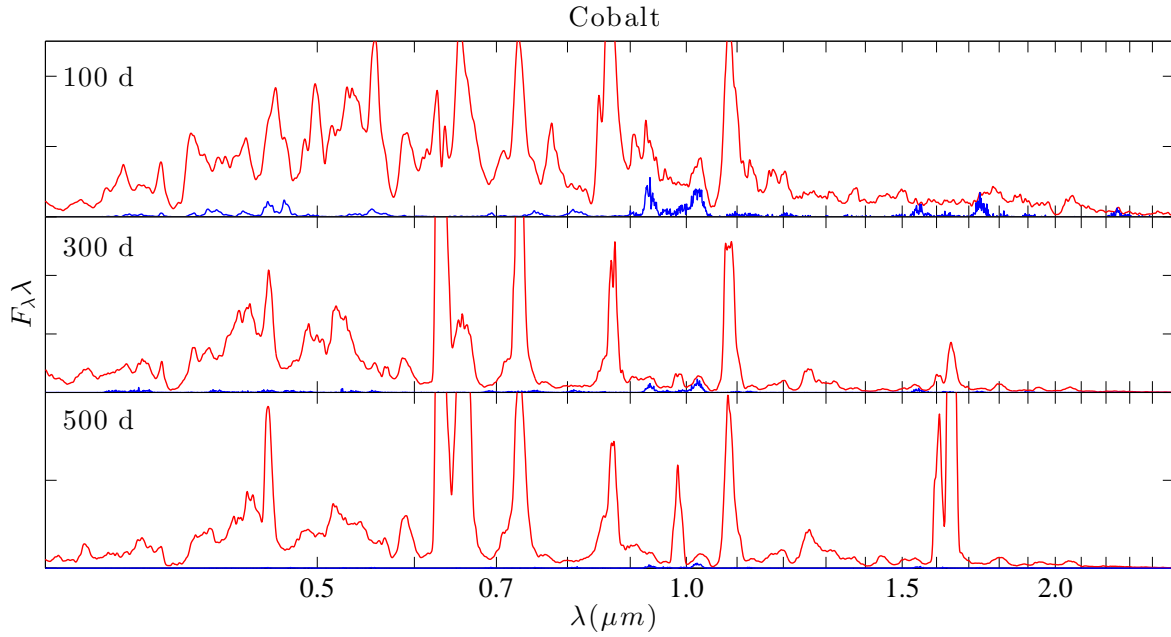


Fig. A.10. The contribution by Co II lines (blue) to the spectrum in model 13F (red), at 100, 300 and 500 days.

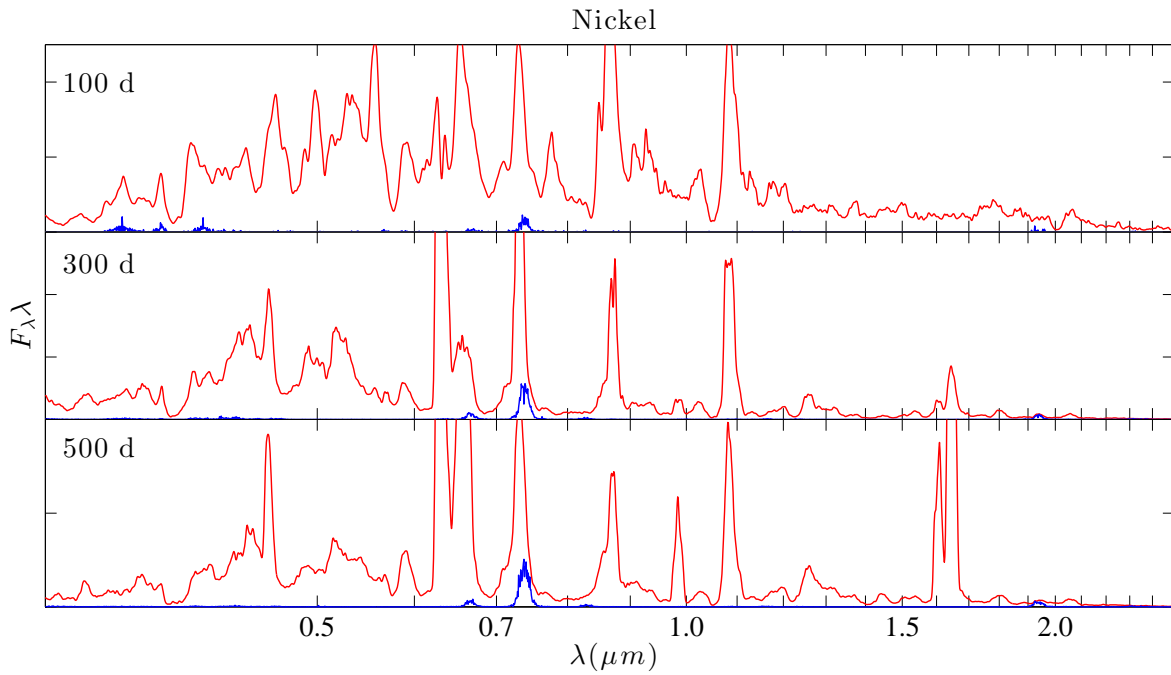


Fig. A.11. The contribution by Ni II lines (blue) to the spectrum in model 13F (red), at 100, 300 and 500 days.

Filippenko, A. V., Matheson, T., & Barth, A. J. 1994, *AJ*, 108, 2220
 Filippenko, A. V., Matheson, T., & Ho, L. C. 1993, *ApJ*, 415, L103
 Fransson, C., Challis, P. M., Chevalier, R. A., et al. 2005, *ApJ*, 622, 991
 Fransson, C. & Kozma, C. 1993, *ApJ*, 408, L25
 Freedman, W. L., Hughes, S. M., Madore, B. F., et al. 1994, *ApJ*, 427, 628
 Friesen, B., Baron, E., Branch, D., et al. 2012, *ApJS*, 203, 12
 Gao, X., Han, X.-Y., Vokly, L., Feautrier, N., & Li, J.-M. 2010, *Phys. Rev. A*, 81, 022703
 Garstang, R. H. 1958, *MNRAS*, 118, 234
 Gerardy, C. L., Fesen, R. A., Nomoto, K., et al. 2002, *PASJ*, 54, 905

Gould, R. J. 1978, *ApJ*, 219, 250
 Hachisu, I., Matsuda, T., Nomoto, K., & Shigeyama, T. 1991, *ApJ*, 368, L27
 Hachisu, I., Matsuda, T., Nomoto, K., & Shigeyama, T. 1994, *A&AS*, 104, 341
 Harkness, R. P., Wheeler, J. C., Margon, B., et al. 1987, *ApJ*, 317, 355
 Herant, M. & Benz, W. 1991, *ApJ*, 370, L81
 Houck, J. C. & Fransson, C. 1996, *ApJ*, 456, 811
 Hunter, D. J., Valenti, S., Kotak, R., et al. 2009, *A&A*, 508, 371
 Iwamoto, K., Young, T. R., Nakasato, N., et al. 1997, *ApJ*, 477, 865
 Jerkstrand, A., Fransson, C., & Kozma, C. 2011, *A&A*, 530, A45
 Jerkstrand, A., Fransson, C., Maguire, K., et al. 2012, *A&A*, 546, A28, (J12)

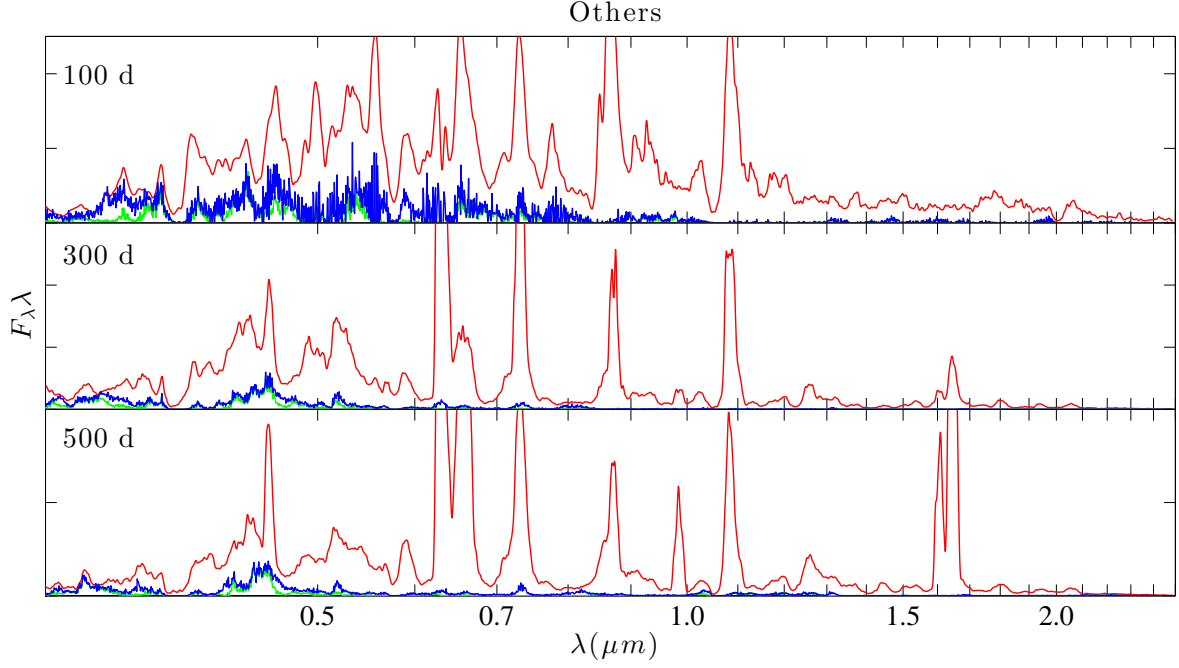


Fig. A.12. The contribution by all other lines (blue) and by Ti II (green) to the spectrum in model 13F (red), at 100, 300 and 500 days.

Table C.1. The chemical composition (mass fractions) of the $12 M_{\odot}$ models. **Abundances small than 10^{-9} are listed as zero.**

Element/Zone	Fe/He	Si/S	O/Si/S	O/Ne/Mg	O/C	He/C	He/N	H
$^{56}\text{Ni} + ^{56}\text{Co}$	6.3×10^{-1}	1.8×10^{-1}	2.6×10^{-6}	2.2×10^{-5}	1.3×10^{-5}	1.0×10^{-6}	1.1×10^{-7}	0
$^{57}\text{Ni} + ^{57}\text{Co}$	3.4×10^{-2}	2.7×10^{-3}	7.6×10^{-6}	1.5×10^{-6}	4.9×10^{-8}	4.4×10^{-9}	2.9×10^{-9}	0
^{44}Ti	5.0×10^{-4}	2.6×10^{-5}	3.0×10^{-7}	0	0	0	0	0
H	5.0×10^{-6}	1.2×10^{-6}	6.2×10^{-8}	7.0×10^{-9}	2.9×10^{-9}	2.0×10^{-9}	6.6×10^{-8}	5.4×10^{-1}
He	2.7×10^{-1}	7.3×10^{-6}	5.3×10^{-6}	4.4×10^{-6}	1.3×10^{-2}	6.7×10^{-1}	9.8×10^{-1}	4.4×10^{-1}
C	1.9×10^{-6}	2.1×10^{-5}	9.0×10^{-4}	3.8×10^{-3}	2.3×10^{-1}	2.7×10^{-1}	2.0×10^{-3}	1.2×10^{-4}
N	3.3×10^{-6}	4.6×10^{-7}	2.6×10^{-5}	4.1×10^{-5}	1.8×10^{-5}	3.5×10^{-6}	7.9×10^{-3}	1.0×10^{-2}
O	2.0×10^{-5}	1.1×10^{-2}	7.6×10^{-1}	6.8×10^{-1}	6.5×10^{-1}	3.3×10^{-2}	8.1×10^{-4}	5.0×10^{-3}
Ne	2.2×10^{-5}	1.5×10^{-5}	1.1×10^{-3}	2.2×10^{-1}	8.2×10^{-2}	1.8×10^{-2}	2.3×10^{-3}	1.2×10^{-3}
Na	9.4×10^{-7}	6.6×10^{-7}	2.5×10^{-5}	4.5×10^{-3}	1.6×10^{-4}	1.9×10^{-4}	1.7×10^{-4}	7.0×10^{-5}
Mg	4.2×10^{-5}	1.1×10^{-4}	3.5×10^{-2}	6.8×10^{-2}	2.5×10^{-2}	8.1×10^{-3}	7.2×10^{-4}	7.2×10^{-4}
Al	7.7×10^{-6}	1.5×10^{-4}	3.8×10^{-3}	5.4×10^{-3}	1.6×10^{-4}	9.7×10^{-5}	7.5×10^{-5}	7.0×10^{-5}
Si	2.1×10^{-4}	3.2×10^{-1}	1.5×10^{-1}	1.4×10^{-2}	1.7×10^{-3}	9.5×10^{-4}	8.2×10^{-4}	8.2×10^{-4}
S	2.1×10^{-4}	3.3×10^{-1}	3.8×10^{-2}	9.2×10^{-4}	2.3×10^{-4}	3.0×10^{-4}	4.2×10^{-4}	4.2×10^{-4}
Ar	2.3×10^{-4}	5.4×10^{-2}	4.2×10^{-3}	8.5×10^{-5}	8.0×10^{-5}	8.4×10^{-5}	1.1×10^{-4}	1.1×10^{-4}
Ca	2.7×10^{-3}	4.2×10^{-2}	9.6×10^{-4}	3.6×10^{-5}	2.5×10^{-5}	3.9×10^{-5}	7.3×10^{-5}	7.4×10^{-5}
Sc	2.2×10^{-7}	4.7×10^{-7}	2.8×10^{-7}	1.1×10^{-6}	1.4×10^{-6}	8.6×10^{-7}	6.6×10^{-8}	4.5×10^{-8}
Ti	1.6×10^{-3}	7.0×10^{-4}	2.4×10^{-5}	5.8×10^{-6}	5.8×10^{-6}	3.5×10^{-6}	3.4×10^{-6}	3.4×10^{-6}
V	4.8×10^{-5}	1.5×10^{-4}	4.5×10^{-6}	6.2×10^{-7}	7.7×10^{-7}	7.6×10^{-7}	4.6×10^{-7}	4.3×10^{-7}
Cr	2.4×10^{-3}	1.1×10^{-2}	7.5×10^{-5}	1.5×10^{-5}	1.2×10^{-5}	1.4×10^{-5}	2.0×10^{-5}	2.0×10^{-5}
Mn	1.7×10^{-6}	3.5×10^{-4}	1.1×10^{-5}	6.8×10^{-6}	4.0×10^{-6}	6.3×10^{-6}	1.6×10^{-5}	1.5×10^{-5}
Fe	8.0×10^{-4}	4.2×10^{-2}	7.9×10^{-4}	8.9×10^{-4}	6.9×10^{-4}	1.1×10^{-3}	1.4×10^{-3}	1.4×10^{-3}
Co	2.2×10^{-8}	1.2×10^{-8}	1.2×10^{-4}	1.4×10^{-4}	1.5×10^{-4}	1.1×10^{-4}	4.8×10^{-6}	4.0×10^{-6}
Ni	2.5×10^{-2}	3.1×10^{-3}	6.9×10^{-4}	4.3×10^{-4}	5.3×10^{-4}	3.2×10^{-4}	8.2×10^{-5}	8.2×10^{-5}

Jerkstrand, A., Smartt, S. J., Fraser, M., et al. 2013, ArXiv e-prints
 Kjær, K., Leibundgut, B., Fransson, C., Jerkstrand, A., & Spyromilio, J. 2010, A&A, 517, A51
 Kozma, C. & Fransson, C. 1992, ApJ, 390, 602
 Kozma, C. & Fransson, C. 1998, ApJ, 497, 431
 Lewis, J. R., Walton, N. A., Meikle, W. P. S., et al. 1994, MNRAS, 266, L27
 Li, H. & McCray, R. 1992, ApJ, 387, 309
 Li, H. & McCray, R. 1993, ApJ, 405, 730
 Li, H. & McCray, R. 1995, ApJ, 441, 821
 Li, H. & McCray, R. 1996, ApJ, 456, 370

Li, W., Leaman, J., Chornock, R., et al. 2011, MNRAS, 412, 1441
 Liu, W. & Dalgarno, A. 1994, ApJ, 428, 769
 Liu, W., Dalgarno, A., & Lepp, S. 1992, ApJ, 396, 679
 Lucy, L. B., Danziger, I. J., Gouffes, C., & Bouchet, P. 1991, in Supernovae, ed. S. E. Woosley, 82
 Matthews, K., Neugebauer, G., Armus, L., & Soifer, B. T. 2002, AJ, 123, 753
 Maund, J. R., Fraser, M., Ergon, M., et al. 2011, ApJ, 739, L37
 Maund, J. R., Smartt, S. J., Kudritzki, R. P., Podsiadlowski, P., & Gilmore, G. F. 2004, Nature, 427, 129
 Maurer, I., Jerkstrand, A., Mazzali, P. A., et al. 2011, MNRAS, 418, 1517

Table C.2. Same as Table C.1 for the 13 M_{\odot} models.

Element/Zone	Fe/He	Si/S	O/Si/S	O/Ne/Mg	O/C	He/C	He/N	H
$^{56}\text{Ni} + ^{56}\text{Co}$	7.4×10^{-1}	7.2×10^{-2}	4.8×10^{-6}	3.0×10^{-5}	1.3×10^{-5}	1.3×10^{-6}	2.5×10^{-8}	0
$^{57}\text{Ni} + ^{57}\text{Co}$	3.2×10^{-2}	1.5×10^{-3}	9.6×10^{-6}	1.4×10^{-6}	3.0×10^{-8}	7.4×10^{-9}	3.0×10^{-9}	0
^{44}Ti	2.6×10^{-4}	2.0×10^{-5}	3.1×10^{-7}	0	0	0	0	0
H	5.3×10^{-6}	8.9×10^{-7}	4.5×10^{-8}	3.7×10^{-9}	1.4×10^{-9}	0	1.3×10^{-7}	5.4×10^{-1}
He	1.4×10^{-1}	9.1×10^{-6}	5.0×10^{-6}	3.6×10^{-6}	4.2×10^{-2}	8.2×10^{-1}	9.9×10^{-1}	4.4×10^{-1}
C	3.1×10^{-7}	2.0×10^{-5}	1.2×10^{-3}	6.6×10^{-3}	2.5×10^{-1}	1.5×10^{-1}	4.2×10^{-4}	1.2×10^{-4}
N	2.0×10^{-6}	5.1×10^{-7}	2.9×10^{-5}	3.5×10^{-5}	1.3×10^{-5}	4.1×10^{-5}	8.4×10^{-3}	1.0×10^{-2}
O	8.8×10^{-6}	1.1×10^{-2}	7.5×10^{-1}	7.2×10^{-1}	6.4×10^{-1}	1.3×10^{-2}	7.8×10^{-4}	4.8×10^{-3}
Ne	1.0×10^{-5}	1.8×10^{-5}	2.4×10^{-3}	1.4×10^{-1}	5.6×10^{-2}	1.4×10^{-2}	1.4×10^{-3}	1.2×10^{-3}
Na	6.7×10^{-7}	8.9×10^{-7}	3.7×10^{-5}	9.6×10^{-4}	1.9×10^{-4}	1.9×10^{-4}	1.7×10^{-4}	7.3×10^{-5}
Mg	1.9×10^{-5}	1.4×10^{-4}	4.7×10^{-2}	9.1×10^{-2}	9.4×10^{-3}	1.5×10^{-3}	5.7×10^{-4}	6.2×10^{-4}
Al	1.4×10^{-5}	2.2×10^{-4}	4.7×10^{-3}	8.0×10^{-3}	1.1×10^{-4}	6.5×10^{-5}	7.6×10^{-5}	7.0×10^{-5}
Si	2.8×10^{-3}	3.9×10^{-1}	1.5×10^{-1}	3.0×10^{-2}	6.3×10^{-3}	1.3×10^{-3}	9.7×10^{-4}	9.2×10^{-4}
S	5.4×10^{-3}	3.8×10^{-1}	3.4×10^{-2}	7.1×10^{-4}	2.4×10^{-4}	3.8×10^{-4}	4.2×10^{-4}	4.2×10^{-4}
Ar	1.7×10^{-3}	5.8×10^{-2}	3.8×10^{-3}	8.2×10^{-5}	7.9×10^{-5}	9.7×10^{-5}	1.1×10^{-4}	1.1×10^{-4}
Ca	3.4×10^{-3}	4.0×10^{-2}	1.0×10^{-3}	3.4×10^{-5}	2.7×10^{-5}	6.1×10^{-5}	7.3×10^{-5}	7.4×10^{-5}
Sc	2.1×10^{-7}	4.9×10^{-7}	4.3×10^{-7}	1.5×10^{-6}	1.3×10^{-6}	3.9×10^{-7}	6.1×10^{-8}	4.5×10^{-8}
Ti	8.1×10^{-4}	5.2×10^{-4}	2.3×10^{-5}	5.6×10^{-6}	5.1×10^{-6}	3.4×10^{-6}	3.4×10^{-6}	3.4×10^{-6}
V	3.1×10^{-5}	1.3×10^{-4}	4.2×10^{-6}	6.0×10^{-7}	7.1×10^{-7}	5.2×10^{-7}	4.5×10^{-7}	4.3×10^{-7}
Cr	2.3×10^{-3}	7.0×10^{-3}	7.6×10^{-5}	1.5×10^{-5}	1.2×10^{-5}	1.9×10^{-5}	2.0×10^{-5}	2.0×10^{-5}
Mn	1.6×10^{-5}	2.0×10^{-4}	1.1×10^{-5}	5.7×10^{-6}	4.2×10^{-6}	1.0×10^{-5}	1.6×10^{-5}	1.5×10^{-5}
Fe	2.7×10^{-3}	4.1×10^{-2}	9.3×10^{-4}	8.7×10^{-4}	8.0×10^{-4}	1.3×10^{-3}	1.4×10^{-3}	1.4×10^{-3}
Co	3.0×10^{-8}	1.8×10^{-8}	1.3×10^{-4}	1.3×10^{-4}	1.8×10^{-4}	6.7×10^{-5}	4.4×10^{-6}	4.0×10^{-6}
Ni	3.1×10^{-2}	2.4×10^{-3}	5.9×10^{-4}	4.5×10^{-4}	4.5×10^{-4}	9.3×10^{-5}	8.2×10^{-5}	8.2×10^{-5}

Table C.3. Same as Table C.1, for the 17 M_{\odot} models.

Element/Zone	Fe/He	Si/S	O/Si/S	O/Ne/Mg	O/C	He/C	He/N	H
$^{56}\text{Ni} + ^{56}\text{Co}$	7.1×10^{-1}	3.1×10^{-2}	2.9×10^{-7}	1.7×10^{-5}	1.8×10^{-5}	2.6×10^{-7}	2.5×10^{-9}	0
$^{57}\text{Ni} + ^{57}\text{Co}$	2.8×10^{-2}	9.2×10^{-4}	1.5×10^{-5}	8.8×10^{-7}	3.0×10^{-8}	6.2×10^{-9}	0	0
^{44}Ti	2.5×10^{-4}	1.3×10^{-5}	5.9×10^{-6}	1.8×10^{-8}	0	0	0	0
H	2.4×10^{-6}	1.2×10^{-7}	6.1×10^{-8}	1.7×10^{-9}	0	0	3.8×10^{-8}	5.4×10^{-1}
He	1.2×10^{-1}	7.7×10^{-6}	3.3×10^{-6}	2.9×10^{-6}	4.5×10^{-2}	9.3×10^{-1}	9.9×10^{-1}	4.4×10^{-1}
C	3.4×10^{-7}	2.0×10^{-5}	6.9×10^{-5}	1.5×10^{-2}	2.4×10^{-1}	4.5×10^{-2}	2.5×10^{-4}	1.2×10^{-4}
N	1.5×10^{-6}	8.0×10^{-7}	1.3×10^{-5}	3.8×10^{-5}	1.1×10^{-5}	1.1×10^{-3}	9.1×10^{-3}	1.0×10^{-2}
O	7.9×10^{-6}	1.6×10^{-2}	2.5×10^{-1}	6.9×10^{-1}	6.8×10^{-1}	1.1×10^{-2}	1.7×10^{-4}	4.0×10^{-3}
Ne	9.0×10^{-6}	2.5×10^{-5}	1.1×10^{-4}	2.1×10^{-1}	2.2×10^{-2}	9.2×10^{-3}	1.1×10^{-3}	1.2×10^{-3}
Na	8.8×10^{-7}	1.1×10^{-6}	1.3×10^{-6}	5.1×10^{-3}	2.0×10^{-4}	1.8×10^{-4}	1.8×10^{-4}	8.9×10^{-5}
Mg	1.8×10^{-5}	1.9×10^{-4}	5.5×10^{-4}	5.8×10^{-2}	6.7×10^{-3}	7.4×10^{-4}	7.0×10^{-4}	7.2×10^{-4}
Al	2.6×10^{-5}	2.8×10^{-4}	2.5×10^{-4}	4.5×10^{-3}	7.4×10^{-5}	7.3×10^{-5}	9.5×10^{-5}	7.1×10^{-5}
Si	1.5×10^{-2}	4.3×10^{-1}	3.5×10^{-1}	1.3×10^{-2}	9.0×10^{-4}	8.3×10^{-4}	8.2×10^{-4}	8.2×10^{-4}
S	2.7×10^{-2}	3.8×10^{-1}	3.1×10^{-1}	2.8×10^{-3}	3.0×10^{-4}	4.1×10^{-4}	4.2×10^{-4}	4.2×10^{-4}
Ar	7.4×10^{-3}	5.3×10^{-2}	5.5×10^{-2}	4.1×10^{-4}	8.6×10^{-5}	1.1×10^{-4}	1.1×10^{-4}	1.1×10^{-4}
Ca	1.0×10^{-2}	3.2×10^{-2}	2.2×10^{-2}	1.5×10^{-4}	4.4×10^{-5}	7.3×10^{-5}	7.4×10^{-5}	7.4×10^{-5}
Sc	3.1×10^{-7}	6.2×10^{-7}	1.3×10^{-6}	1.4×10^{-6}	7.1×10^{-7}	8.8×10^{-8}	4.5×10^{-8}	4.5×10^{-8}
Ti	1.0×10^{-3}	3.2×10^{-4}	1.6×10^{-4}	6.7×10^{-6}	4.9×10^{-6}	3.4×10^{-6}	3.4×10^{-6}	3.4×10^{-6}
V	6.9×10^{-5}	1.2×10^{-4}	1.2×10^{-5}	6.5×10^{-7}	3.2×10^{-7}	4.9×10^{-7}	4.3×10^{-7}	4.3×10^{-7}
Cr	7.2×10^{-3}	4.2×10^{-3}	2.0×10^{-4}	1.4×10^{-5}	1.6×10^{-5}	2.0×10^{-5}	2.0×10^{-5}	2.0×10^{-5}
Mn	1.4×10^{-4}	2.9×10^{-4}	1.6×10^{-5}	5.4×10^{-6}	7.8×10^{-6}	1.6×10^{-5}	1.5×10^{-5}	1.5×10^{-5}
Fe	1.2×10^{-2}	4.8×10^{-2}	1.4×10^{-3}	7.9×10^{-4}	1.0×10^{-3}	1.4×10^{-3}	1.4×10^{-3}	1.4×10^{-3}
Co	3.3×10^{-8}	4.7×10^{-8}	8.8×10^{-7}	1.6×10^{-4}	1.2×10^{-4}	4.8×10^{-6}	4.0×10^{-6}	4.0×10^{-6}
Ni	3.3×10^{-2}	2.3×10^{-3}	8.1×10^{-4}	4.8×10^{-4}	3.1×10^{-4}	8.2×10^{-5}	8.2×10^{-5}	8.2×10^{-5}

- Milisavljevic, D., Fesen, R. A., Gerardy, C. L., Kirshner, R. P., & Challis, P. 2010, *ApJ*, 709, 1343, (M10)
- Nahar, S. N. 1999, *ApJS*, 120, 131
- Nomoto, K., Suzuki, T., Shigeyama, T., et al. 1993, *Nature*, 364, 507
- Nomoto, K. I., Iwamoto, K., & Suzuki, T. 1995, *Phys. Rep.*, 256, 173
- Nussbaumer, H. & Storey, P. J. 1986, *A&AS*, 64, 545
- Panagia, N., Sramek, R. A., & Weiler, K. W. 1986, *ApJ*, 300, L55
- Park, C. 1971, *J. Quant. Spec. Radiat. Transf.*, 11, 7
- Pastorello, A., Kasliwal, M. M., Crockett, R. M., et al. 2008, *MNRAS*, 389, 955
- Pequignot, D. & Aldrovandi, S. M. V. 1986, *A&A*, 161, 169
- Podsiadlowski, P., Joss, P. C., & Hsu, J. J. L. 1992, *ApJ*, 391, 246
- Porter, A. C. & Filippenko, A. V. 1987, *AJ*, 93, 1372
- Ramsbottom, C. A., Hudson, C. E., Norrington, P. H., & Scott, M. P. 2007, *A&A*, 475, 765
- Rutherford, J. A., Mathis, R. F., Turner, B. R., & Vroom, D. A. 1971, *J. Chem. Phys.*, 55, 3785
- Sana, H., de Mink, S. E., de Koter, A., et al. 2012, *Science*, 337, 444
- Schlegel, E. M. & Kirshner, R. P. 1989, *AJ*, 98, 577
- Shigeyama, T., Nomoto, K., Tsujimoto, T., & Hashimoto, M.-A. 1990, *ApJ*, 361, L23
- Shigeyama, T., Suzuki, T., Kumagai, S., et al. 1994, *ApJ*, 420, 341
- Shivvers, I., Mazzali, P., Silverman, J. M., et al. 2013, *MNRAS*, 436, 3614
- Shull, J. M. & van Steenberg, M. 1982, *ApJS*, 48, 95
- Smith, N., Li, W., Filippenko, A. V., & Chornock, R. 2011, *MNRAS*, 412, 1522

- Sollerman, J., Holland, S. T., Challis, P., et al. 2002, A&A, 386, 944
Sollerman, J., Leibundgut, B., & Spyromilio, J. 1998, A&A, 337, 207
Spyromilio, J. 1994, MNRAS, 266, L61
Spyromilio, J. & Pinto, P. A. 1991, in European Southern Observatory Conference and Workshop Proceedings, Vol. 37, European Southern Observatory Conference and Workshop Proceedings, ed. I. J. Danziger & K. Kjaer, 423
Sramek, R. A., Panagia, N., & Weiler, K. W. 1984, ApJ, 285, L59
Sugar, J. & Corliss, C. 1985, Atomic energy levels of the iron-period elements: Potassium through Nickel
Taubenberger, S., Navasardyan, H., Maurer, J. I., et al. 2011, MNRAS, 413, 2140
Taubenberger, S., Valenti, S., Benetti, S., et al. 2009, MNRAS, 397, 677
Timmes, F. X., Woosley, S. E., & Weaver, T. A. 1995, ApJS, 98, 617
Trail, W. K., Morrison, M. A., Zhou, H.-L., et al. 1994, Phys. Rev. A, 49, 3620
Uomoto, A. & Kirshner, R. P. 1985, A&A, 149, L7
Van Dyk, S. D., Zheng, W., Clubb, K. I., et al. 2013, ApJ, 772, L32
Verner, D. A. & Ferland, G. J. 1996, ApJS, 103, 467
Wheeler, J. C. & Levreault, R. 1985, ApJ, 294, L17
Woosley, S. E., Eastman, R. G., Weaver, T. A., & Pinto, P. A. 1994, ApJ, 429, 300
Woosley, S. E. & Heger, A. 2007, Phys. Rep., 442, 269
Woosley, S. E., Pinto, P. A., & Ensmann, L. 1988, ApJ, 324, 466
Yoon, S.-C., Woosley, S. E., & Langer, N. 2010, ApJ, 725, 940
Zhang, H. L. & Pradhan, A. K. 1995a, A&A, 293, 953
Zhang, H. L. & Pradhan, A. K. 1995b, Journal of Physics B Atomic Molecular Physics, 28, 3403
Zhang, T., Wang, X., Zhou, X., et al. 2004, AJ, 128, 1857

Acknowledgments

We thank Dan Milisavljevic and Peter Meikle for providing observational data on SN 2008ax and SN 1993J, respectively. **ST acknowledges support by TRR 33 “The Dark Universe” of the German Research Foundation.**